CONTRACTOR REPORT

WIPP Library

ENTERED

SAND92—7306
Unlimited Release
UC—721

A Modeling Approach To Address Spatial Variability within the Culebra Dolomite Transmissivity Field

A. Marsh LaVenue
INTERA, Inc.
1650 University Blvd. NE, Suite 300
Albuquerque, NM 87102

B. S. RamaRao
INTERA Inc.
6850 Austin Center Blvd., Suite 300
Austin, TX 78731

Prepared by Sandia National Laboratories Albuquerque, New Mexico 87185 and Livermore, California 94550 for the United States Department of Energy under Contract DE-AC04-76DP00789

Printed December 1992

SCANNED

921201.6

Issued by Sandia National Laboratories, operated for the United States Department of Energy by Sandia Corporation.

NOTICE: This report was prepared as an account of work sponsored by an agency of the United States Government. Neither the United States Government nor any agency thereof, nor any of their employees, nor any of their contractors, subcontractors, or their employees, makes any warranty, express or implied, or assumes any legal liability or responsibility for the accuracy, completeness, or usefulness of any information, apparatus, product, or process disclosed, or represents that its use would not infringe privately owned rights. Reference herein to any specific commercial product, process, or service by trade name, trademark, manufacturer, or otherwise, does not necessarily constitute or imply its endorsement, recommendation, or favoring by the United States Government, any agency thereof or any of their contractors or subcontractors. The views and opinions expressed herein do not necessarily state or reflect those of the United States Government, any agency thereof or any of their contractors.

Printed in the United States of America. This report has been reproduced directly from the best available copy.

Available to DOE and DOE contractors from
Office of Scientific and Technical Information
PO Box 62
Oak Ridge, TN 37831

Prices available from (615) 576-8401, FTS 626-8401

Available to the public from
National Technical Information Service
US Department of Commerce
5285 Port Royal Rd
Springfield, VA 22161

NTIS price codes
Printed copy: A06
Microfiche copy: A01

SAND92-7306
Unlimited Release
Printed December 1992

Distribution
Category UC-721

A Modeling Approach To Address Spatial Variability within the Culebra Dolomite Transmissivity Field

A. Marsh LaVenue
INTERA Inc.
1650 University Blvd. NE, Suite 300
Albuquerque, NM 87102

B.S. RamaRao
INTERA Inc.
6850 Austin Center Blvd., Suite 300
Austin, TX 78731

ABSTRACT

Spatial estimates of transmissivity, which are essential input to a groundwater flow model, are usually developed from a limited number of transmissivity measurements and therefore associated with an uncertainty. In an attempt to assess the spatial variability of the unmeasured transmissivities within the Culebra Dolomite near the Waste Isolation Pilot Plant (WIPP), a multiple realization approach is employed. An innovative aspect of the methodology is the generation of an ensemble of conditional simulations of the transmissivity field, which preserves the statistical moments and spatial correlation structure of the measured transmissivity field and honors the measured values at their locations. Each simulation is then calibrated, using an iterative procedure, to match an exhaustive set of steady-state and transient pressure data. A completely automated inverse algorithm using pilot points as parameters of calibration was employed. The methodology was applied to the transmissivity fields for the Culebra Dolomite aquifer, and 70 conditional simulations were produced and calibrated. Based on an analysis of the calibrated transmissivity fields, additional data in a region east and north of the H-3 borehole would help to more accurately characterize the transmissivity of the region and reduce the uncertainty in calculating groundwater travel times. Progress in these areas would, in, turn, reduce the uncertainty in the prediction of concentrations at the accessible environment boundary.

---

*The work described in this report was performed for Sandia National Laboratories under Contract No. 67-0412.

ACKNOWLEDGMENT

The authors wish to acknowledge the contributions to this work made by Ghislain de Marsily of University of Paris VI, Shin Yang of INTERA Inc., Walt Beyeler of Science Applications International Corporation, Tony Zimmerman of GRAM Inc., and Bruce Baker of Technadyne. In addition, the authors wish to recognize the technical reviews of this report by Mel Marietta (6342) and Richard Beauheim (6119) of Sandia National Laboratories. We also acknowledge the efforts of Janet Chapman, Tech Reps, Inc., during the editing and production of this report.

CONTENTS

1. INTRODUCTION 1

2. SITE DESCRIPTION AND REVIEW OF PAST MODELING STUDIES 3

2.1 WIPP Site Description 3
2.2 Previous Modeling Studies 11
2.3 Incorporating Uncertainty in the Culebra Transmissivity Field to Performance Assessment Calculations 13

3. METHODOLOGY 21

3.1 Uncertainty Analysis: Need and a Strategy 21
3.2 Analysis Methodology: An Overview 21
3.3 Simulated Transmissivities 23

3.3.1 Unconditional Simulations 24
3.3.2 Conditional Simulations 27
3.3.3 Simulated Fields: Computational Options 30
3.3.4 Validation of Simulations 31

3.4 Automated Calibration 31

3.4.1 Objective Function 31
3.4.2 Parameters of Calibration 33
3.4.3 Pilot-Point Location 33
3.4.4 Pilot-Point Transmissivities: Optimization 37
3.4.5 Pilot-Point Transmissivities: Constraints 44
3.4.6 Convergence Criteria 45
3.4.7 Computational Experience 47
3.4.8 Earlier Inverse Algorithms: Similarities and Differences 47

3.5 Code Development and Organization 48

4. APPLICATION 53

4.1 Application to 1990 Model Grid 53
4.2 Description of the 1992 Culebra Model 61

4.2.1 Model Grid and Boundary Conditions 61
4.2.2 Model Initial Kriged-Transmissivity Field and Its Uncertainty 68
4.2.3 Model Transient Time Steps 71

4.3 Discussion of the Calibration of a Single Realization 71
4.4 Discussion of the Ensemble of Calibrated Conditionally Simulated Transmissivity Fields 86

4.4.1 Ensemble Mean Transmissivities 86
4.4.2 Ensemble Steady-State Head Differences 86
4.4.3 Ensemble Groundwater Travel Times 94

5. DISCUSSION 103

6. CONCLUSIONS 109

REFERENCES 111

NOMENCLATURE 115

FIGURES

2-1 Geologic column representative of WIPP area 4
2-2 Map of WIPP site and surrounding area. 5
2-3 Center-of-Culebra elevations in the model area 6
2-4 Culebra $\log_{10}$ transmissivities at the WIPP-area boreholes 7
2-5 Formation fluid density values of the Culebra Dolomite 8
2-6 Mean $\log_{10}$ storativity values of the Culebra Dolomite 9
2-7 Freshwater heads in Culebra Dolomite. 10
2-8 Approximate boundaries of groundwater flow models in the WIPP region 12
2-9 Initial kriged $\log_{10}$ transmissivities 14
2-10 Transient calibrated $\log_{10}$ transmissivities 15
2-11 Difference between initial transmissivity field (Figure 2-9) and calibrated transmissivity field (Figure 2-10) determined in LaVenue et al. (1990). 16
2-12 Calculated and observed transient freshwater heads at H-11, H-15, and DOE-1 using transient calibrated transmissivity field 17
2-13 Particle travel path through the transient calibrated transmissivity field 18
2-14 Cumulative distribution of travel times of the 60 flow fields used in 1991 Performance Assessment calculations 20
3-1 Flowchart illustrating calibration of conditionally simulated transmissivity fields 22
3-2 Schematic of real, simulated, and kriged fields. 25
3-3 Schematic representation of the field and turning bands lines 26
3-4 Relationships between conditional and unconditional simulation. 29
3-5 Pilot-point schematic 34
3-6 Inner and outer iterations of calibration 46
3-7 GRASP-INV code organization 50
4-1 Transient calibrated kriged transmissivity field determined using GRASP-INV and the 1990 model grid 55
4-2 Transient heads calculated using the GRASP-INV transient calibrated model: Well H-1, Hydropad H-6, and Well DOE-2 57
4-3 Transient heads calculated using the GRASP-INV transient calibrated model: Hydropad H-011, Well DOE-1, and Hydropad H-15 58
4-4 Enlargement of transmissivity field in the vicinity of the southern WIPP-site boundary 59
4-5 Differences between the GRASP-INV calibrated transmissivity field and the manually calibrated field of LaVenue et al., 1990. 60
4-6 Particle travel paths from the 1990 and 1992 kriged transmissivity fields 62
4-7 Finite-difference regional grid used in 1992 modeling study 63
4-8 Comparison of 1990 and 1992 model areas. 64
4-9 Initial kriged grid-block $\log_{10}$-transmissivity estimates (i.e., the average over the specific area of each block as determined using a 2 x 2 Gauss-point grid within each grid block) 69
4-10 Estimation errors of the initial kriged field 70
4-11 Unconditional simulation of a $\log_{10}$ transmissivity field on the Gauss grid. 73
4-12 Kriged field using the unconditional sampled data as input. 74
4-13 Differences between the unconditional simulation (UCS) field (Figure 4-11) and the simulated kriged (SK) field (Figure 4-12) 75
4-14 Initial conditionally simulated (CS) field of the example realization on the Gauss grid 76
4-15 Initial conditionally simulated (CS) field of the example realization on the finite-difference grid. 77
4-16 Contour map of the differences between the calculated and observed freshwater heads 78
4-17 Sensitivities of the initial steady-state performance measure to an increase in model transmissivities. 80
4-18 The conditionally simulated (CS) field during the second step of the steady-state calibration. 81
4-19 Increase in transmissivities after a pilot point was added during steady-state calibration 82
4-20 DOE-1 and H-15 transient hydrographs and their response to pumping at the H-11 borehole 83
4-21 Calibrated conditionally simulated (CS) transmissivity field 84
4-22 Differences between initial and calibrated conditionally simulated (CS) transmissivity fields 85
4-23 Groundwater travel path through calibrated conditionally simulated (CS) field 87

FIGURES (continued)

4-24 Ensemble transmissivity field resulting from a mean calculation performed across the realizations. 88
4-25 Ensemble transmissivity field in the vicinity of the southern WIPP-site boundary..... 89
4-26 Calibrated transmissivities of the 1990 model in the vicinity of the southern WIPP-site boundary..... 90
4-27 Histogram of the average root-mean squared error (RMSE) value for each of the 70 simulations..... 91
4-28 Contour surface of the root-mean squared error (RMSE) values over the model domain..... 93
4-29 Travel time cumulative distribution function (cdf) determined from the 70 calibrated fields..... 95
4-30 Histogram of travel times from ensemble of transient calibrated fields..... 96
4-31 Travel paths corresponding to the travel times contained in the cumulative distribution function (cdf)..... 97
4-32 Cumulative distribution function (cdf) of travel times determined from the transient-calibrated fields (TCDF) and the cdf determined from the steady-state calibrated fields (SCDF)..... 98
4-33 Histogram of travel times from ensemble of fields calibrated only to steady-state head data..... 100
4-34 Travel paths associated with ensemble of transmissivity fields calibrated only to steady-state head data..... 101
5-1 Scatterplot of goodness-of-fit of H-15 drawdown to travel times..... 104
5-2 A transmissivity field that has an excellent fit to the steady-state and transient pressures and an associated groundwater travel time of 15,700 yr..... 105
5-3 A transmissivity field that has a fair fit to the transient pressures and an associated groundwater travel time of 9900 yr. 106
5-4 Histogram of groundwater particle distance traveled to southern WIPP-site boundary for the ensemble of calibrated fields..... 108
5-5 Scatterplot of harmonic-mean transmissivity over first 2000 m of flow path for ensemble of fields vs. associated groundwater travel time..... 108

TABLES

2-1 Summary of Modeling Investigations of the Rustler Formation or Culebra Dolomite Member in the WIPP-Site Region 11
3-1 Subroutines and Their Functions 51
4-1 Events Used during Transient Calibration 54
4-2 Difference Between Calculated and Observed Freshwater Heads for GRASP-INV Calibrated Field using the 1990 Model Grid 56
4-3 Prescribed Pressure Boundaries 65
4-4 Average Root-Mean Squared Error (RMSE) Values for the Ensemble Differences between Calculated and Observed Heads 92

1. INTRODUCTION

The Waste Isolation Pilot Plant (WIPP) near Carlsbad, New Mexico, is a research and development project of the United States Department of Energy (DOE). The WIPP is designed to be the first mined geologic repository to demonstrate the safe disposal of transuranic (TRU) radioactive wastes generated by DOE defense programs since 1970. Before disposing of radioactive waste at the WIPP, the DOE must have a reasonable expectation that the WIPP will comply with the quantitative requirements of Subpart B of the United States Environmental Protection Agency's (EPA) *Environmental Standards for the Management and Disposal of Spent Nuclear Fuel, High-Level and Transuranic Radioactive Wastes* (40 CFR Part 191, EPA, 1985). Comparing the long-term performance of the WIPP disposal system with the quantitative requirements of 40 CFR Part 191 will help determine whether the disposal system will provide safe disposal of radionuclides.

Performance assessment as defined in the Containment Requirements of Subpart B of 40 CFR Part 191 is an analysis that identifies the processes and events that might affect the disposal system, examines the effects of these processes and events on the performance of the disposal system, and estimates the cumulative releases of radionuclides, considering the associated uncertainties, caused by all significant processes and events (191.12(q)).

Major sources of data for WIPP performance assessment calculations result from site-characterization activities, which began at the WIPP site in 1976. Since 1983, when full construction of the facility was started, site-characterization activities have had the objectives of updating or refining the overall conceptual models of the geologic, hydrologic, and structural behavior of the WIPP site and providing data adequate for use in the WIPP performance assessment (Lappin, 1988). As the WIPP Project moves toward a compliance determination, the present objective of site-characterization efforts, as described in this report, is to reduce uncertainty in the conceptual models.

Uncertainty and sensitivity analysis for the total disposal system is the task of the WIPP Performance Assessment (PA) Department at Sandia National Laboratories. Because some uncertainty about the parameters controlling groundwater flow and transport will always remain, the WIPP PA calculations employ Monte Carlo techniques to provide estimates of radionuclide concentrations at the accessible environment boundary (WIPP PA Department, 1992, Vol. 2). This approach requires that cumulative distribution functions be selected for numerous imprecisely known input parameters. For example, local-scale multiphase codes that simulate the interaction of waste-generated gas and brine within the repository and the Salado Formation require input parameters such as residual saturation, threshold pressure, undisturbed pore pressure, and porosity. Examples of input parameters needed to simulate far-field flow and transport through the Culebra Dolomite, which is considered to be the principal pathway for offsite transport, include transmissivity, dispersivity, and porosity. The reports by the WIPP PA Department (1992) and the Sandia WIPP Project (1992) describe the input parameters used in the PA calculations, the codes used during the calculations, and the relationships between the parameters and codes.

Numerous modeling studies over the last 10 years have focused on characterizing the hydrogeology of the Culebra Dolomite. In general, these studies have attempted to characterize the Culebra transmissivity field by iteratively reducing the differences between the calculated and observed heads within a single groundwater numerical model. The head differences have been reduced by modifying the transmissivity field either by intuition or through

the use of numerical algorithms such as kriging. While these studies have improved our understanding of the relationship between the transmissivity and the flow fields within the Culebra, they have not provided a metric for quantifying the uncertainty within the transmissivity field. This report presents an attempt to quantify this uncertainty and assess the spatial variability within the field.

The theory and subsequent application of a new numerical model, GRASP-INV, which solves the groundwater inverse problem, is also presented in this report. The GRASP-INV code has the capability of generating and subsequently calibrating conditionally simulated (CS) transmissivity fields. Because each CS field has similar broad features but distinctly different small-scale variations, the GRASP-INV code is able to produce numerous, equally probable, transmissivity fields calibrated to the observed head data. The unique features present within each calibrated field are related to the uncertainty of the transmissivity field. The WIPP PA Department has incorporated this uncertainty into the Monte Carlo analysis by partially ordering a set of equally probable transmissivity fields by travel time to the accessible environment, and then drawing one field for each system calculation by sampling a uniformly distributed index variable. Because a Latin Hypercube Sampling technique is used and the number of fields in the set is equal to the number of imprecisely known parameters, each field is drawn once in the PA calculations. Although not required for a compliance assessment with *40 CFR 191, Subpart B*, travel time is a good intermediate performance measure and provides some physical interpretation of the index variable for sensitivity and uncertainty analysis.

The objective of this report is to address the following questions:

1. What impact did the subjective assignment of pilot-point transmissivities and regionalized approach to calibration have upon the results determined in an earlier study (LaVenue et al., 1990)?

2. How can information concerning the spatial variability of the Culebra transmissivity field be gained from the information concerning the uncertainty of the Culebra transmissivities?

3. What is the uncertainty in the groundwater travel time given the uncertainty in the transmissivity field?

4. What features of the variability within the transmissivity field have the most significant impact upon the groundwater travel time?

2. SITE DESCRIPTION AND REVIEW OF PAST MODELING STUDIES

2.1 WIPP Site Description

The Waste Isolation Pilot Plant (WIPP) is a US Department of Energy facility currently being evaluated to assess its suitability for the isolation of defense transuranic wastes. The WIPP site lies within the geologic region known as the Delaware Basin. The upper seven formations present at or in the vicinity of the WIPP site are, in descending order, the Gatuña Formation, the Dockum Group, the Dewey Lake Red Beds, the Rustler Formation, the Salado Formation, the Castile Formation, and the Bell Canyon Formation (Figure 2-1). The proposed repository horizon lies within the bedded salt of the Salado Formation.

The Rustler Formation consists of beds of halite, siltstone, anhydrite, and dolomite. It is divided into five separate members based on lithology. The Culebra Dolomite, one of these five members, has been identified through extensive field site-characterization efforts as the most transmissive, laterally continuous hydrogeologic unit above the Salado Formation and is considered to be the principal pathway for offsite radionuclide transport in the subsurface, should an accidental breach of the repository occur. Based upon observations of outcrops, core, and detailed shaft mapping, the Culebra can be characterized, at least locally, as a fractured medium at the WIPP site. As the amount of fracturing and development of secondary porosity increases, the Culebra transmissivity generally increases.

Over the past 12 years, a significant effort has been directed toward field investigations at the WIPP site. These investigations have been instrumental in providing estimates of the variability of the hydrogeologic properties within the Culebra Dolomite such as transmissivity and storativity. Numerous boreholes in and immediately surrounding the WIPP-site area have been drilled and tested within the Culebra in support of these investigations (Figure 2-2). The Culebra aquifer, which dips toward the southeast (Figure 2-3), has spatially varying characteristics across the WIPP-site area. For instance, an increase in transmissivity and a decrease in formation-fluid density exists from east to west (Figures 2-4 and 2-5). There is no apparent trend to the storativity data obtained from the tests within the Culebra (Figure 2-6).

The transmissivity data base for the Culebra Dolomite is derived from numerous hydraulic tests performed at the WIPP site. Values have been obtained from drill-stem tests (DSTs), slug tests, and local- and regional-scale pumping or interference tests (Beauheim, 1986, 1987a, 1987b, 1987c, 1988, 1989; Mercer, 1983; Saulnier, 1987). Transmissivity values interpreted from these tests extend over a range of seven orders of magnitude. The large range in the transmissivities results from the variation in the fractured nature of the Culebra and from the removal of halite across parts of the site area.

A contour map of the undisturbed freshwater heads within the Culebra is illustrated in Figure 2-7. The contours in the northeastern portion of the model area do not represent accurate heads due to the lack of data in this area to guide the contouring algorithm. Generally, though, the freshwater heads reveal a predominantly southerly flow direction across the WIPP site. The heads southeast of the WIPP-site area reflect an approximate westerly flow

System	Series	Group	Formation	Member
Recent	Recent		Surficial Deposits	
Quaternary	Pleistocene		Mescalero Caliche	
			Gatuña	
Triassic		Dockum	Undivided	
Permian	Ochoan		Dewey Lake Red Beds	
			Rustler	Forty-niner
				Magenta Dolomite
				Tamarisk
				Culebra Dolomite
				unnamed
			Salado	
			Castile	
	Guadalupian	Delaware Mountain	Bell Canyon	
			Cherry Canyon	
			Brushy Canyon	

TRI-6330-89-1

Figure 2-1. Geologic column representative of WIPP area (after Powers et al., 1978).

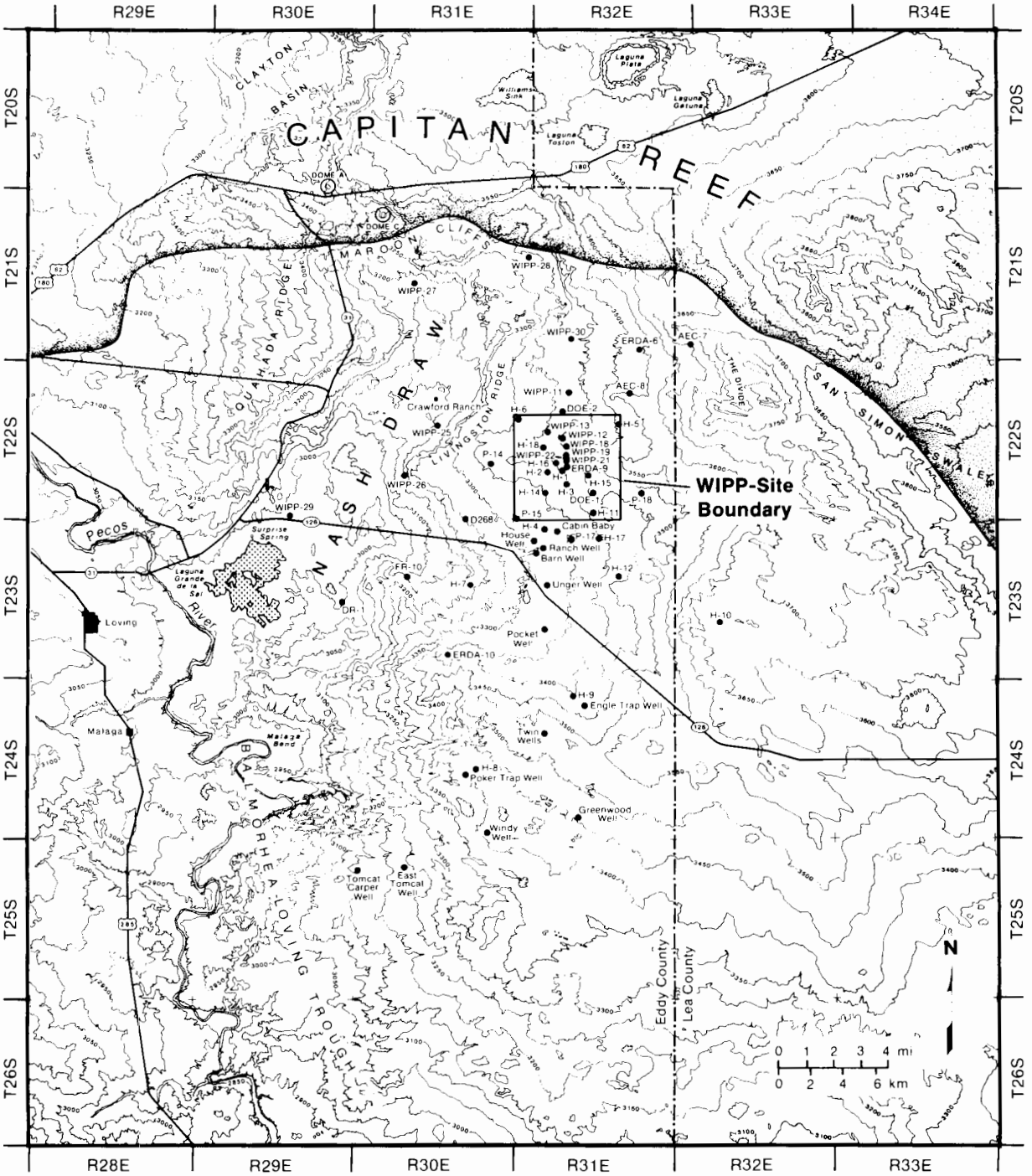

Figure 2-2. Map of WIPP site and surrounding area.

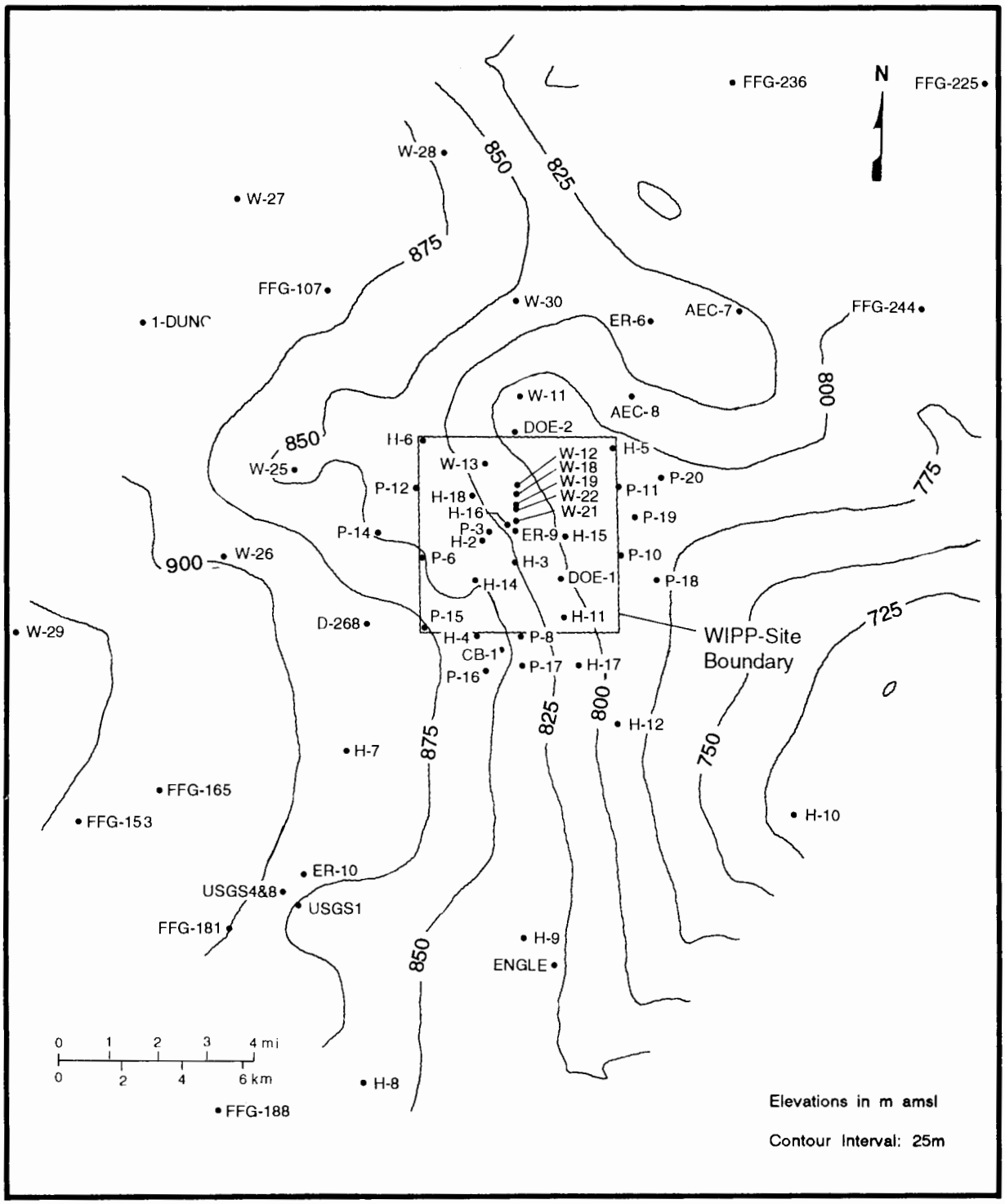

TRI-6342-3308-0

Figure 2-3. Center-of-Culebra elevations in the model area.

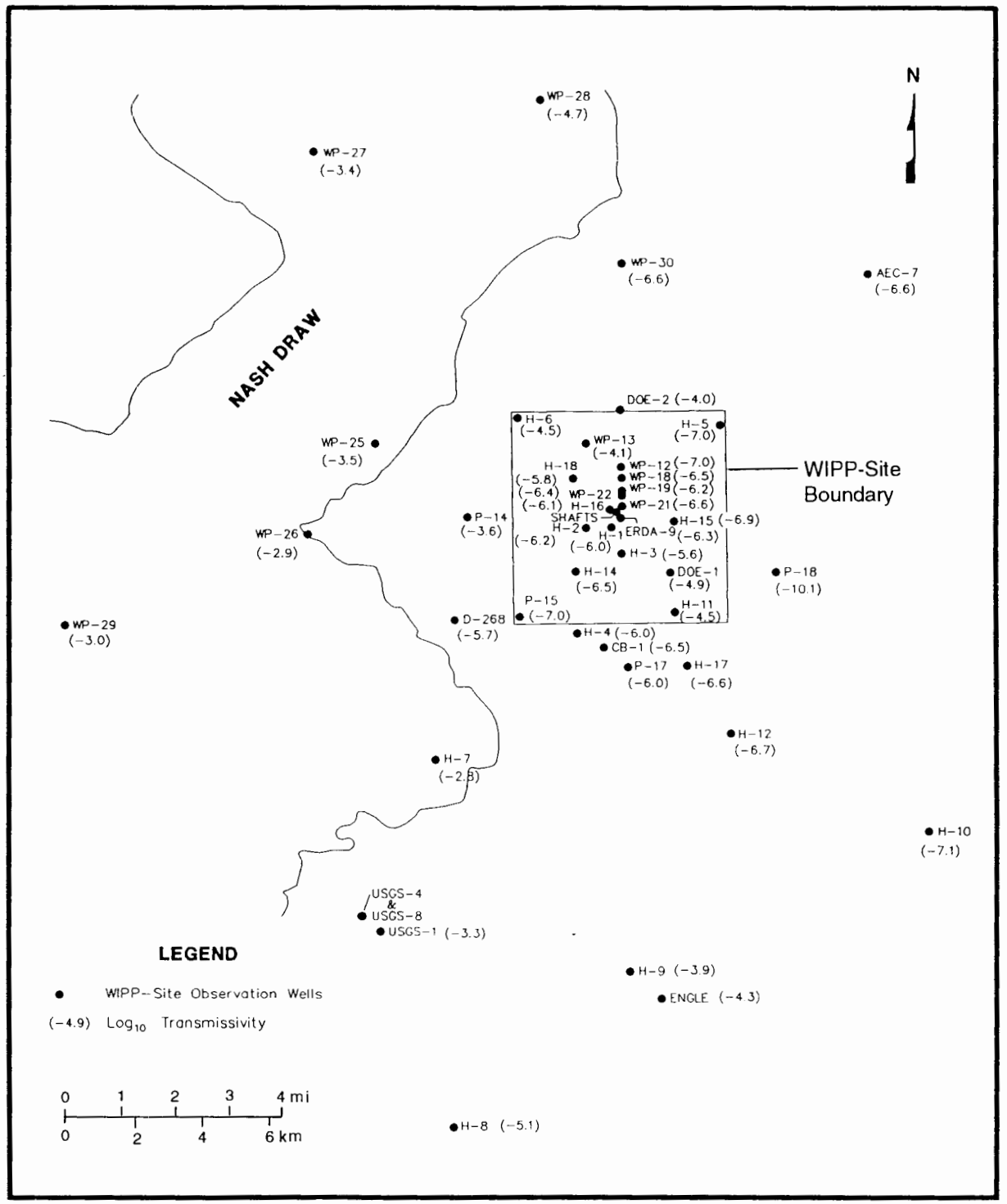

TRI-6342-3309-0

Figure 2-4. Culebra $\log_{10}$ transmissivities at the WIPP-area boreholes (after Cauffman et al., 1990).

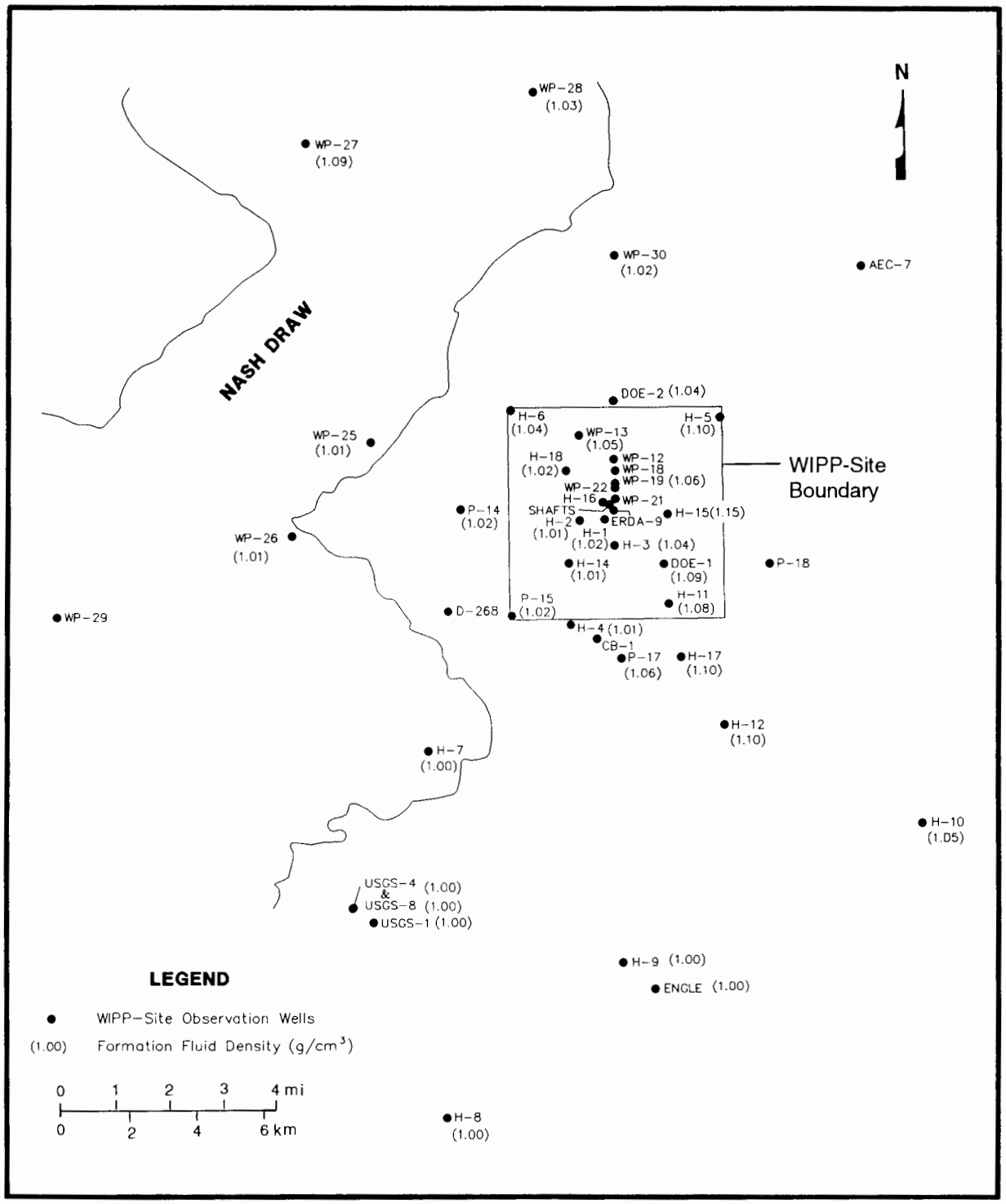

TRI-6342-3310-0

Figure 2-5. Formation-fluid density values of the Culebra Dolomite (after Cauffman et al., 1990).

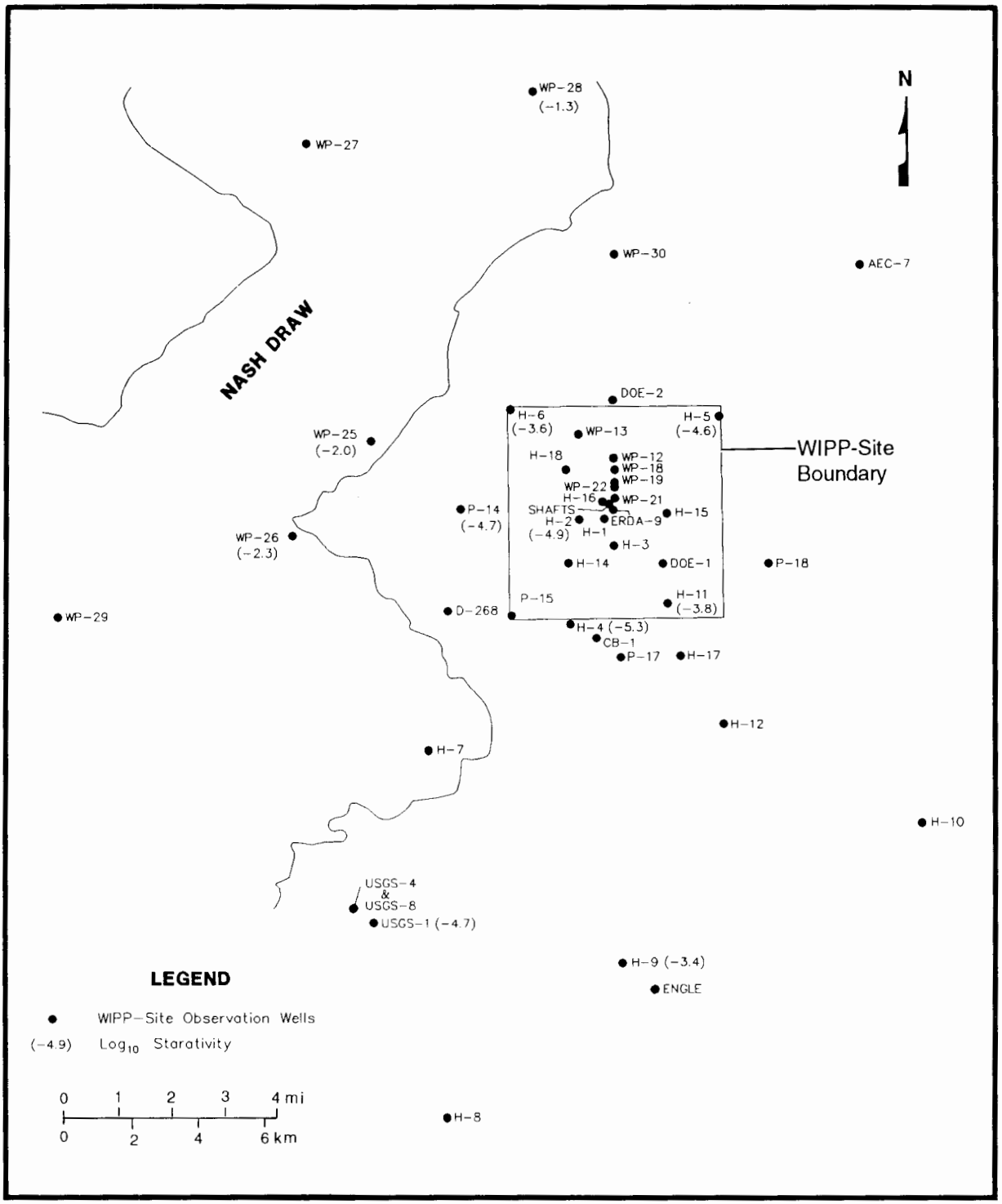

TRI-6342-3311-0

Figure 2-6. Mean $\log_{10}$ storativity values of the Culebra Dolomite (after Cauffman et al., 1990).

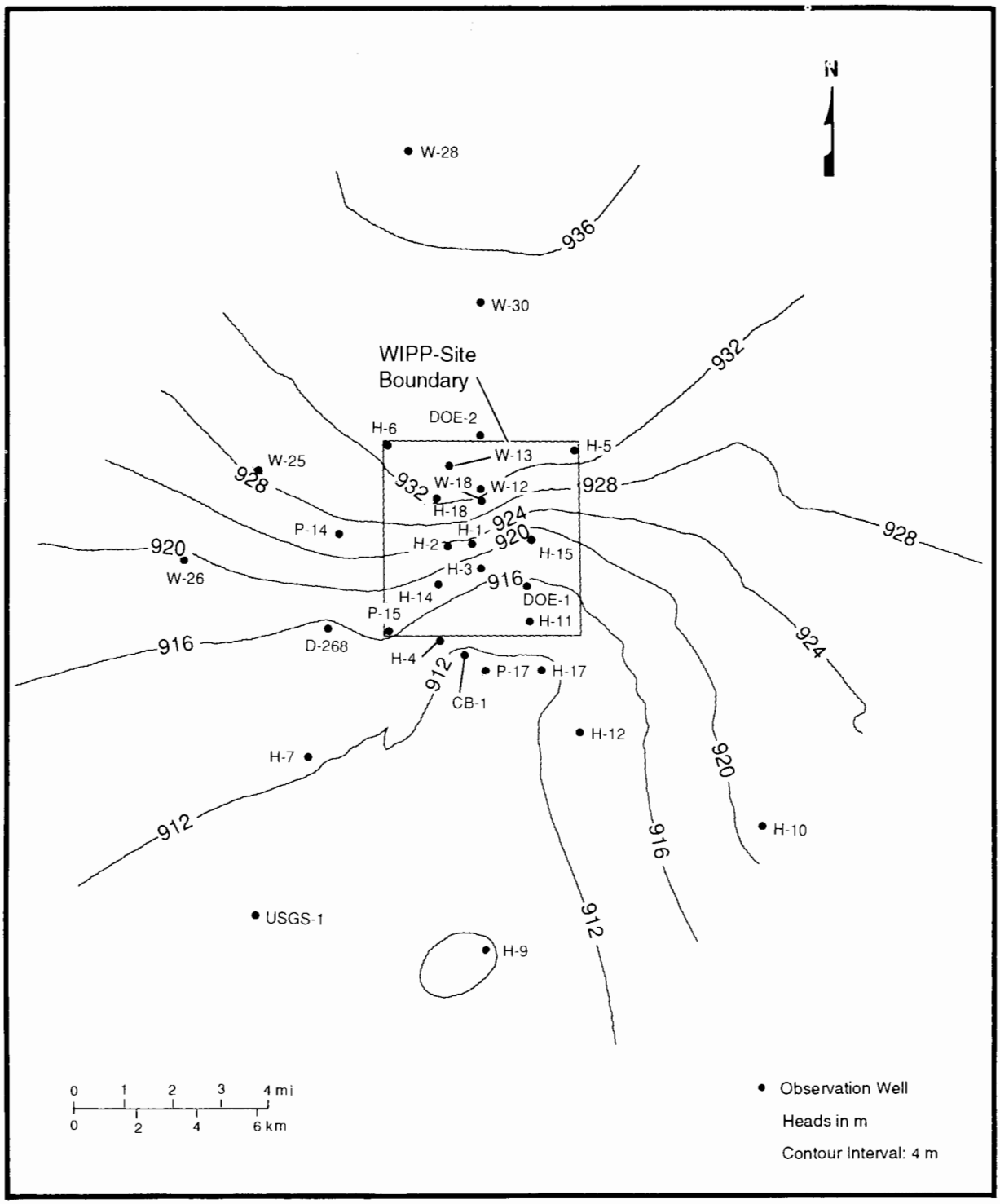

TRI-6342-3322-0

Figure 2-7. Freshwater heads in Culebra Dolomite.

direction. The freshwater heads used in this study were taken from Table 5.5 of LaVenue et al. (1990). The head estimates at several boreholes (e.g., H-14 and H-18) were increased to account for the residual drawdown still affecting the hydrographs as a result of the construction of the shafts. A complete discussion of the increase in the initial head estimates may be found in Table 5.4 of LaVenue et al. (1990).

2.2 Previous Modeling Studies

Since the early 1980s, the Culebra has been a focus of numerical modeling activities. Both regional and local-scale models have been constructed over the years due to changes in the conceptual model and in the definitions of the parameter-value distributions. These changes have occurred as a result of the continuing field investigations and the subsequent expansion of the hydrogeologic data base. Table 2-1 lists the modeling studies that have been conducted to date. Figure 2-8 illustrates the model boundaries associated with each of these models. A detailed review of the modeling efforts prior to 1988 may be found in LaVenue et al. (1988).

In 1990, LaVenue et al. calibrated a two-dimensional model to the extensive data set of observed steady-state and transient heads within the Culebra. The data base used in this study originated from approximately 10 years of regional hydrogeologic site-characterization efforts conducted in the Culebra Dolomite. A summary and evaluation of the data base used for this modeling study and complete listing of data sources are presented in Cauffman et al. (1990). The data base includes borehole locations, ground-surface and Culebra elevations, Culebra thickness, transmissivity, storativity, formation-fluid density, and freshwater heads calculated from depth-to-water and downhole-transducer-pressure measurements from the observation-well network. The data base was used in conjunction with kriging to assign the initial estimates of Culebra transmissivity, elevation, and fluid density to each grid block in the model.

Table 2-1. Summary of Modeling Investigations of the Rustler Formation or Culebra Dolomite Member in the WIPP-Site Region

Reference	Hydrogeologic Unit Modeled	Head Calibration
U.S. DOE (1980a,b)	Rustler	Steady State
D'Appolonia (1981)	Rustler	Steady State
Cole and Bond (1980)	Rustler	Steady State
Barr et al. (1983)	Culebra	Steady State
Davies (1989)	Culebra	Steady State
Niou and Pietz (1987)	Culebra	Transient
Haug et al. (1987)	Culebra	Steady State
LaVenue et al. (1988)	Culebra	Steady State
Bertram-Howery et al. (1990)	Culebra	Steady State
LaVenue et al. (1990)	Culebra	Steady State/Transient
WIPP PA Division (1991)	Culebra	Steady State

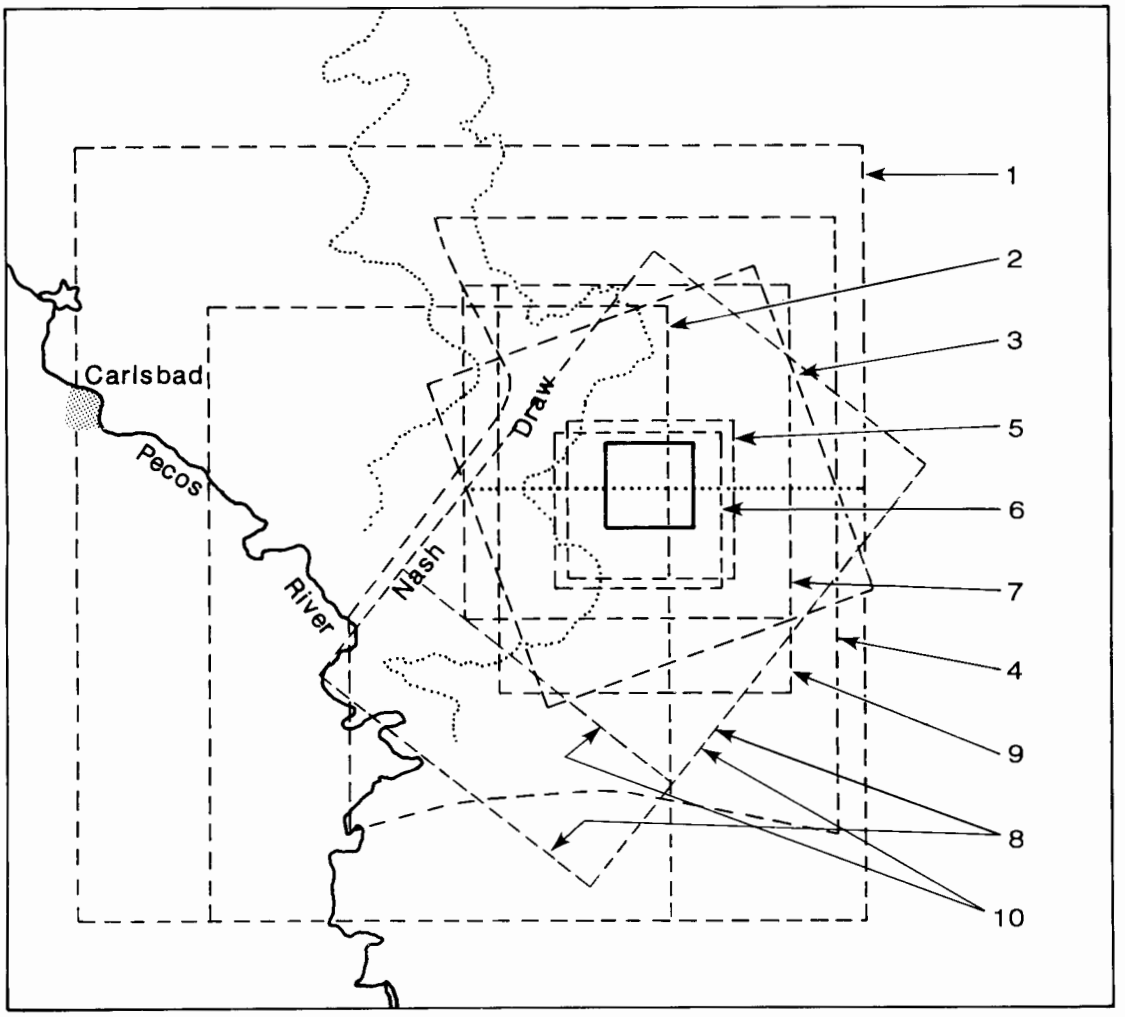

1 U.S. Department of Energy (1980a, 1980b); Cole and Bond (1980)
2 D'Appolonia Consulting Engineers (1981)
3 Barr et al. (1983)
4 Davies (1989)
5 Niou and Pietz (1987)
6 Haug et al. (1987)
7 La Venue et al. (1988)
8 Bertram - Howery et al. (1990)
9 La Venue et al. (1990)
10 WIPP PA Division (1991)

1 5 10 mi
0 5 10 15 km

TRI-6342-3312-0

Figure 2-8. Approximate boundaries of groundwater flow models in the WIPP region (after Lappin et al., 1989).

The calibration approach used by LaVenue et al. employed an adjoint-sensitivity technique to determine flow-field sensitivity coefficients. The adjoint algorithm was coupled with a kriging algorithm that provided estimates of grid-block transmissivity values. This approach, developed by RamaRao and Reeves (1990), is similar in concept to one proposed in Marsily, de, et al. (1984). The notable exception in the RamaRao and Reeves approach, relative to de Marsily's inverse formulation, stems from the optimal identification of locations where modification of the model's kriged transmissivity or boundary-pressure values will directly improve the overall fit between measured and model-calculated heads at selected wells. At the locations identified as most sensitive to transmissivity changes, synthetic transmissivity values, referred to as pilot points, were added to the transmissivity data base and used as input for kriging the transmissivity field. The values of the pilot points were assigned by the modeler based upon constraints determined by the surrounding transmissivity values and any interference test values in the vicinity. More details concerning the approach may be found in RamaRao and Reeves (1990).

The LaVenue et al. (1990) modeling study produced the first transmissivity field calibrated to both steady-state and transient heads. Figures 2-9 and 2-10 illustrate the initial and calibrated transmissivity fields determined in LaVenue et al. (1990). The differences between these two fields are illustrated in Figure 2-11. The major difference is the introduction of a high-transmissivity region south of the P-17 borehole, which extends northward passing just east of the H-11 and DOE-1 boreholes and terminating near the H-15 borehole. This feature was introduced into the transmissivity field in order to match the drawdown that occurred in the DOE-1 and H-15 boreholes during the H-11 pumping test (Figure 2-12). One other difference between the initial and calibrated kriged transmissivity fields occurs in the region between the H-3 and CB-1 boreholes where the initial transmissivities are higher than the calibrated transmissivities.

The high-transmissivity feature south of H-15 and the lower transmissivity region south of H-3 significantly affect the velocity field within the Culebra. Figure 2-13 shows the travel path of a non-reactive particle advecting through the calibrated model velocity field. The starting point is located within the Culebra at a position analogous to the centroid of the repository. The travel path has a distinct easterly direction that is a result of the northern extension of the high-transmissivity zone. The calculated travel time from the starting point to the southern WIPP-site boundary was 14,000 yr assuming a single porosity value of 16%. Processes of dispersion, transport in fractures, matrix diffusion, and sorption were not considered in this calculation. The travel time that would be determined by including these processes could be very different from the value presented above.

2.3 Incorporating Uncertainty in the Culebra Transmissivity Field to Performance Assessment Calculations

Efforts to incorporate uncertainty in the Culebra transmissivity field into performance assessment (PA) calculations have been somewhat evolutionary. In the 1990 PA calculations, the Culebra was divided into seven zones or regions. A mean transmissivity value and an associated standard deviation was assigned to each zone. By sampling from the distributions associated with each zone, multiple realizations of zonal transmissivity values were subsequently used as input to the flow and transport calculations. Although computationally simple, the specification of large zones significantly reduces the spatial variability within a given realization because each zone is assigned a constant value during each realization.

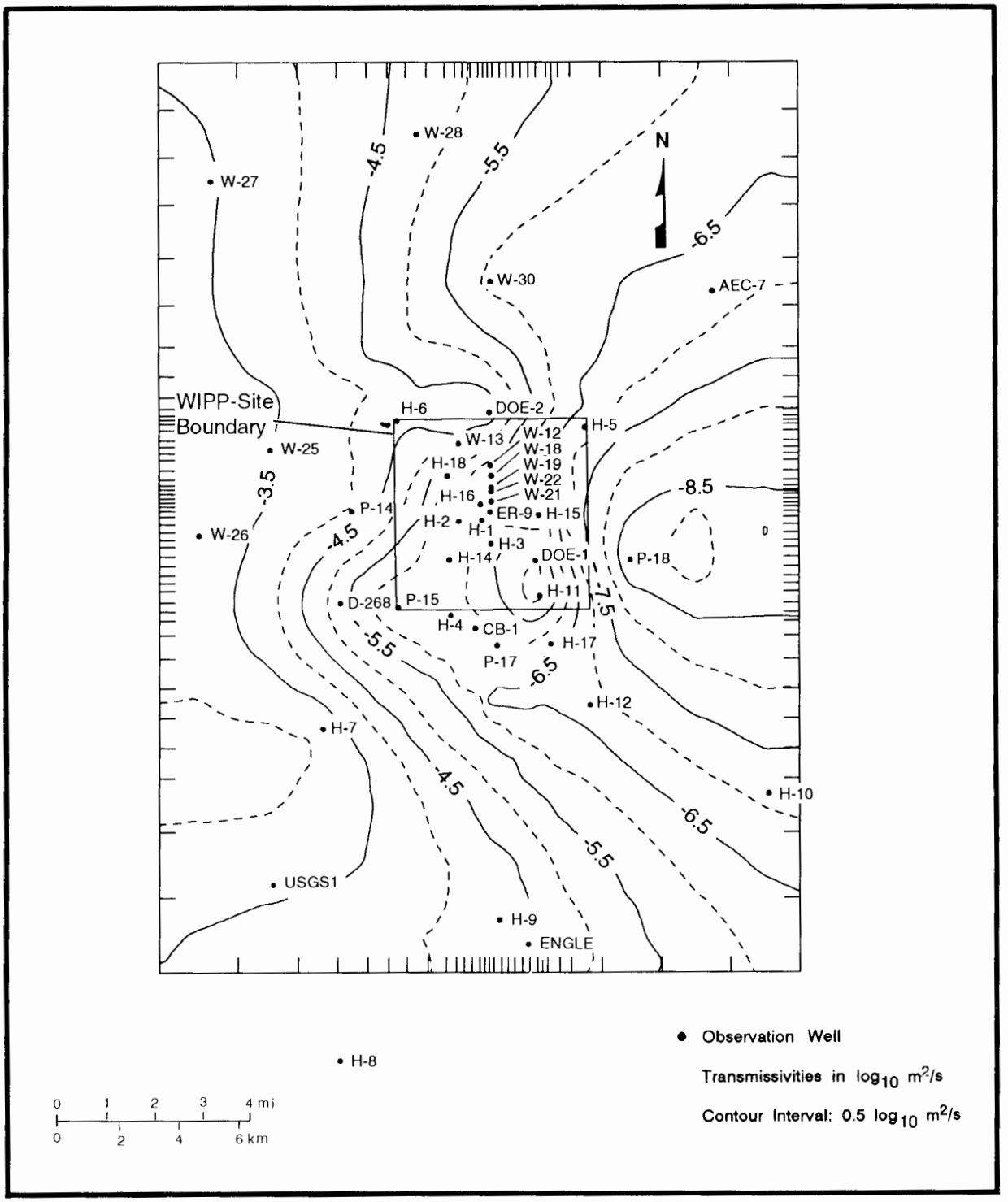

TRI-6342-3313-0

Figure 2-9. Initial kriged $\log_{10}$ transmissivities (after LaVenue et al., 1990).

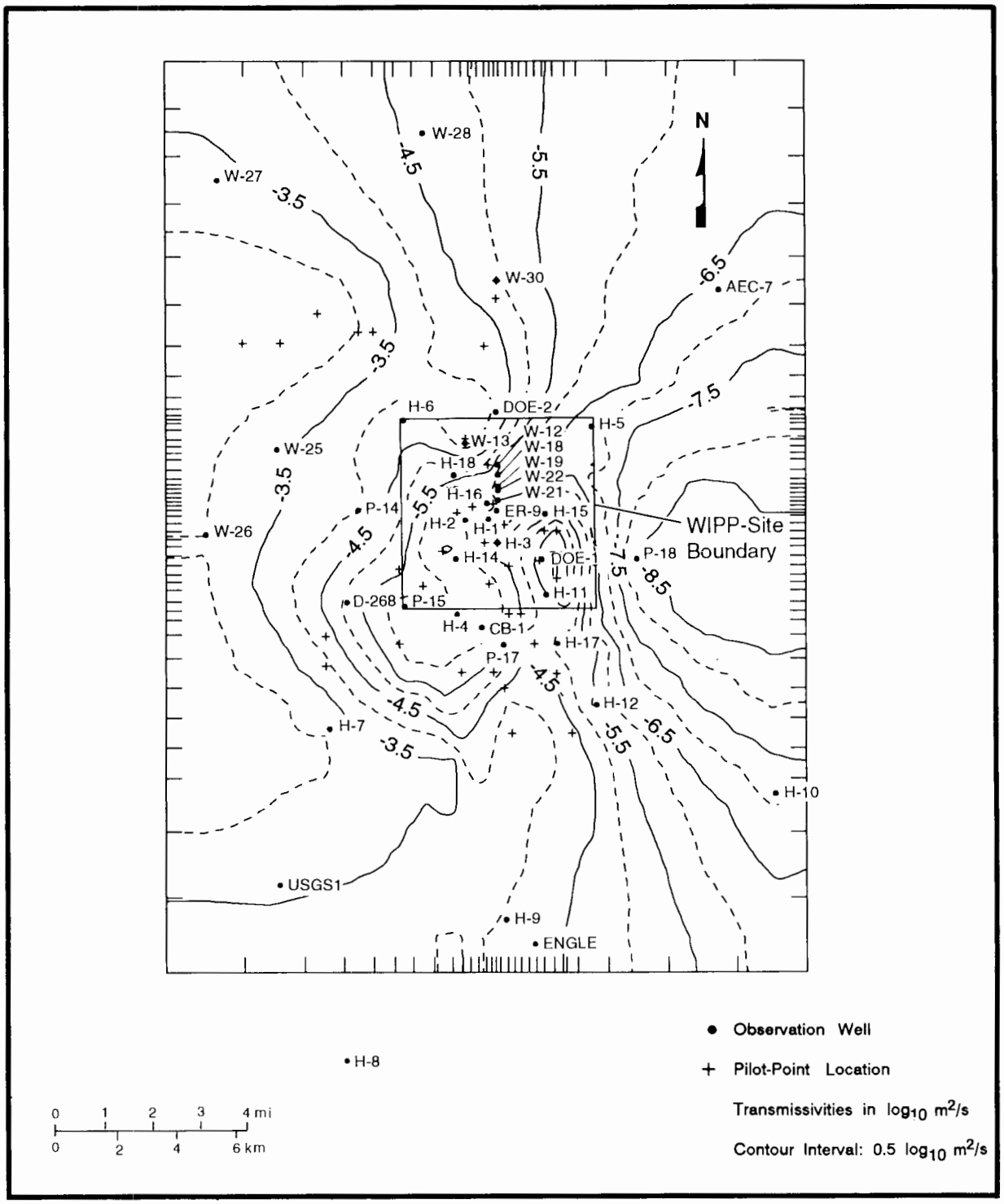

TRI-6342-3314-0

Figure 2-10. Transient calibrated $\log_{10}$ transmissivities (after LaVenue et al., 1990).

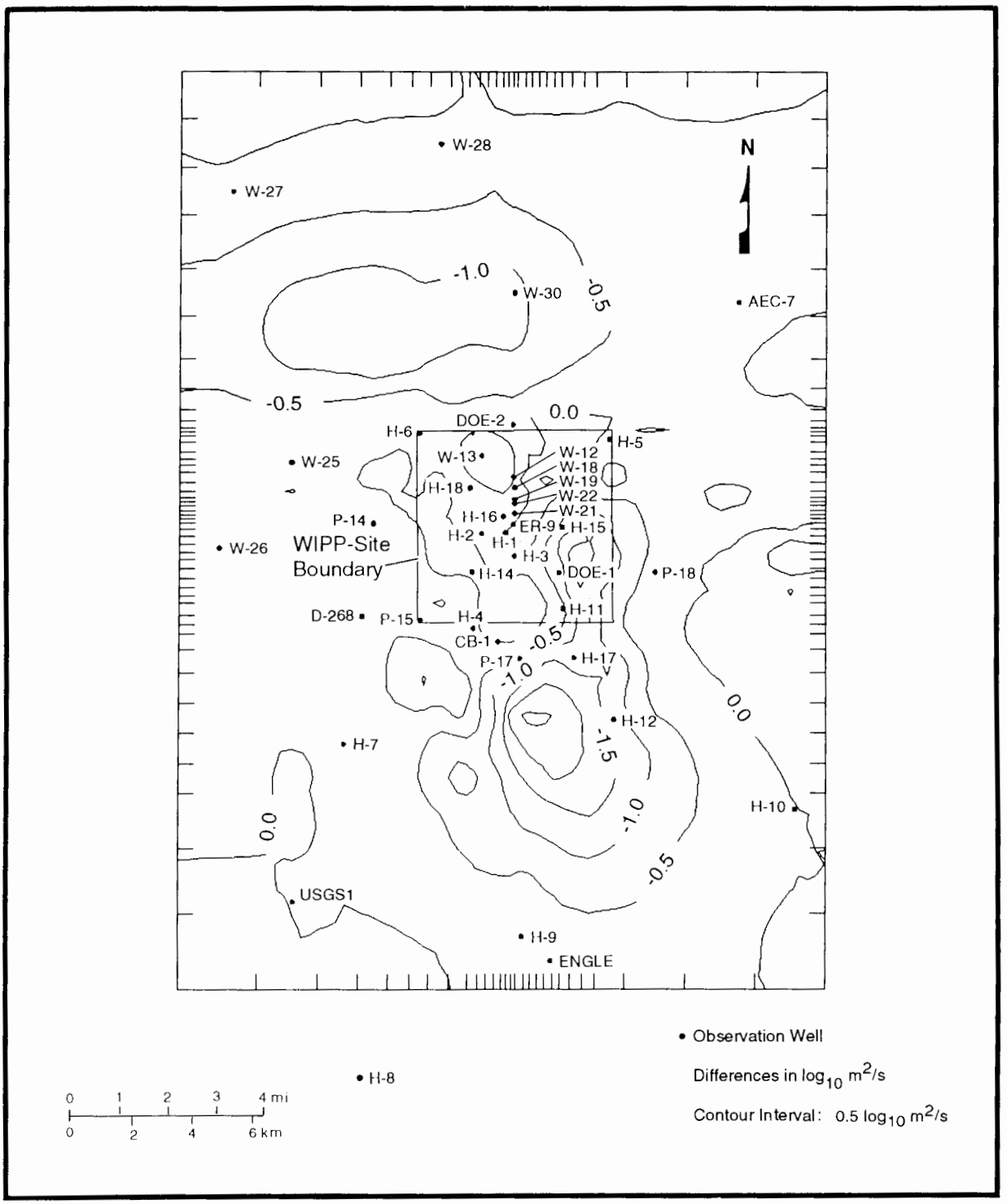

TRI-6342-3318-0

Figure 2-11. Difference between initial transmissivity field (Figure 2-9) and calibrated transmissivity field (Figure 2-10) determined in LaVenue et al. (1990).

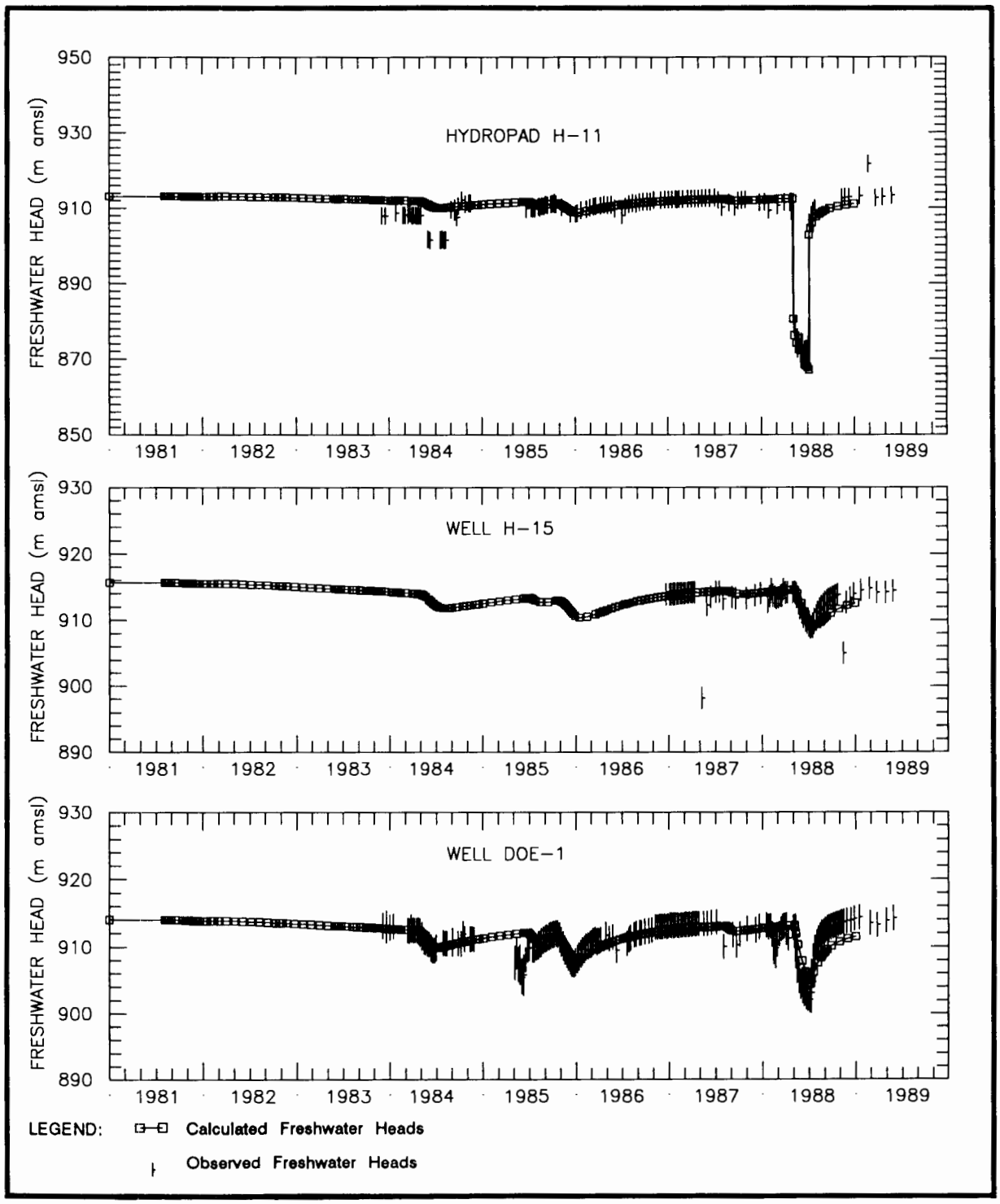

TRI-6342-3315-0

Figure 2-12. Calculated and observed transient freshwater heads at H-11, H-15, and DOE-1 using transient calibrated transmissivity field (after LaVenue et al., 1990).

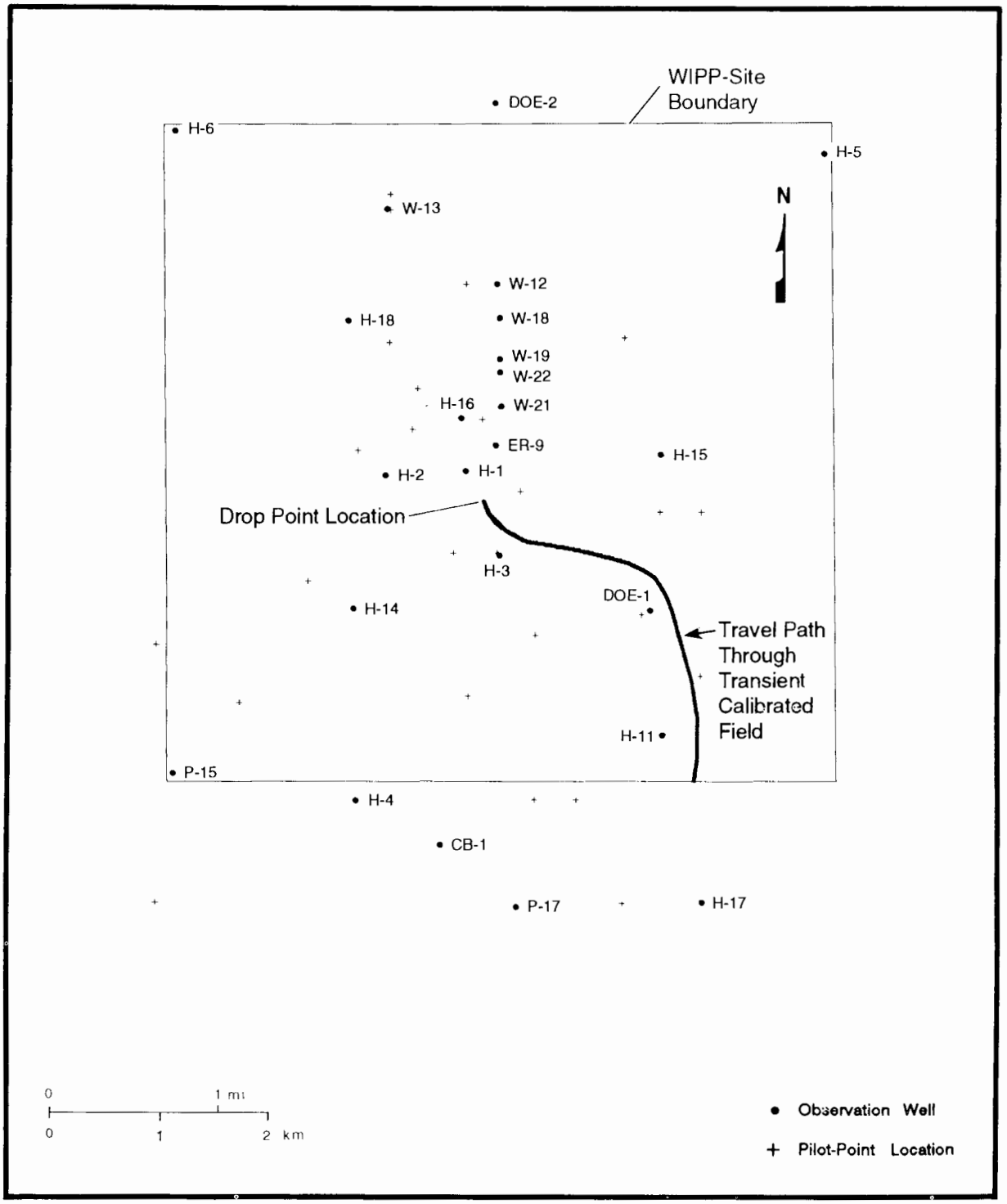

TRI-6342-3316-0

Figure 2-13. Particle travel path through the transient calibrated transmissivity field (after LaVenue et al., 1990).

In an effort to improve the transmissivity field used in the 1991 PA calculations, conditional simulations (CS) of Culebra transmissivity fields were produced by conditioning upon the observed transmissivity values and the pilot points that were added in the LaVenue et al. (1990) model. The CS transmissivity fields were then used in a groundwater flow model (WIPP PA Division, 1991). The boundary conditions necessary to reduce the differences between the observed and calculated steady-state heads were then iteratively determined. Those realizations that did not meet a minimum error criterion were not considered adequate and were discarded. This work resulted in over 60 conditional simulations that had acceptable fits to the observed steady-state freshwater heads and were subsequently used in the flow and mass-transport calculations. The 60 fields were partially ordered by travel time and selected by sampling on a uniformly distributed variable assigned to each CS field (WIPP PA Division, 1991). The associated groundwater travel times from a point within the Culebra that is coincident with the center of the waste panels to the southern WIPP-site boundary are illustrated in Figure 2-14.

In March of 1991, a geostatistics expert panel (GXG) was convened to provide guidance for adequately incorporating the uncertainty of the Culebra transmissivity field into the PA calculations. After reviewing the previous work, the GXG had several concerns regarding the approach taken in LaVenue et al. (1990). One of the principle concerns raised by the GXG panel members related to the subjectivity inherent in the manual calibration approach. For example, the model was calibrated in a piecewise fashion by sequentially selecting regions to be calibrated instead of calibrating the whole model area at the same time. The model was sequentially calibrated in the northwest (upgradient) region, southwest region, southern region, and central region or WIPP-site boundary area. As mentioned in the 1990 study, the regions upgradient and downgradient from the WIPP-site area were calibrated prior to making any changes within the WIPP-site boundary. This approach was employed in order to reproduce the regional hydraulic gradients across the northern and southern WIPP-site boundaries and is analogous to producing a regional flow model to provide boundary conditions for a local-scale model. The GXG panel wondered whether there would be any major differences in the calibrated transmissivity field had the entire model area been calibrated at the same time.

One of the recommendations proposed by the GXG panel members included repeating the modeling performed by LaVenue et al. (1990) numerous times. However, instead of simply kriging the transmissivities as in the LaVenue et al. (1990) study, conditional simulations would be generated and subsequently calibrated. The conditional simulations would allow for different transmissivity fields to be used as the initial fields for the model. These fields would initially be conditioned on the observed transmissivity data only. Subsequent model calibration would then condition each of the CS fields to the observed steady-state and transient heads. Since the GXG panel also expressed concerns regarding the manual assignment of transmissivities to the pilot points, the approach used in LaVenue et al. (1990) was also enhanced to include optimization routines to assign transmissivity values to the pilot points once their locations were selected.

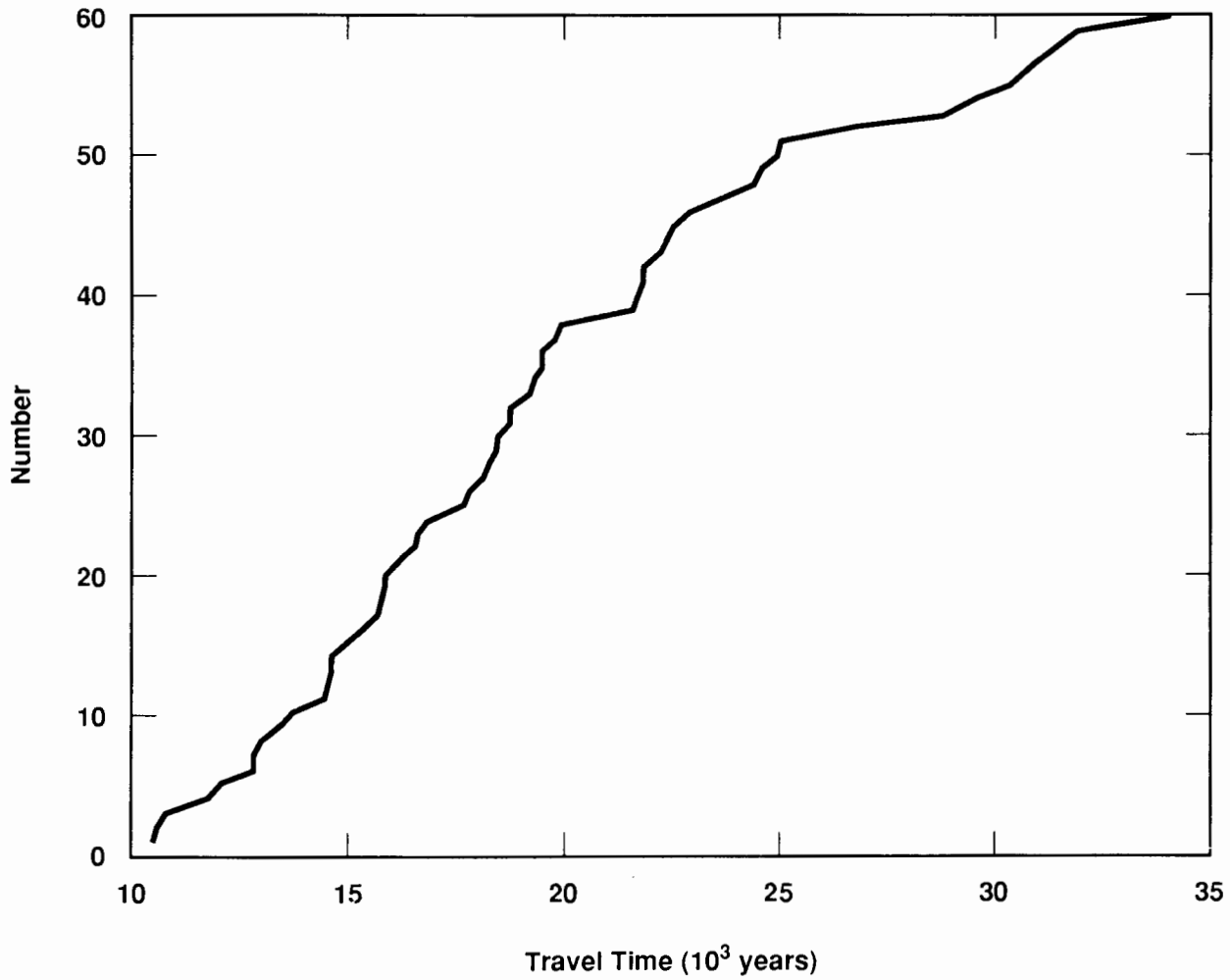

TRI-6342-1381-0

Figure 2-14. Cumulative distribution of travel times of the 60 flow fields used in 1991 performance assessment calculations (after WIPP PA Division, 1991).

3. METHODOLOGY

3.1 Uncertainty Analysis: Need and a Strategy

The groundwater travel time from a point in the Culebra Dolomite above the repository to a delineated accessible environment is a diagnostic measure used in the WIPP PA calculations. Groundwater travel time depends upon the assumed transmissivity distribution within the Culebra Dolomite. While transmissivities are measured at a few locations, those elsewhere are estimated. This estimation necessarily brings about an uncertainty in the transmissivities at all the locations where no measurements are made. The uncertainty in the unmeasured transmissivities propagates through the groundwater flow model to an uncertainty in travel time computations. The uncertainty in travel time, in turn, leads to uncertainty in the prediction of concentrations at the accessible environment boundary.

The present study addresses the uncertainty in the travel time by embedding the problem in a probabilistic framework. The "true transmissivity distribution" within the Culebra Dolomite is conceptualized to be one realization of a stochastic process. Accordingly, a large number of realizations of this stochastic process, which are plausible versions of the "true transmissivity" within the Culebra Dolomite, are generated. This "ensemble" of realizations is used with the groundwater flow model to generate an ensemble of the corresponding travel times. The distribution of the travel times provides an understanding of the uncertainty. While several statistical measures can be used to quantify the uncertainty, a cumulative distribution function (cdf) is commonly used for a graphical display of the uncertainty in travel time.

3.2 Analysis Methodology: An Overview

The solution methodology involves the application of the GRASP-INV code and the subsequent generation of a large number of random transmissivity fields, each of which is in close agreement with all the measured data within the Culebra Dolomite. The collected data comprise (1) transmissivity measurements and (2) pressure measurements (both steady and transient state). Conformity between a random transmissivity field and the measured data is achieved in stages, as described below. Figure 3-1 presents an overview of the methodology used in this study.

First, unconditional simulations of the Culebra transmissivity field are generated. These are random fields, having the same statistical moments (the mean and the variance) and the same spatial correlation structure as indicated by the transmissivity measurements. (These fields need not, however, match the measured transmissivities at the locations of their measurements.)

These transmissivity fields are then "conditioned," so that they honor exactly the measured Culebra transmissivities at the WIPP borehole locations. The resulting field may be referred to as a "conditional simulation" of the Culebra transmissivity field.

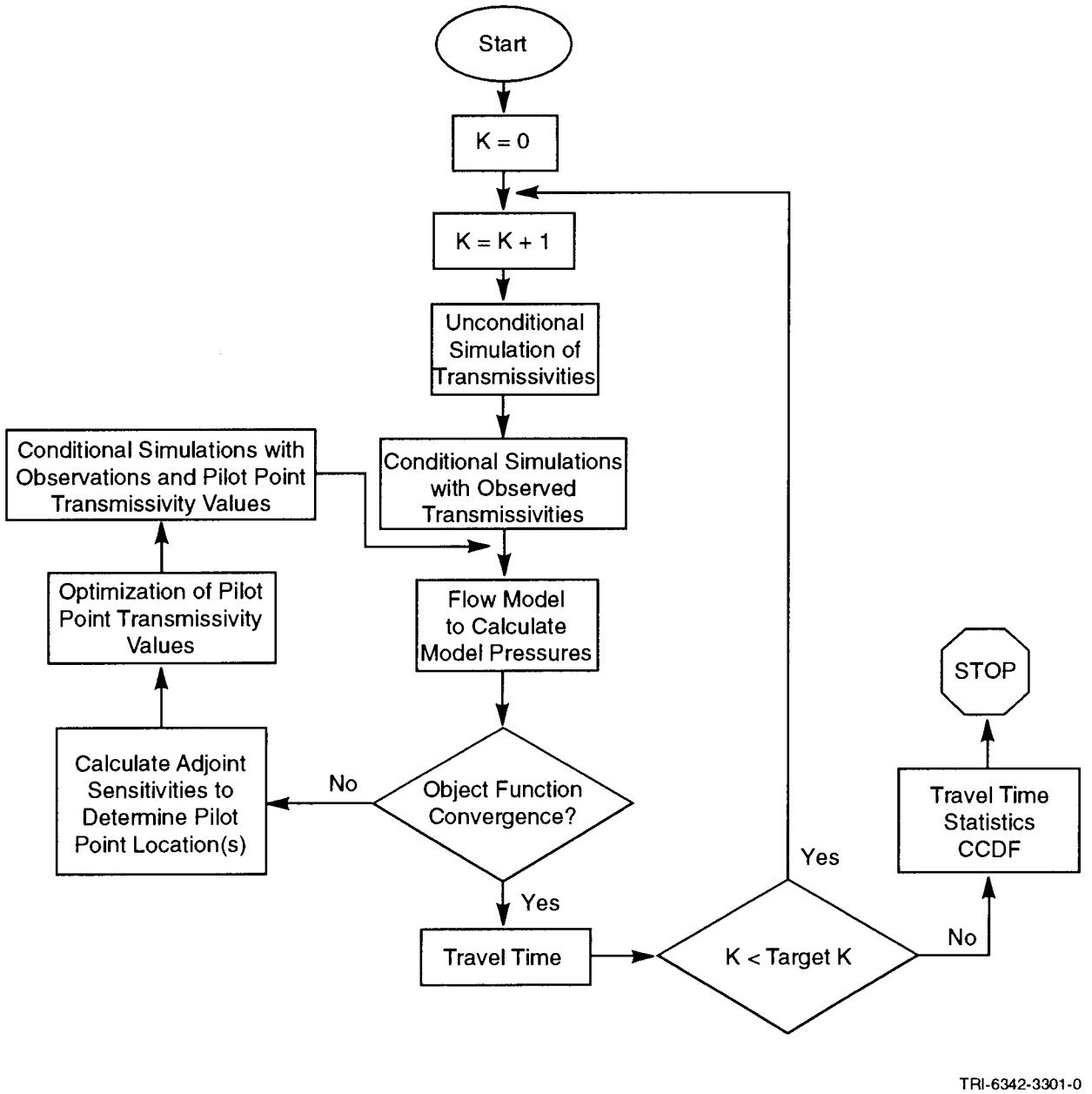

Figure 3-1. Flowchart illustrating calibration of conditionally simulated transmissivity fields.

The conditional simulations of the transmissivity field are then further "conditioned" such that the pressures computed by the groundwater flow model (both steady and transient state) agree closely with the "measured pressures," in a least-square sense. This phase is known as "calibration" or the solution of the "inverse problem" and accounts for a large part of the time and effort in this study. When the calibration is completed, one obtains a transmissivity field that is in conformity with all the data within the Culebra Dolomite and may therefore be regarded as a plausible version of the true distribution of transmissivity.

In this study, model calibration is approached indirectly. An objective function is defined as the weighted sum of the squared deviations between the model computed pressures and the observed pressures, with the summation extended in the spatial and temporal domain where pressure measurements are taken. The classical formulation of the calibration then requires the minimization of the objective function, subject to the constraints of the groundwater flow equations in the steady and transient state. This approach is implemented by iteratively adjusting the transmissivity distribution until the objective function is reduced to a prescribed minimum value.

A common approach to calibration consists of dividing the model domain into a few zones; in each of these zones, the transmissivity is treated as constant. The transmissivities in the different zones constitute the "parameters" to be adjusted in the optimization process. Clearly, the delineation of zones is a subjective process that affects the results of the calibration. Thus it may become necessary to consider several alternative zonation patterns for calibration. Also, in this approach, uniform transmissivities are assigned to each zone. This "representation" may be considered inadequate, particularly while addressing the issues of spatial variability (within a zone).

To avoid the above difficulties of the zonation approach, an approach using pilot points as parameters is adopted here. A pilot point is a synthetic transmissivity data point that is added to an existing measured transmissivity data set during the course of calibration. A pilot point is defined by its spatial location and by the transmissivity value assigned to it. After a pilot point is added to the transmissivity data set, the augmented data set is used to obtain kriged or CS transmissivity fields for a subsequent iteration in calibration. With the addition of a pilot point, the transmissivity distribution in the neighborhood of the pilot point is modified with dominant modifications being closer to the pilot-point location. The modifications in the different grid blocks are determined by kriging weights and are not uniform (as in the zonation approach). Conceptually, a pilot point may be viewed as a simple way to effect realistic modifications of transmissivity in the region of the model surrounding the pilot-point location. A coupled kriging and adjoint sensitivity analysis is used for the location of the pilot point and optimization algorithms are used for assigning the transmissivity of a pilot point. Thus the pilot-point approach to calibration has been rendered objective. Further, a multi-stage approach has been used in implementing this methodology.

3.3 Simulated Transmissivities

In the earlier modeling efforts for the Culebra Dolomite aquifer (Haug et al., 1987; LaVenue et al., 1988, 1990), kriging was employed to address the issue of spatial variability in transmissivity. In an effort in which only one calibrated field is to be produced, kriging becomes an obvious choice. Kriging provides an optimal estimate of the transmissivity at a point, i.e., the mean value. In an attempt to reproduce the natural variability of transmissivity fields, a simulation of the transmissivity field is conducted. Simulated transmissivity values reproduce the fluctuation patterns in transmissivity, which may lead to extreme values in travel times. Thus simulated fields are

useful to resolve the residual uncertainty not addressed by kriging. Figure 3-2 taken from Journel and Huijbregts (1978) provides a relationship between the true, kriged, and simulated fields.

3.3.1 Unconditional Simulations

An unconditional simulation of a transmissivity field produces a random field with the same statistical moments (mean and variance) and the same spatial correlation structure as indicated by the measured transmissivities in the field. An unconditionally simulated transmissivity field is said to be isomorphic with the true field and is independent of the true field. The following methods have been used earlier in groundwater hydrology for generating unconditional simulations:

- Nearest neighbor method (Smith and Schwartz, 1981; Smith and Freeze, 1979)
- Matrix decomposition (Wilson, 1979)
- Multidimensional spectral analysis (Shinozuka and Jan, 1972; Mejia and Rodríguez-Iturbe, 1974)
- Turning bands method (Matheron, 1971, 1973; Mantoglou and Wilson, 1982; Zimmerman and Wilson, 1990)

In this study, the Turning Bands Method and the TUBA code (Zimmerman and Wilson, 1990) have been used to generate $\log_{10}$ transmissivity fields.

GENERAL METHODOLOGY OF TURNING BANDS METHOD

A two-dimensional (or a three-dimensional) stochastic process is generated in the Turning Bands Method by the summation of a series of equivalent one-dimensional processes. Figure 3-3 illustrates this point. The region P shows a grid of points at which the two-dimensional field is to be generated. In particular, consider a point N in the grid where the two-dimensional field $[Z_s(N)]$ is to be simulated. Also consider a particular line i, the length along which, from the origin O, is measured by ζ_i. This line is divided into a number of intervals (bands), of length $\Delta\zeta_i$; for each, the one-dimensional process Z_i is computed. Let N_i be the projection of the point N onto the line i. Let $Z_i(\zeta_i)$ be the one-dimensional process in the band containing N_i. Then the two-dimensional process, $[Z_s(N)]$, is obtained by summing the contributions from the different lines, by the relation

$$Z_s(N) = \frac{\sum_{i=1}^{L} Z_i\left(\zeta_{N_i}\right)}{\sqrt{L}}, \tag{3-1}$$

where L is the number of lines selected. Usually L is between 16 and 20.

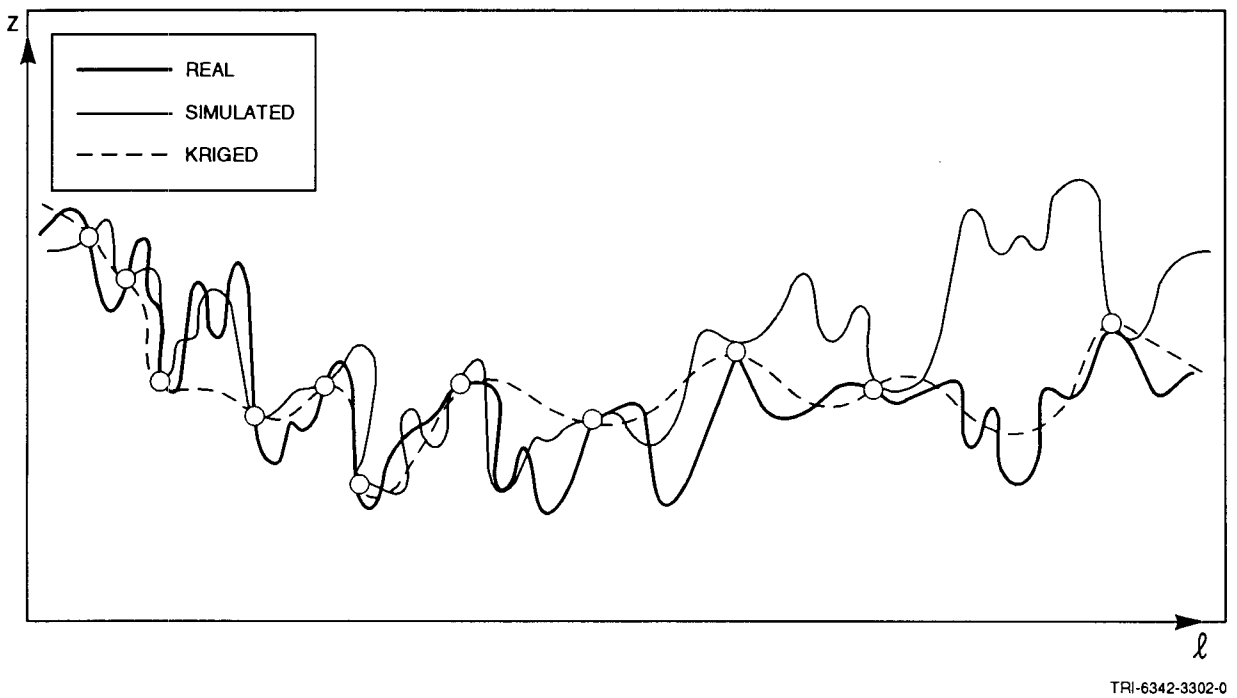

Figure 3-2. Schematic of real, simulated, and kriged fields.

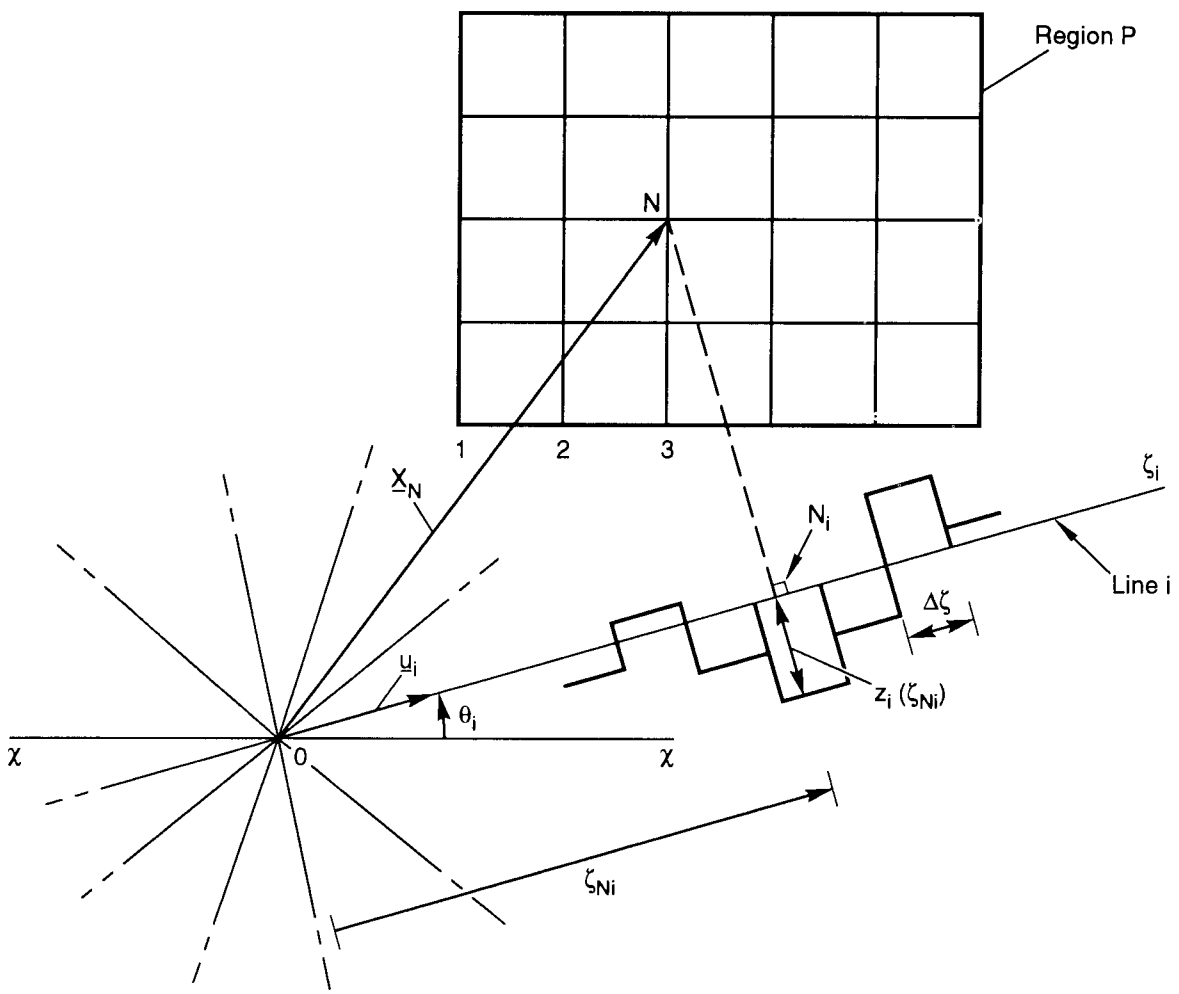

TRI-6342-3303-0

Figure 3-3. Schematic representation of the field and turning bands lines (after Mantoglou and Wilson, 1982).

WEINER-LEVY PROCESS

LaVenue et al. (1990) analyzed the Culebra transmissivity data and determined that the spatial structure of the two-dimensional transmissivity field could be represented by an isotropic process with an intrinsic random function of order zero (IRF-0), and a generalized covariance function (GCF) given by

$$k_2(r) = -a_0 r(\mathrm{GCF}) \tag{3-2}$$

where r is a radial distance, a_0 is a constant, and k_2 indicates a two-dimensional process.

If $k_1(r)$ is the GCF for an equivalent one-dimensional process, then

$$k_1(r) = -\left(\frac{\pi}{2}\right) a_0 r\,. \tag{3-3}$$

The Weiner-Levy process is known to be an IRF-0 process and is accordingly used to generate the line process. The relevant equations are given below.

$$Z_i(\zeta) = W(\zeta), \tag{3-4}$$

where $W(\zeta)$ is the Weiner-Levy Process.

$$W(0) = 0, \tag{3-5}$$

$$W(\zeta + \Delta\zeta) = W(\zeta) + gU(\zeta), \tag{3-6}$$

$$U(\zeta) = U\left[-\frac{1}{2}, \frac{1}{2}\right], \tag{3-7}$$

and

$$g = \sqrt{12\pi a_0 \Delta\zeta}, \tag{3-8}$$

where $U(\zeta)$ is a uniformly distributed random variable.

3.3.2 Conditional Simulations

An unconditionally simulated transmissivity field that is made to honor exactly the measured transmissivity at the locations of the measurements is called a conditionally simulated (CS) transmissivity field. The procedure of conditioning is described below.

Let $Z(x)$ be the true value (not known) of the field at a point x. One may decompose $Z(x)$ as below:

$$Z(x) = Z_{ok}(x) + [Z(x) - Z_{ok}(x)], \tag{3-9}$$

where $Z_{ok}(x)$ is the kriged estimate of Z, at x, based on the observed values of Z at the locations of the observations. Here, $[Z(x) - Z_{ok}(x)]$ is a true kriging error and is unknown, since the true value of $Z(x)$ is unknown. It is possible to simulate this error.

Using the unconditionally simulated values (Z_{uc}) at the locations of the observations (not the actual values at the observations), a kriged field (Z_{uk}) is generated. One may write, using a similar decomposition as above,

$$Z_{uc}(x) = Z_{uk}(x) + [Z_{uc}(x) - Z_{uk}(x)] \ , \tag{3-10}$$

where $[Z_{uc}(x) - Z_{uk}(x)]$ is also a kriging error, is known, and may be called a simulated kriging error. This error is isomorphic with the true kriging error. More important, this error is independent of the kriged values:

$$E\{Z_{ok}(x), [Z_{uc}(y) - Z_{uk}(y)]\} = 0 \text{ for all x,y .} \tag{3-11}$$

Substituting the known simulated kriging error for the true but unknown kriging error, in Equation 3-9, one obtains:

$$Z_{cs}(x) \approx Z_{ok}(x) + [Z_{uc}(x) - Z_{uk}(x)] \tag{3-12}$$

Equation 3-12 clarifies the conditioning step as one in which simulated kriging errors are added on a kriged field using the measured data. This step involves kriging twice, once with the measured transmissivities and another time with the unconditionally simulated transmissivities, both at the location of the observations. The superposition of the three different transmissivity fields is graphically illustrated in Figure 3-4.

Because the CS values of transmissivity are meant to be used as input to a finite-difference flow model, the CS transmissivity values assigned to the grid block must represent the average value over the area of the grid block. In order to accomplish this, each finite-difference grid block is divided by a 2x2 Gauss quadrature grid. All the geostatistical computations are conducted at the Gauss grid scale. Once the CS values are obtained, Gauss quadrature integration is employed to determine the average CS value assigned to the flow model grid block.

$$Z_{CS}(x) \approx Z_{OK}(x) + [Z_{UC}(x) - Z_{UK}(x)]$$

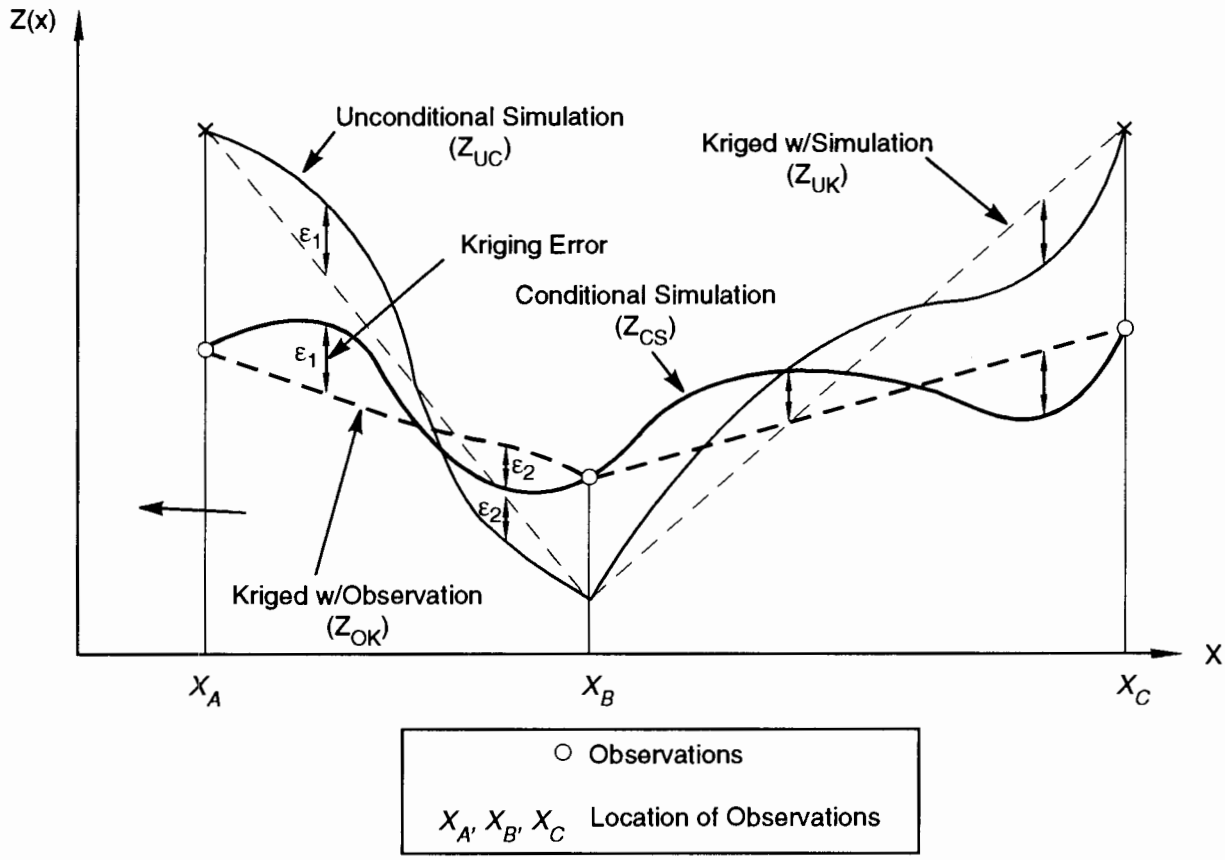

TRI-6342-3304-0

Figure 3-4. Relationships between conditional and unconditional simulation.

The conditional simulations constitute the most important input to the groundwater flow model. It is useful to appreciate the following properties of a conditional simulation:

1. **The CS field honors the measured values exactly at the measurement locations.** This follows from the fact that kriging is an exact interpolator, so that the simulated kriging error is zero at measurement locations and the kriged value from observations, (Z_{ok}), reduces to the measured value for the same reason.

2. **The CS field has the same spatial correlation structure as indicated by the measured data.** This follows from an orthogonality property of the kriging errors (Equation 3-11), which states that the kriging errors (both true and simulated) are uncorrelated with any kriged values for stationary fields and with generalized increments for the intrinsic fields (Delfiner, 1976; Delhomme, 1979).

3. **The average of many CS fields at a location x will approach the kriged estimate at x** $[Z_{ok}(x)]$ **as the number of fields becomes statistically significant.**

4. **The variance of many CS fields at a location x is given by the kriging variance.**

5. **The CS fields reproduce the true variability of the field, in contrast to a smoothed field given by kriging.**

6. **The conditioning step imposes the features observed within the measured data that are not specifically represented in the (unconditionally) simulated field.**

3.3.3 Simulated Fields: Computational Options

There are several options for the simulated kriging error that can be used in the GRASP-INV code while constructing a conditional simulation. For example, the simulated kriging error can be rendered zero at all observation points (see Figure 3-4). When a pilot point is added to the observed transmissivity data set, two options exist:

1. The pilot point may be given the full status of an observed data point. Then the simulated kriging error at the pilot point is also rendered zero. In this case, the simulated kriged error field varies from one iteration to the other, and needs to be computed at every iteration.

2. The simulated kriging error is rendered zero only at the observed data point and not at the pilot points. Thus, the pilot points are used to obtain the kriged field using the "augmented" data. But the simulated kriged error field remains the same as the initial field, through all the iterations. It does not need to be recomputed during the various iterations.

During this study, Option 2 was used. Another set of options exists while obtaining the kriged field using the simulated data at the measurement locations. These options are:

1. Assume that the simulated values (Z_{uc}) have the same errors as the actual measurements.

2. Assume that the simulated values (Z_{uc}) have no errors.

During this study, Option 1 was employed while obtaining the simulated kriged field.

3.3.4 Validation of Simulations

To verify that the generated simulations' geostatistical structure is approximately the same as the observed data, the mean and variance of the $\log_{10}$ transmissivity are computed and compared with that of the Culebra data for a select number of simulations. Also, using the code AKRIP, the generalized covariance function (GCF) of the field is obtained and is compared with that obtained from measured data in the Culebra. A close agreement between the two provides verification that the generated CS transmissivity field is a plausible version of the reality within the Culebra.

A collection of all the generated CS fields constitutes an ensemble. For any one location in the field, transmissivity values across all the fields in the ensemble are studied and their mean and variance computed. A spatial distribution of the ensemble mean and variance should closely agree with the spatial distribution of kriged values and kriging variance obtained from the kriging exercise itself (Delhomme, 1979).

3.4 Automated Calibration

An overview of the automated calibration, the zonation approach, and pilot-point methodology has been presented in Section 3.2. The computational details of the automated algorithm used to guide the calibration are given here.

In an automatic algorithm, it becomes necessary to restrict the number of parameters to be identified to a small number. This step is referred to as parameterization. The zonation approach and the pilot-point methodology can both be viewed as two alternative paths for parameterization. As discussed in Section 3.2, the pilot-point approach used in GRASP-INV eliminates an inherent subjectivity in the zonation approach.

3.4.1 Objective Function

The objective function that is minimized during calibration is a weighted least square error criterion function. It comprises two components, a model fit criterion and a plausibility criterion. The model fit criterion is a weighted sum of the squared deviations between the computed and measured pressures taken over all points in spatial and temporal domains, where pressure measurements have been made. The plausibility criterion demands that the

calibrated transmissivities are not too far from their prior estimates. A relative weight η between the plausibility criterion and the model fit criterion has been used. Because of the nature of the pilot-point methodology (Marsily, de, et al., 1984), the plausibility criterion in this study is disregarded by setting $\eta = 0$. But the GRASP-INV code has the capability to use $\eta \neq 0$. (Note: the "degrees of freedom" of the inverse solution is prescribed by the number of pilot points 478used in the pilot-point methodology.)

Equation 3-13 defines the objective function in general terms:

$$J(\underline{u}) = \sum_{k=1}^{L} \underline{e}_p^T(k)\underline{\underline{R}}^{-1}(k)\underline{e}_p(k) \quad \text{(model fit)}$$

$$+ \eta \bullet \underline{e}_u^T \bullet \underline{\underline{U}}^{-1} \bullet \underline{e}_u \qquad \text{(plausibility)}, \tag{3-13}$$

where:

$J(\underline{u})$ = weighted least squares (WLS) error criterion function
$\underline{e}_p$ = $\left\{\underline{p}(k) - \underline{p}_{ob}(k)\right\}$
$\underline{e}_u$ = $\left\{\underline{u} - \underline{u}_{est}\right\}$
$\underline{\underline{R}}$ = covariance matrix of errors in $\underline{p}_{ob}$
$\underline{\underline{U}}$ = covariance matrix of errors in $\underline{u}$
$\underline{u}$ = vector of parameters ($Y_p = \log_{10} T_p$)
η = relative weight of the plausibility criterion to model fit criterion
k = time step number
$\underline{p}(k)$ = pressures computed
$\underline{p}_{ob}(k)$ = pressures observed
T = transpose
T_p = pilot point transmissivity
L = number of time steps.

After optimal estimates of $\underline{u}$ are obtained, the posterior covariance matrix of the parameters is given by

$$\underline{\underline{P}}_{uu} = \left\{ \sum_{k=1}^{L} \underline{\underline{S}}^T(k)\underline{\underline{R}}^{-1}(k)\underline{\underline{S}}(k) + \underline{\underline{U}}^{-1} \right\}^{-1} \tag{3-14}$$

$$\underline{\underline{S}}_k = \text{Jacobian Matrix} = \left[\frac{dp(k)}{d\underline{u}'} \right],$$

where $\underline{\underline{P}}_{uu}$ is the posterior covariance matrix of the parameters.

3.4.2 Parameters of Calibration

The pilot-point transmissivities are the parameters that are adjusted for calibration. However, in the mathematical implementation, the logarithms (to base 10) of the transmissivities (and not the transmissivity) are treated as parameters. The calibration parameters are given by

$$Y_p = \log_{10} T_p \ ,$$

where T_p is the transmissivity at a pilot point (suffix p denotes pilot point). Figure 3-5 illustrates the concepts of pilot points presented in Section 3.2.

3.4.3 Pilot-Point Location

Pilot points are placed at locations where their potential for reducing the objective function is the highest. This potential is quantified by the sensitivity coefficients (dJ/dY) of the objective function J, with respect to Y, the logarithm (to base 10) of pilot-point transmissivity. A large number of candidate pilot points are considered, usually the centroids of all the grid blocks in the flow model grid. The selected candidate pilot points are ranked in descending order of the magnitude of their absolute sensitivity coefficients, i.e., $|dJ/dY|$. The selected number of pilot points chosen to be added during each iteration in the calibration process is selected from the top of the ranked list of points. Coupled adjoint sensitivity analysis and kriging is used to compute the required derivatives and the procedure is documented in RamaRao and Reeves (1990). It is described briefly in this section.

KRIGING

As mentioned in Section 3.3.2, the geostatistical computations are conducted at each Gauss grid center point. Integration is then employed to determine the average value assigned to the flow model grid blocks. The kriging equations presented below use point estimates for this reason.

Let P be a pilot point added to a set of N observation points. Let T_p be the transmissivity assigned to pilot point P. Kriging is done using Y_p, where

$$Y_p = \log_{10} T_p \ . \tag{3-15}$$

The kriged estimate (Y^*) at the centroid of a Gauss grid center point m is given by

$$Y_m^* = \sum_{k=1}^{N} \gamma_{m,k} \, Y_k + \gamma_{m,p} \, Y_p \ , \tag{3-16}$$

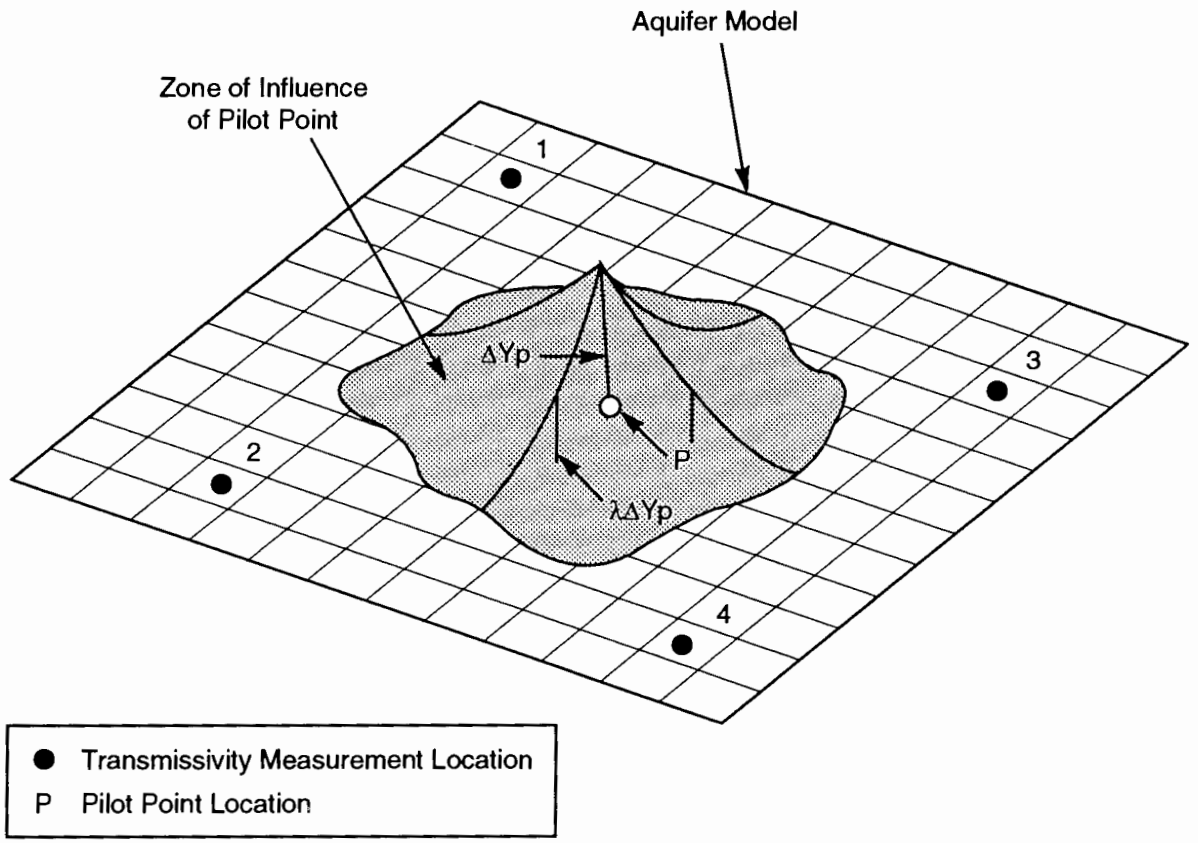

Pilot Point - Schematic

		X	Y	T	y	σ_y
Measured Transmissivity	1	150	1050	$10^{-3.1}$	-3.1	0.5
	2					
	⋮					
	4					
Pilot Points added in Calibration	P_1	650	620	$10^{-4.81}$	-4.81	0.84
	P_2					
	⋮					
	P_n					

TRI-6342-3305-0

Figure 3-5. Pilot-point schematic.

where k is the subscript for an observation point, p is the subscript for pilot point, $\gamma_{m,k}$ is the kriging weight between the interpolation point m and data point k, and $\gamma_{m,p}$ is the kriging weight between interpolation point m and pilot point p.

When a pilot-point transmissivity is perturbed, the kriged transmissivities and hence the CS values in all grid blocks are altered, causing the objective function J to change. Let $\overline{Y}_m^*$ represent the CS value assigned to grid block m. Using the chain rule,

$$\frac{dJ}{dY_p} = \sum_{m=1}^{M} \frac{dJ}{d\overline{Y}_m^*} \frac{d\overline{Y}_m^*}{dY_p} , \tag{3-17}$$

where M is the total number of grid blocks in the flow model.

$$\frac{d\overline{Y}_m^*}{dY_p} = \overline{\gamma}_{m,p}$$

where $\overline{\gamma}_{m,p}$ is the average linear weight between a pilot point and the area over a finite-difference grid block.

$$\frac{dJ}{dY_p} = \sum_{m=1}^{M} \frac{dJ}{d\overline{Y}_m^*} \bullet \overline{\gamma}_{m,p} \tag{3-18}$$

$$\overline{Y}_m^* = \log_{10}\left(\overline{T}_m^*\right)$$

$$\overline{T}_m^* = K_m \frac{\rho_m}{\mu_m} g b_m$$

$$\frac{dJ}{d\overline{Y}_m^*} = \ln(10) K_m \frac{dJ}{dK_m} \tag{3-19}$$

where T^* is the CS transmissivity, K is the CS permeability, ρ is fluid density, μ is fluid viscosity, g is acceleration due to gravity, b is grid block thickness, and m is the subscript denoting grid block.

Combining Equations 3-18 and 3-19 yields

$$\frac{dJ}{dY_p} = \ln(10) \sum_{m=1}^{M} \overline{\gamma}_{m,p} K_m \frac{dJ}{dK_m} \tag{3-20}$$

The sensitivity coefficient, dJ/dK_m of the objective function with respect to the permeability in a grid block m, is obtained by adjoint sensitivity analysis.

ADJOINT SENSITIVITY ANALYSIS

Adjoint sensitivity analysis provides an extremely efficient algorithm for computing sensitivity coefficients between a given objective function J and a large number of parameters (permeabilities in thousands of grid blocks as is the case here).

Let the groundwater flow model be represented by the following matrix equation:

$$\underline{\underline{A}}\,\underline{p}^n = \underline{\underline{B}}\,\underline{p}^{n-1} + \underline{f}^n \ , \tag{3-21}$$

where for a fully implicit scheme of time integration adopted here:

$\underline{p}$ = vector of gridblock pressures
$\underline{\underline{A}}$ = $\underline{\underline{C}} + \underline{\underline{B}}$
$\underline{\underline{B}}$ = $\underline{\underline{S}}/\Delta t$
$\underline{\underline{C}}$ = conductance matrix
$\underline{\underline{S}}$ = storativity matrix
$\underline{f}^n$ = vector of source terms
Δt = $t^n - t^{n-1}$
t = time
n = time level $(1,2,3\ldots L)$
L = maximum time level of the simulation.

First, an adjoint state vector $\{\lambda\}$ is obtained by the solution of the following equation:

$$\underline{\underline{A}}\,\underline{\lambda}^{n-1} = \underline{\underline{B}}\,\underline{\lambda}^n + \left[\frac{\partial J}{\partial \underline{p}^n}\right]^T \ , \tag{3-22}$$

where T denotes the transpose of the matrix.

The equation J = objective function (performance measure) is solved backwards in time, from $n = L$ to $n = 1$ with

$$\underline{\lambda}^L = 0 \ . \tag{3-23}$$

If α_i is a generic sensitivity parameter in the gridblock i, the sensitivity coefficient $dJ/d\alpha_i$ is evaluated by the expression:

$$\frac{dJ}{d\alpha_i} = \frac{\partial J}{\partial \alpha_i} + \sum_{n=1}^{L} \underline{\lambda}^{nT} \bullet \left[\frac{\partial \underline{\underline{A}}}{\partial \alpha_i} \underline{p}^n - \frac{\partial \underline{\underline{B}}}{\partial \alpha_i} \underline{p}^{n-1} - \frac{\partial \underline{f}^n}{\partial \alpha_i} \right] . \tag{3-24}$$

Here, Equation 3-24 is evaluated with $\alpha_i = K_i$, the permeability in the grid block.

3.4.4 Pilot-Point Transmissivities: Optimization

The transmissivities at pilot points are assigned by an unconstrained optimization algorithm and a subsequent imposition of constraints. The optimization algorithm chosen here belongs to a class of iterative search algorithms. It involves a repeated application of the following equation until convergence is achieved:

$$\underline{Y}_{i+1} = \underline{Y}_i + \beta_i \bullet \underline{d}_i , \tag{3-25}$$

where i is the iteration index, $\underline{d}_i$ is the direction vector, β_i is the step length (a scalar), and $\underline{Y}_i$ is the vector of parameters to be optimized (i.e., logarithms of pilot-point transmissivities to base 10).

The steps in the implementation of this algorithm are as follows:

1. For the selected number of pilot points, choose the initial estimates of the pilot-point $\log_{10}$ transmissivity ($Y_p = \log_{10} T_p$). These are taken to be the kriged or the CS values in the gridblocks where pilot points are located depending upon the option (Section 3.3.3) chosen.

2. Compute the direction vector, $\underline{d}_i$, as per one of the three algorithms discussed below (Fletcher-Reeves, Broyden's, or Davidon-Fletcher-Powell). The direction vector constitutes a direction in the hyperspace of the parameters. By advancing along the direction vector, the new values of the parameters are obtained. The step length β determines the actual advance along this direction.

3. Determine the optimal step length β, which minimizes the objective function. (Details are given below in the section titled "Step Length: β_i").

$$\min_{\beta_i} J(\underline{Y}_{i+1}) = J(\underline{Y}_i + \beta_i \underline{d}_i)$$

4. Update the parameters:

$$\underline{Y}_{i+1} = \underline{Y}_i + \beta_i \underline{d}_i$$

   Impose the constraints (Section 3.4.5).

5. Check for convergence (see Section 3.4.6).

6. If convergence is achieved, the optimization algorithm is completed and the pilot points are added to the data and the execution of the main algorithm continues.

7. If convergence is not achieved, let $i = i + 1$ and go to Step 8.

8. Using the augmented data set, generate a new conditional simulation of transmissivity field, derive the corresponding pressure field, and recompute the gradient vector using the already selected pilot point locations. (The pilot point selection process will be skipped.)

9. Go to Step 2.

DIRECTION VECTOR: $\underline{d}_i$

The code includes three options for the computation of the direction vector $\underline{d}_i$. They are the algorithms due to (1) Fletcher-Reeves, (2) Broyden, and (3) Davidon-Fletcher-Powell (Luenberger, 1973; Gill et al., 1981; Carrera and Neuman, 1986).

Fletcher-Reeves Algorithm

This method generates in successive iterations, a sequence of direction vectors, which are conjugate to each other with respect to the Hessian Matrix $[H]$. The Hessian Matrix is a matrix of second order partial derivatives of J with respect to calibration parameters (e.g., pilot-point transmissivities).

$$\underline{d}_i^T \underline{\underline{H}} \underline{d}_j = 0, \tag{3-26}$$

$$H_{ij} = \frac{\partial^2 J}{\partial Y_i Y_j}. \tag{3-27}$$

Initially (for $i = 1$) the direction vector is taken to be negative gradient. For subsequent iterations, the direction vector is calculated as shown. But after every N iterations, N being the number of parameters (pilot points), a pacer iteration is introduced, where the direction vector is reset to the negative of the gradient vector:

$$\underline{d} = -\underline{g}_i; \qquad i = 1, n+1, 2n+1, \ldots, \tag{3-28}$$

$$\underline{d}_i = -\underline{g}_i + \beta_i \underline{d}_{i-1}, \tag{3-29}$$

$$\beta_i = \frac{\left(\underline{g}_i^T \underline{g}_i\right)}{\left(\underline{g}_{i-1}^T \underline{g}_{i-1}\right)} \qquad \text{(scalar).} \tag{3-30}$$

Broyden's Algorithm

Broyden's algorithm belongs to a class of variable metric family of algorithms. It is also called a quasi-Newton algorithm. Here a transformation matrix $\underline{\underline{B}}$ is updated at every iteration. The direction vector $\underline{d}_i$ is obtained from $\underline{\underline{B}}$, as

$$\underline{d}_i = -\underline{\underline{B}}_i \bullet \underline{g}_i. \tag{3-31}$$

The matrix $\underline{\underline{B}}$ is an approximation to the true inverse Hessian Matrix used in Newton and Gauss-Newton methods:

$$\underline{\underline{B}}_i = \underline{\underline{U}} \text{ or } \underline{\underline{I}}; \quad i = I, \tag{3-32}$$

where $\underline{\underline{U}}$ is the prior covariance matrix of the parameters, and $\underline{\underline{I}}$ is the identity matrix.

$$\underline{\underline{B}}_{i+1} = \left[\underline{\underline{B}}_i - \frac{\underline{\underline{B}}_i \underline{Q}_i d_i^T + \underline{d}_i \underline{Q}_i^T \underline{\underline{B}}_i}{\underline{d}_i^T \underline{Q}} \right] r_i + \left[\beta_i + \frac{r_i \underline{Q}^T \underline{\underline{B}}_i \underline{Q}}{\underline{d}_i^T \underline{Q}^T} \right] \frac{\underline{d}_i \underline{d}_i^T}{\underline{d}_i^T \underline{Q}_i}, \tag{3-33}$$

where

$$r = 1 \qquad \text{if } i > 2,$$

$$r = \frac{\underline{d}_i^T \underline{Q}_i}{\underline{Q}_i^T \underline{\underline{B}}_i \underline{Q}_i} \qquad \text{if } i = 2,$$

and

$$\underline{\underline{Q}}_i = \underline{g}_{i+1} - \underline{g}_i.$$

Davidon-Fletcher-Powell Algorithm

The Davidon-Fletcher-Powell algorithm is similar to Broyden's algorithm in that the direction is computed by:

$$\underline{d}_i = -\underline{\underline{B}}_i \bullet \underline{g}_i \ .$$

However, the Davidon-Fletcher-Powell algorithm differs from the Broyden algorithm in the way the approximation to the true inverse Hessian is constructed.

$$\underline{\underline{B}}_{i+1} = \left[\underline{\underline{B}}_i - \frac{\left(\underline{\underline{B}}_i \underline{q}_i\right)\left(\underline{\underline{B}}_i \underline{q}_i\right)^T}{\underline{q}_i^T \left(\underline{\underline{B}}_i \underline{q}_i\right)} \right] + \frac{\underline{h}_i \underline{h}_i^T}{\underline{h}_i^T q_i}, \tag{3-34}$$

where

$$\begin{aligned} \underline{h}_i &= \underline{Y}_{i+1} - \underline{Y}_i \\ \underline{\underline{B}}_i &= \underline{\underline{I}} \text{ or } \underline{\underline{U}}; \quad i = 0, N+1, 2N+1 \\ \underline{q}_i &= \underline{g}_{i+1} - \underline{g}_i \ . \end{aligned}$$

At each iteration, a check is made to verify that $\underline{p}_i^T \underline{q}_i > 0$.

STEP LENGTH: β_i

The step length β_i, (a scalar) is determined by:

$$\min_{\beta_i} J(\underline{Y}_{i+1}) = J(\underline{Y}_i + \beta_i \underline{d}_i). \tag{3-35}$$

Thus, β_i is obtained by solving

$$\frac{\partial J(\underline{Y}_{i+1})}{\partial \beta_i} = 0. \tag{3-36}$$

The first-order Taylor expansion for $\underline{p}(\underline{Y}_{i+1})$ gives:

$$\underline{p}(\underline{Y}_{i+1}) = \underline{p}(\underline{Y}_i) + \frac{\partial \underline{p}(\underline{Y}_{i+1})}{\partial \beta_i} \bullet \beta_i \ . \tag{3-37}$$

(For $\underline{p}$, the time level k is suppressed.)

Also,

$$\underline{Y}_{i+1} = \underline{Y}_i + \beta_i \underline{d}_i,$$

so that

$$\frac{\partial \underline{Y}_{i+1}}{\partial \beta_i} = \underline{d}_i. \tag{3-38}$$

Using the Equations 3-36, 3-37, and 3-38, one may obtain (k = time level index)

$$\beta_i = \frac{\left[\sum_k \underline{e}_p^T(k) R^{-1}(k) \underline{q}(k) + \underline{e}_u^T \underline{\underline{U}}^{-1} \underline{d}_i\right]}{\left[\sum_k \underline{q}^T(k) R^{-1}(k) \underline{q}(k) + \underline{d}_i^T \underline{\underline{U}}^{-1} \underline{d}_i\right]}, \tag{3-39}$$

where

$$\underline{q} = \frac{\partial \underline{p}}{\partial \beta_i}. \tag{3-40}$$

The calculation of the sensitivities of $\underline{p}$ to ß, $\partial \underline{p} / \partial \beta$ is presented in the next section.

SENSITIVITIES OF PRESSURES TO STEP LENGTH

The sensitivity of pressures to step length $(\partial \underline{p} / \partial \beta)$ can be obtained by direct differentiation of the steady and transient state pressure equations. The pressures may relate to steady state, transient state, or a sequence of steady state and transient states. The calculation of the sensitivities for all these cases is given below.

Steady State

The steady-state simulation of pressure is represented by:

$$\underline{\underline{A}} \bullet \underline{p}_o = \underline{R}_o \ , \tag{3-41}$$

where, $\underline{\underline{A}}$ is the conductance matrix, $\underline{p}_o$ is the steady-state pressure, and $\underline{R}_o$ is the load vector. (The subscript o indicates a steady-state quantity.)

Differentiating with reference to β (iteration suffix is dropped for ß),

$$\underline{\underline{A}} \frac{\partial \underline{p}_o}{\partial \beta} + \frac{\partial \underline{\underline{A}}}{\partial \beta} \bullet \underline{p}_o = \frac{\partial \underline{R}_o}{\partial \beta} \tag{3-42}$$

$$\underline{\underline{A}} \frac{\partial \underline{p}_o}{\partial \beta} = \left[-\frac{\partial \underline{\underline{A}}}{\partial \beta} \bullet \underline{p}_o + \frac{\partial \underline{R}_o}{\partial \beta} \right]. \tag{3-43}$$

This equation is similar to the pressure equation (Equation 3.41). The coefficient matrix remains the same for both, while the load vector differs. The formulas for $\partial \underline{\underline{A}}/\partial\beta$ and $\partial \underline{\underline{R}}_o/\partial\beta$ will be developed below.

Suppose that there are N pilot points where the transmissivities $\underline{u}$ are being estimated by optimization. Consider one particular pilot point p:

$$\left(Y_p\right)_{i+1} = \left(Y_p\right)_i + \beta\left(d_p\right)_i$$

$$\frac{\partial\left(Y_p\right)_{i+1}}{\partial\beta} = \left(d_p\right)_i,$$

where d_p and Y_p are the pth elements in the vectors $\underline{d}$ and $\underline{Y}$ respectively, and i is the iteration level; $Y_p = \log_{10} T_p$, where T_p is the transmissivity assigned to pilot point p.

$$\frac{\partial \underline{\underline{A}}}{\partial\beta} = \frac{\partial \underline{\underline{A}}}{\partial Y_p} \bullet \frac{\partial Y_p}{\partial\beta} = \frac{\partial \underline{\underline{A}}}{\partial Y_p} \bullet d_p \tag{3-44}$$

$$\frac{\partial \underline{\underline{A}}}{\partial Y_p} = \ln(10) \sum_{m=1}^{M} \frac{\partial \underline{\underline{A}}}{\partial K_m} \bullet K_m \bullet \bar{\gamma}_{m,p} \quad . \tag{3-45}$$

From RamaRao and Reeves, (1990, Eq. 58, p. 26),

$$\frac{\partial \underline{\underline{A}}}{\partial\beta} = \ln(10) \sum_{m=1}^{M} \frac{\partial \underline{\underline{A}}}{\partial K_m} \bullet K_m \bullet \bar{\gamma}_{m,p} \bullet d_p . \tag{3-46}$$

Considering *all* the pilot points,

$$\frac{\partial \underline{\underline{A}}}{\partial\beta} = \ln(10) \sum_{p=1}^{N} \sum_{m=1}^{M} \frac{\partial \underline{\underline{A}}}{\partial K_m} \bullet K_m \bullet \bar{\gamma}_{m,p} \bullet d_p . \tag{3-47}$$

Similarly,

$$\frac{\partial \underline{R}_o}{\partial\beta} = \ln(10) \sum_{p=1}^{N} \sum_{m=1}^{M} \frac{\partial \underline{R}_o}{\partial K_m} \bullet K_m \bullet \bar{\gamma}_{m,p} \bullet d_p \ , \tag{3-48}$$

where K_m is the permeability in grid block m, $\bar{\gamma}_{m,p}$ is the average kriging weight at grid block m due to pilot point p, M is the number of grid blocks, and N is the number of pilot points.

Transient State

The pressures in transient state are obtained from

$$\left(\underline{\underline{A}}+\frac{\underline{\underline{S}}}{\Delta t}\right)\underline{p}^{k+1}=\left(\frac{\underline{\underline{S}}}{\Delta t}\right)\underline{p}^{k}+\underline{R}^{k}\ , \tag{3-49}$$

where k is the time level index, $\underline{\underline{A}}$ is the conductance matrix, $\underline{\underline{S}}$ is the storativity matrix, Δt is the time step $t^{k+1}-t^{k}$, and $\underline{R}^{k}$ is a part of the load vector, accounting for prescribed flow/pressure boundary condition.

This equation can be formulated in terms of $\delta\underline{p}=\left[\left(\underline{p}^{k+1}-\underline{p}^{k}\right)\right]$. This is accomplished by subtracting, $\underline{\underline{A}}p^{k}$ from both sides of Equation 3-49:

$$\left(\underline{\underline{A}}+\frac{\underline{\underline{S}}}{\Delta t}\right)\delta\underline{p}\ =\ -\underline{\underline{A}}p^{k}+\underline{R}^{k}\ , \tag{3-50}$$

where

$$\delta\underline{p}=\left(\underline{p}^{k+1}-\underline{p}^{k}\right). \tag{3-51}$$

Now, differentiating with reference to β,

$$\left(\underline{\underline{A}}+\frac{\underline{\underline{S}}}{\Delta t}\right)\frac{\partial(\delta\underline{p})}{\partial\beta}+\frac{\partial}{\partial\beta}\left(\underline{\underline{A}}+\frac{\underline{\underline{S}}}{\Delta t}\right)\delta\underline{p}\ =\ \frac{\partial\underline{R}^{k}}{\partial\beta}-\frac{\partial\underline{\underline{A}}}{\partial\beta}\bullet\underline{p}^{k}-\underline{\underline{A}}\frac{\partial\underline{p}^{k}}{\partial\beta}. \tag{3-52}$$

Noting that pilot points do not affect the storativity ($\partial\underline{\underline{S}}/\partial\beta\equiv 0$),

$$\left(\underline{\underline{A}}+\frac{\underline{\underline{S}}}{\Delta t}\right)\frac{\partial(\delta\underline{p})}{\partial\beta}\ =\ -\frac{\partial\underline{\underline{A}}}{\partial\beta}\bullet\underline{p}^{k+1}+\frac{\partial\underline{R}^{k}}{\partial\beta}-\frac{\underline{\underline{A}}\partial\underline{p}^{k}}{\partial\beta} \tag{3-53}$$

$$\frac{\partial\underline{p}^{k+1}}{\partial\beta}\ =\ \frac{\partial\underline{p}^{k}}{\partial\beta}+\frac{\partial(\delta\underline{p})}{\partial\beta} \tag{3-54}$$

Once again, these sensitivity equations are very similar to the pressure equations, with the coefficient matrix remaining the same, but with a different load vector.

The expressions for $\partial\underline{\underline{A}}/\partial\beta$ and $\partial\underline{R}^{k}/\partial\beta$ are similar to those already given for steady state and are not given separately, except to state that the time index must be carefully noted. Note that if the simulation involves steady state, $\partial\underline{p}_{0}/\partial\beta$ is evaluated first and then propagated to the transient state, just as pressure would be propagated. If the problem involves only transient state, $\underline{p}_{0}$ is the given initial condition. Then $\partial\underline{p}_{0}/\partial\beta\equiv 0$ is the initial condition for $\partial\underline{p}/\partial\beta$.

3.4.5 Pilot-Point Transmissivities: Constraints

It is possible that the optimization algorithms may dictate large changes in the transmissivities assigned to pilot points and bring about an impressive reduction in the objective function. Such recommended large changes may be viewed as undesirable for several reasons. At any point in the field, one can obtain a kriged estimate of transmissivity and its variance (kriging variance). One may construct a confidence interval (assuming a normal distribution of kriging errors) for the transmissivity. It is reasonable to expect the calibrated value to be within the confidence band. A constraint may be imposed to achieve this.

There also may be situations where the confidence band is large. A large change in a pilot-point transmissivity value, even if contained within the confidence band, can cause a large change in the spatial correlation structure of the transmissivity field. One objective in calibration can then be to limit the maximum change to a specified value so that the geostatistical structure of the transmissivity field is not altered significantly.

Consider the kth parameter, whose value is Y_k (kth element in the vector of parameters, $\underline{Y}$). Then,

$$\begin{aligned} \Delta Y_{k,i} &= \left(Y_{k,i+1} - Y_{k,i}\right) \\ &= \beta_i \bullet d_{k,i} \quad , \end{aligned} \tag{3-55}$$

where i is an iteration index.

Constraint 1: The parameter value should lie within the confidence band.

$$Y_{k,\mathrm{o}} - m\sigma_{y\mathrm{o}} \le Y_{ki+1} \le Y_{k,\mathrm{o}} + m\sigma_{y\mathrm{o}}, \tag{3-56}$$

where the subscript o indicates initially kriged value, based on the measured data only. Thus $Y_{k,\mathrm{o}}$ gives the initially kriged value at the location of k (the pilot point), $\sigma^2_{y\mathrm{o}}$ gives the initially computed kriging variance at the same location, and m is the multiplier of the standard deviation, which gives the semi width of the confidence band. If a normal distribution is assumed for kriging errors, and if 95% confidence levels are desired, then $m = 2$.

Constraint 2: The change in any parameters must be limited to $\Delta Y_{\max}$.

$$\Delta Y_{k,i} \le \Delta Y_{\max} \tag{3-57}$$

After the optimization, these constraints are implemented for each parameter. The selection of the constraints is input to GRASP-INV by the modeler. If a constraint becomes active (imposed), the optimal step length computed is reduced; however, the direction is preserved.

3.4.6 Convergence Criteria

DISTINCTION BETWEEN INNER AND OUTER ITERATIONS

There are two levels of iteration, designated as inner and outer iterations. An inner iteration relates to the iterations needed to optimize the transmissivities of the pilot points. Thus when an inner iteration is repeated, the pilot-point locations are fixed as at the beginning of the sequence of inner iterations. When the convergence of an inner iteration is achieved, the pilot points are added to the transmissivity data set. This then sets the stage for an outer iteration. During the course of outer iteration, optimal location of the next set of pilot points is done using coupled kriging and adjoint sensitivity analysis. Subsequently, their transmissivities are optimized by a sequence of inner iterations. Figure 3-6 clarifies these points. It may be noted that both inner and outer iterations go through all phases of the algorithm, except that inner iterations skip the phase of selecting pilot points from a grid of candidate pilot points.

CONVERGENCE CRITERIA: INNER ITERATIONS

The following criteria may be used to define convergence when optimizing the transmissivities assigned to a set of pilot points.

1. The performance measure (J) drops below a prescribed minimum value (JMIN):

$$J \leq \text{JMIN} . \tag{3-58}$$

2. The number of iterations (NITER) equals a prescribed maximum number of iterations, for the inner iterations (ITERMX1):

$$\text{NITER} \geq \text{ITERMX1} . \tag{3-59}$$

3. The ratio of the norm of the gradient to the initial gradient norm reduces below a prescribed value (GRNR):

$$\frac{\|\underline{g}\|}{\|\underline{g}_0\|} \leq \underset{\text{(gradient norm ratio)}}{\text{GRNR}} . \tag{3-60}$$

4. The gradient norm $\|\underline{g}\|$ is less than a prescribed minimum (GRMIN):

$$\|\underline{g}\| \leq \text{GRMIN} . \tag{3-61}$$

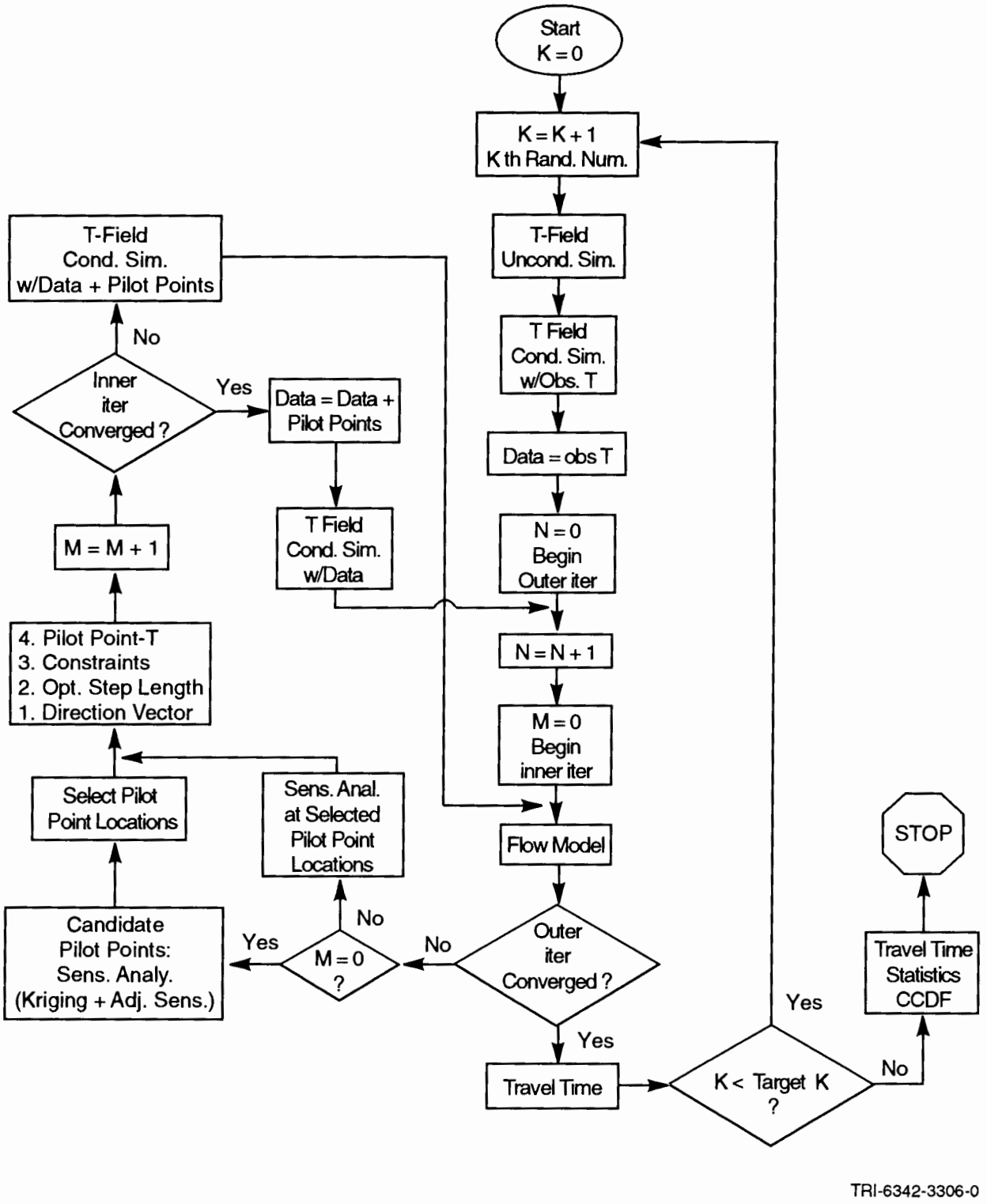

Figure 3-6. Inner and outer iterations of calibration.

5. The relative change in objective function is defined, as $\Delta J/J$, where ΔJ is the change in the objective function during one iteration. Iterations are terminated if this relative change falls below a prescribed value (RELCJ):

$$\frac{\Delta J}{J} \leq \text{RELCJ} \tag{3-62}$$

CONVERGENCE CRITERIA: OUTER ITERATIONS

Outer iterations are terminated essentially on criteria (1) and (2) of inner iterations. They are not repeated.

3.4.7 Computational Experience

Before applying the GRASP-INV code to the Culebra Dolomite flow model, several initial runs were conducted to gain experience regarding the sensitivity of the calibration to the number of pilot points added during each outer iteration. The results of this exercise indicated that adding a large number of pilot points during each outer iteration did not decrease the time necessary to achieve calibration relative to the time needed when only one or two pilot points were added. The times are similar because a plateau or region of high sensitivities of an objective function to changes in model transmissivities usually exists. The pilot points that are added are placed in this region at locations that generally have very similar sensitivity values. The optimization routine assigns a ΔY change if one pilot point is added, a $\Delta Y/2$ change at the pilot-point locations if two are added, and a $\Delta Y/3$ change if three pilot points are added. Thus, the modifications to the transmissivity field are essentially the same. Therefore, only one pilot point was added during each outer iteration while performing steady-state calibration in this study. Two pilot points were added to each outer iteration during transient calibration.

3.4.8 Earlier Inverse Algorithms: Similarities and Differences

The inverse algorithm used in GRASP-INV shares some similarities with earlier inverse algorithms (Marsily, de, et al., 1984; Carrera and Neuman, 1986) and maintains essential and substantial differences with them. It is useful to appreciate both the similarities and differences. In the present algorithm, if we suspend the automatic pilot-point selection process in the code, and if instead we proceed from given pilot-point locations, the algorithm would be very similar to that of Marsily, de, et al. (1984). Considering this problem as one of optimizing the magnitudes of parameters (pilot-point transmissivities) at the given locations, the algorithm is similar to that of Carrera and Neuman (1986).

The essential difference, however, is that the choice of (location of) parameters, subjectively done in the above-cited references, is rendered totally objective here, thus eliminating the need to consider alternative choices of zonation in Carrera and Neuman (1986) and the alternative choice of the pilot-point configuration in Marsily, de, et al. (1984). This objectivity is a desirable additional feature, raising the algorithm to a new level of sophistication.

Another distinguishing feature of the present algorithm is the multi-stage-approach used for the location of pilot points. For example, if the final calibration includes 30 pilot points, only one or two pilot points are identified in stage 1. Then starting from the CS transmissivity field, resulting from the inclusion of the pilot points determined in stage 1, another set of pilot points is obtained in stage 2. This process is repeated for several stages till satisfactory calibration is secured. One should notice the similarity of this approach to the well-known multi-stage optimization procedure, the dynamic programming method (Bellman, 1957). The present procedure of sequential-optimization stands in contrast to the earlier approaches that adopt a single-stage approach. They select all the parameters subjectively in one sequence and optimize their magnitudes. The present approach may be expected to provide a calibrated transmissivity field, generated from an optimal choice of calibration parameters. To achieve this optimality in the earlier algorithms, one must repeat the calibration exercise by considering several alternative choices of parameters (i.e., zonation patterns, pilot-point configurations).

Another important feature of the GRASP-INV code is the strategy and philosophy used in the inverse algorithm. Here, optimization of transmissivities is not carried on to the full extent mathematically. As an example, in the first outer iteration one or two pilot points are selected, and only one or two inner iterations are used to obtain the optimal transmissivity. The transmissivity changes at the pilot points are limited by user choice, such that the resulting field is not too different from the initial field, yet still giving substantial reductions in the objective function. Reductions in the objective function have become possible because the pilot point is placed at the most sensitive location, such that small changes in transmissivity can yield reasonable reductions in the objective function. When the parameters are subjectively selected, they are in most cases not optimal and require large changes in parameters to minimize the objective function. The resulting field may exhibit a different spatial structure. We believe that the objective selection of parameters, in a sequence, constitutes a particularly important highlight of the GRASP-INV code. Further, conceptually and mathematically, the sequential selection of parameters introduces an elegance in the methodology.

Because addressing the issues of spatial variability is the main focus of the present study, the zonation approach may not be adequate since it treats transmissivities in a zone as constant. In the pilot-point methodology, the modifications to the transmissivities in different grid blocks are determined by kriging and are not constant as in the zonation approach. In view of this, the pilot-point approach to calibration can be expected to mimic spatial variability more adequately than the zonation approach.

3.5 Code Development and Organization

A comprehensive code package has been assembled using many of the codes already developed and frequently used in groundwater flow simulations; they are listed below. For details of the theory and application of these codes, the references cited may be consulted.

- TUBA, unconditional simulation of transmissivity field (Zimmerman and Wilson, 1990)
- AKRIP, kriging with generalized covariances (Kafritsas and Bras, 1981)
- SWIFT II, modeling pressures (steady and transient state) (Reeves et al., 1986a,b,c)

- GRASP II, adjoint sensitivity analysis (steady and transient state) (Wilson et al., 1986; RamaRao and Reeves, 1990)

- STLINE, groundwater travel time and travel paths (INTERA, Inc., 1989)

In addition to using the above codes, the following new codes have been developed in the present task. The details of the new codes will be given later.

- MAIN—drives the different modules

- CONSIM—generates conditional simulations of transmissivity from the unconditional simulations of transmissivity

- PILOTL—locates the pilot points based on sensitivity analysis

- PAREST—assigns the pilot-point transmissivities by minimization of a least square objective function.

Figure 3-7 gives the code organization. Table 3-1 gives the important subroutines and their functions.

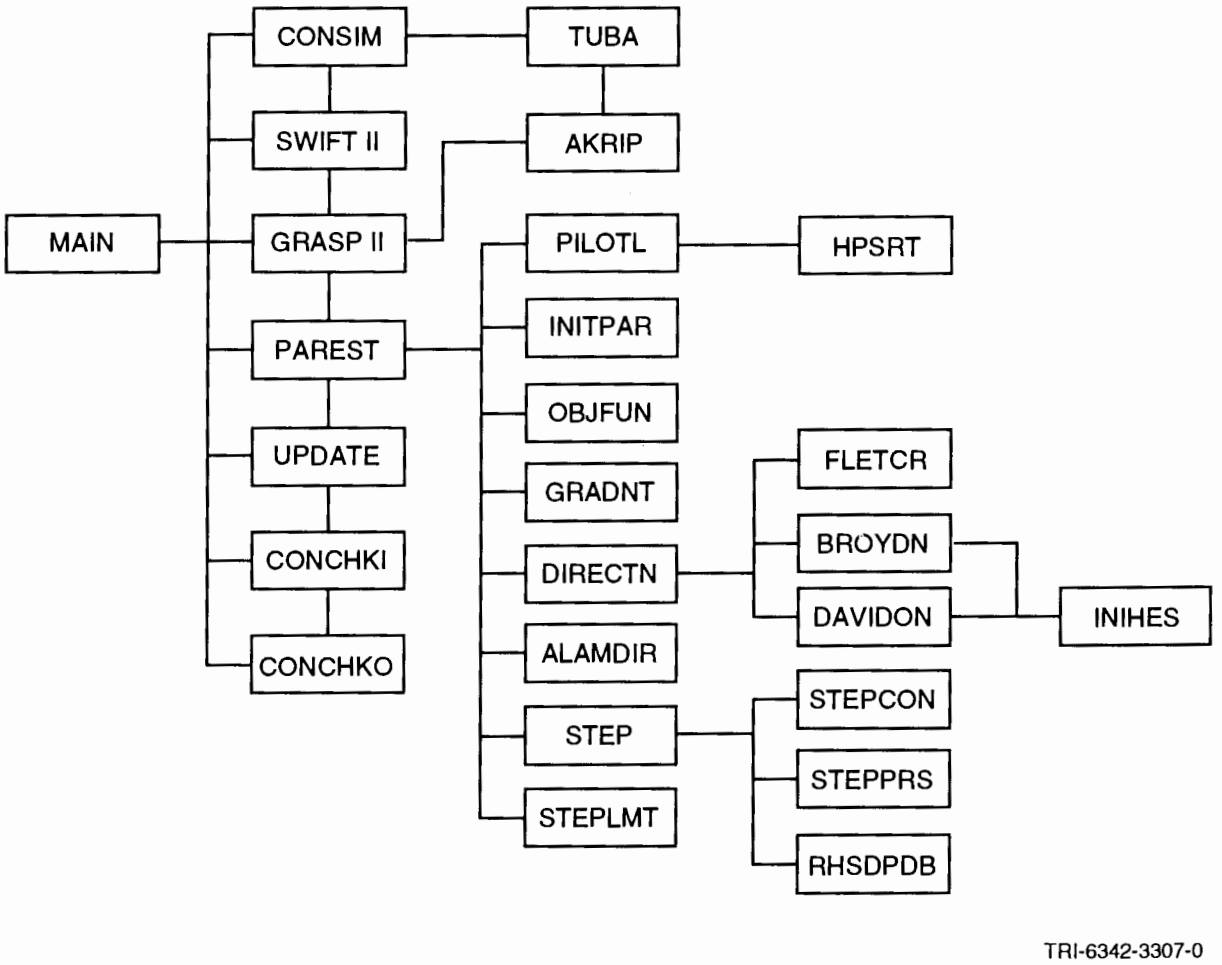

Figure 3-7. GRASP-INV code organization.

Table 3-1. Subroutines and Their Functions

Name of Subroutine	Purpose
MAIN	Driver program for this code package.
SWIFT II	Simulation of pressures.
GRASP II	Sensitivity derivatives of performance measure with reference to model parameters.
TUBA	Unconditional simulation of transmissivities.
CONSIM	Conditional simulation of transmissivities.
AKRIP	Kriging with general covariance functions.
PAREST	Evaluates pilot-point transmissivities by optimization.
PILOTL	Selects the pilot-point locations based on sensitivity analysis.
INITPAR	Initializes pilot-point transmissivities and their covariance matrix for the first iteration in calibration.
READ3	Reads input related to pilot-point transmissivity optimization.
OBJFUN	Compute weighted least squares objective function
GRADNT	Computes gradients of objective function to pilot-point transmissivities.
DIRECTN	Computes directions in search algorithm.
STEP	Computes step length in search algorithm.
UPDATE	Updates the pilot-point transmissivities at the end of an iteration.
HPSRT	Sorts absolute gradients in descending order.
BROYDN	Computes direction per Broyden algorithm.
FLETCR	Computes direction per Fletcher-Reeves (conjugate gradients) algorithm.

Table 3-1. Subroutines and Their Functions (Concluded)

Name of Subroutine	Purpose
INIHES	Computes initial approximate inverse Hessian matrix.
STEPCON	Computes transmissivities-dependent constant in step-length formula.
STEPPRS	Computes pressure-dependent expressions in step-length formula.
ALAMDIR	Computes expressions involving Kriging weights and directions (to be used for solving sensitivity of pressure to step-length).
RHSDPDB	Computes right-hand column vector for solving the equation for sensitivity of pressure to step-length.
STEPLMT	Implements constraints on step length after optimization.
CONVCKI	Checks convergence of inner iterations.
CONVCKO	Checks convergence of outer iterations.

4. APPLICATION

4.1 Application to 1990 Model Grid

In an attempt to determine the effect the subjectivity inherent in the manual calibration had upon the results determined in the 1990 study, the GRASP-INV code was used to produce a kriged transmissivity field calibrated to the Culebra steady-state and transient pressure data. The entire model area was initially calibrated to the steady-state data using the GRASP-INV code. During the calibration, a global objective function was employed that consisted of the differences between the calculated and observed pressures at each of the WIPP-site boreholes. The global objective function eliminated the subjectivity of regionalizing the calibration areas within the model. That is, the areas with the largest head differences were calibrated during each calibration step in contrast to the manual approach in which the upgradient and downgradient areas were calibrated first.

Once the global steady-state objective function was reduced to 3.0×10^9 Pa^2 (a selected calibration target that is equivalent to an average head difference of 1.0 m), the model was subsequently calibrated to the pressures from the transient events. Table 4-1 lists the events used during transient calibration. These are the same events simulated in the 1990 study. The calibration to the transient events was conducted chronologically because earlier tests impact the initial conditions of subsequent tests.

Figure 4-1 and Table 4-2 depict the GRASP-INV calibrated field (GICF) and the associated steady-state head differences. The features of the general trends in the transmissivities are very similar to the calibrated field from the 1990 study (LaVenue et al., 1990). A high-transmissivity region extends northward from P-17 to the H-15 borehole. In addition, the steady-state head differences are very similar to those determined in the 1990 study.

The transient heads calculated from the GICF are illustrated in Figures 4-2 (Well H-1, Hydropad H-6, and Well DOE-2) and 4-3 (Hydropad H-11, Well DOE-1, and Hydropad H-15). The transient heads agree reasonably well with the observed heads. The main differences occur at the H-1 borehole, where the calculated heads are lower than the observed, and the H-15 and DOE-1 boreholes, where the calculated responses to the H-11 pumping test could use some improvement.

Figure 4-4 is an enlargement of Figure 4-1 in the vicinity of the southern WIPP-site boundary. The northern extension of the high-transmissivity zone is clearly depicted. The magnitudes of the transmissivities within this region fall between -5.0 and -4.0 $\log_{10}$ (m^2/s), which is slightly lower than the magnitudes within the high-transmissivity zone of the 1990 study (-5.0 to -3.5). A lower transmissivity region (-7.0 to -6.0 $\log_{10}$ T [m^2/s]) extends across the central WIPP-site area, which causes the differences observed in the transient heads at the H-1 borehole. This lower transmissivity region was split into two distinct regions in the 1990 calibrated field (Figure 2-10): one section surrounded the P-15 and H-14 boreholes in the southwest region of the WIPP site area, and the other section extended northeastward from the WIPP-21 borehole in the central WIPP-site area.

The differences between the GRASP-INV and 1990 calibrated fields are illustrated in Figure 4-5. The GICF has significantly lower transmissivities in the shaded regions with the exception of the region south of the H-3 borehole,

Table 4-1. Events Used during Transient Calibration

Time Period	Well/Shaft	Event
08/07/81 - 12/06/81	C&SH	Construction*
12/06/81 - 10/01/83	C&SH	Lined and Grouted*
01/30/82 - 02/01/84	WHS	Construction*
10/24/82 - 10/14/84	H-4	Pumping for Tracer Test
10/05/83 - 01/10/84	EXS	Construction*
10/13/83 - 10/16/83	H-2	Pumping
11/08/83 - 11/17/83	H-2	Pumping
01/10/84 - 10/15/84	EXS	Enlarged dia. to 4.3 m*
02/01/84 - 04/05/84	WHS	Enlarged dia. to 6.5 m*
04/05/84 - 08/20/84	WHS	Lined and Grouted*
04/23/84 - 06/13/84	H-3	Pumping for Tracer Test
06/07/84 - 07/02/84	H-2	Bailing at H-2
07/17/84 - 08/02/84	H-2	Pumping
10/15/84 - 12/04/84	EXS	Liner on Culebra*
06/20/85 - 07/10/85	H-3	Pumping (Step Drawdown)*
10/15/85 - 12/16/85	H-3	Pumping (Multipad Test)*
04/04/86 - 04/21/86	H-2	Pumping
01/12/87 - 02/17/87	WIPP-13	Pumping (Multipad Test)*
06/01/87 - 06/01/89	C&SH	Grouted*
07/23/87 - 08/12/87	H-2	Pumping (Water Qual. Samp)
08/07/87 - 08/24/87	H-3	Pumping (Water Qual. Samp)
11/01/87 - 06/01/89	WHS	Grouted*
01/01/88 - 11/01/88	AIS	Construction*
05/05/88 - 07/07/88	H-11	Pumping (Multipad Test)*
11/01/88 - 06/01/89	AIS	Steel Liner Emplaced*
02/13/89 - 03/02/89	H-3	Pumping (Water Qual. Samp)
02/14/89 - 02/17/89	P-14	Pumping

*Considered a major event.

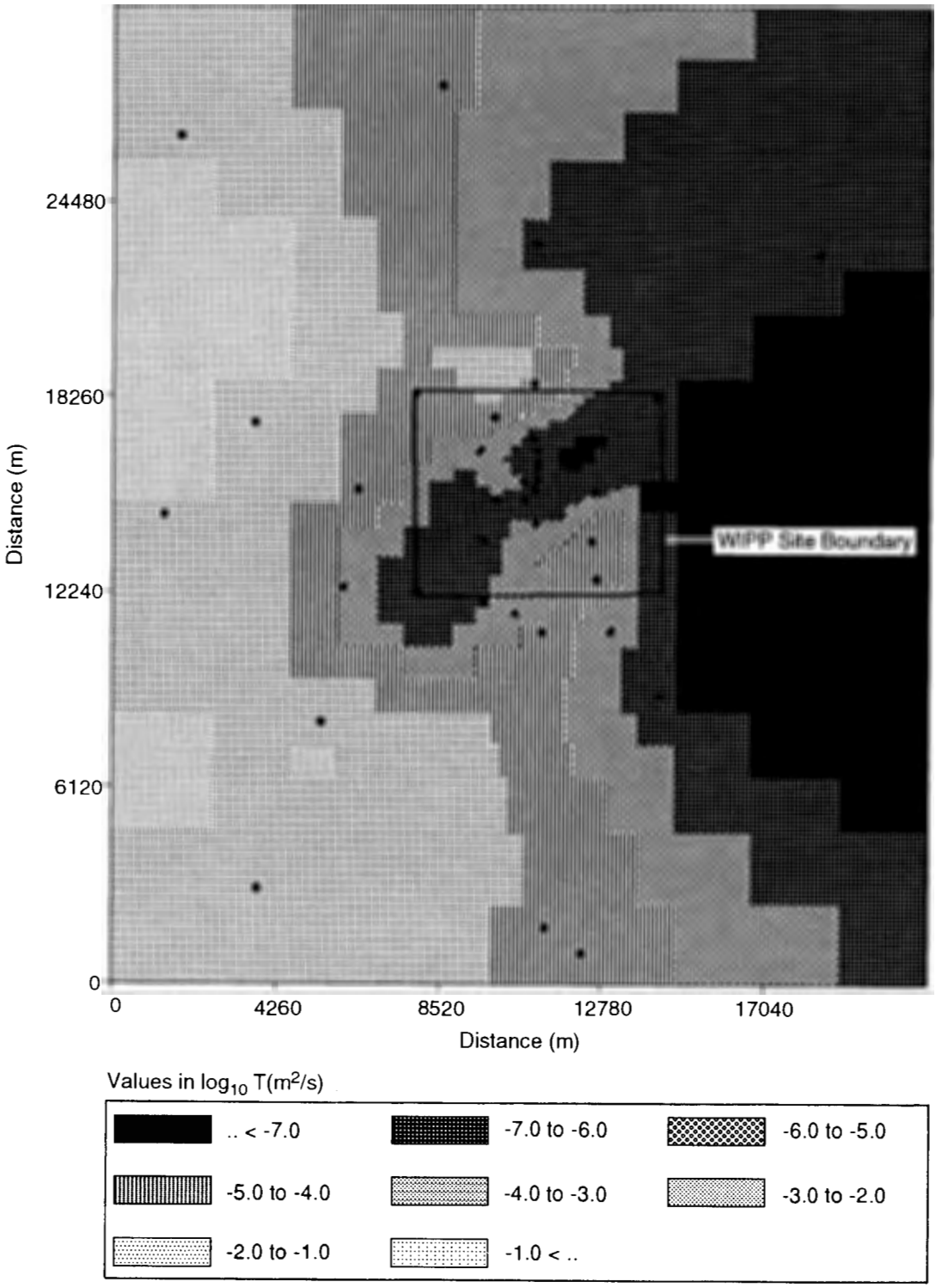

TRI-6342-3410-0

Figure 4-1. Transient calibrated kriged transmissivity field determined using GRASP-INV and the 1990 model grid. (Note: Aspect ratio of figure is not [1:1].)

Table 4-2. Difference Between Calculated and Observed Freshwater Heads for GRASP-INV Calibrated Field using the 1990 Model Grid

Well Location	Difference Between Calculated and Observed Freshwater Heads (m)
H-1	-0.88
H-2	1.50
H-3	-1.74
H-4	-1.08
H-5	-1.25
H-6	0.04
H-7	-2.02
H-9	0.60
H-10	-1.96
H-11	1.37
H-12	0.18
H-14	0.89
H-15	1.68
H-17	3.01
H-18	-0.31
P-14	0.23
P-15	-0.64
P-17	-0.14
WIPP-12	0.83
WIPP-13	-0.83
WIPP-18	0.54
WIPP-25	0.60
WIPP-26	-0.25
WIPP-27	0.47
WIPP-28	1.50
WIPP-30	-0.29
CB-1	-0.42
DOE-1	1.08
DOE-2	-0.60
D-268	1.52
USGS-1	0.02

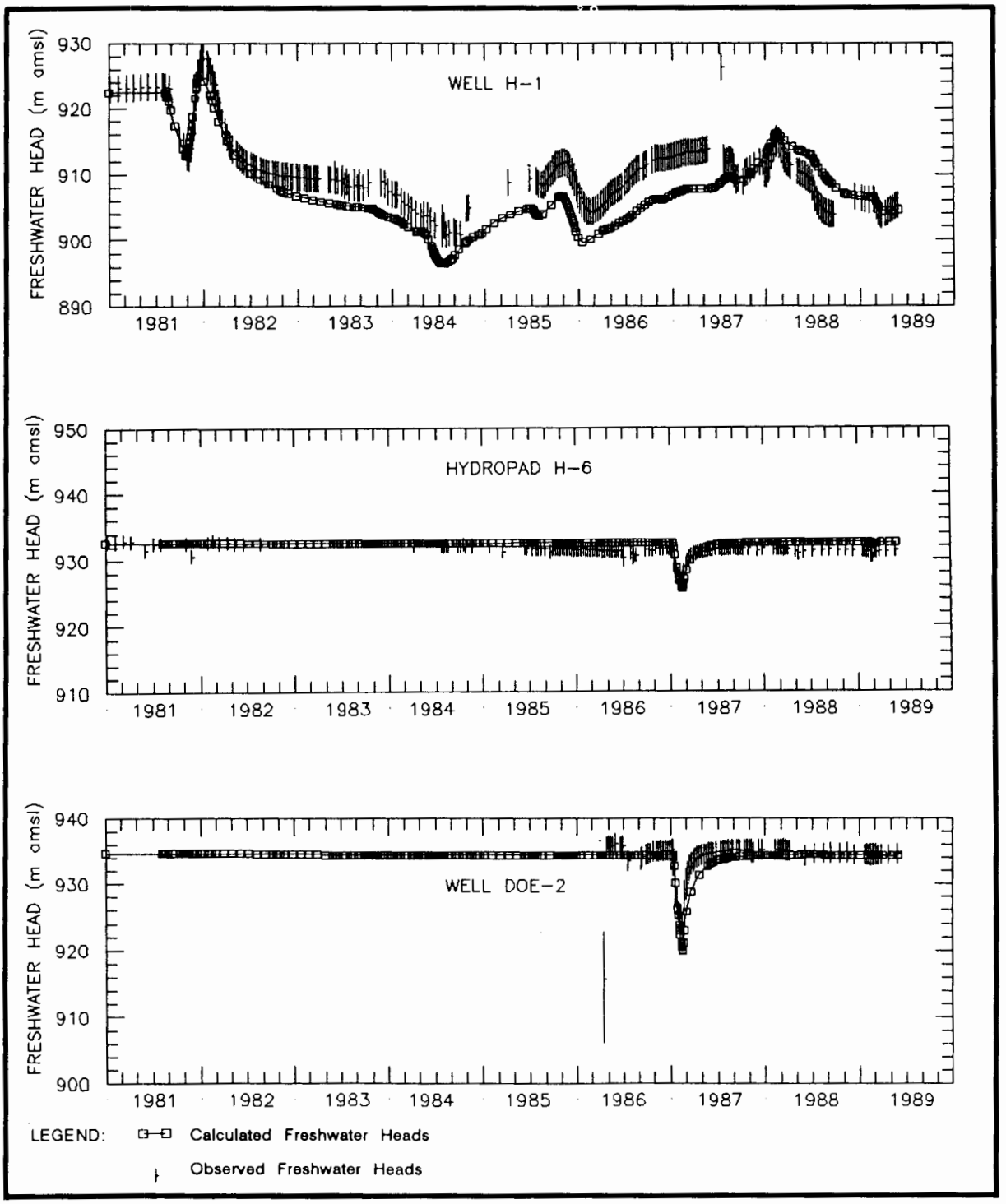

TRI-6342-3412-0

Figure 4-2. Transient heads calculated using the GRASP-INV transient calibrated model: Well H-1, Hydropad H-6, and Well DOE-2.

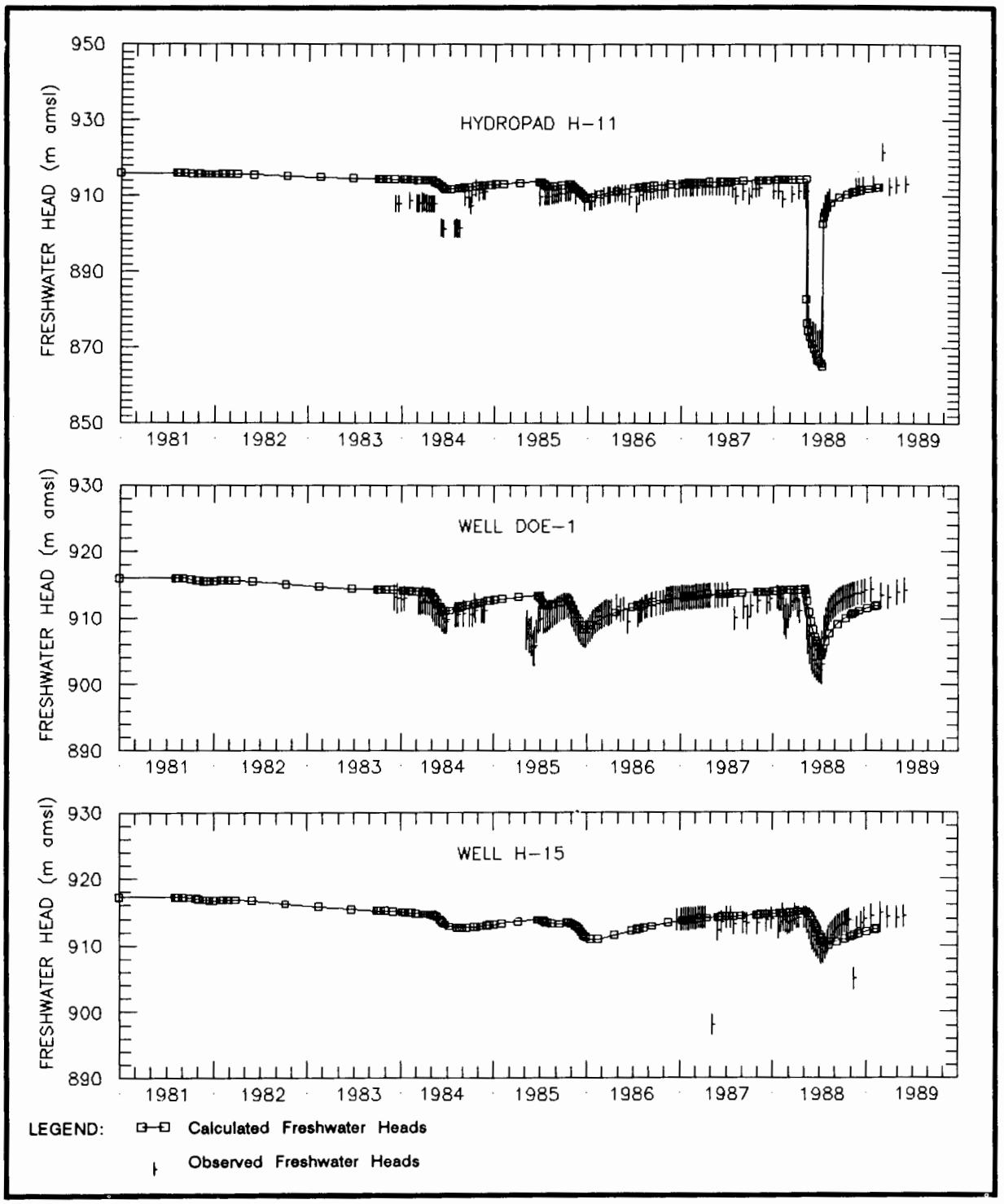

TRI-6342-3346-1

Figure 4-3. Transient heads calculated using the GRASP-INV transient calibrated model: Hydropad H-11, Well DOE-1, and Hydropad H-15.

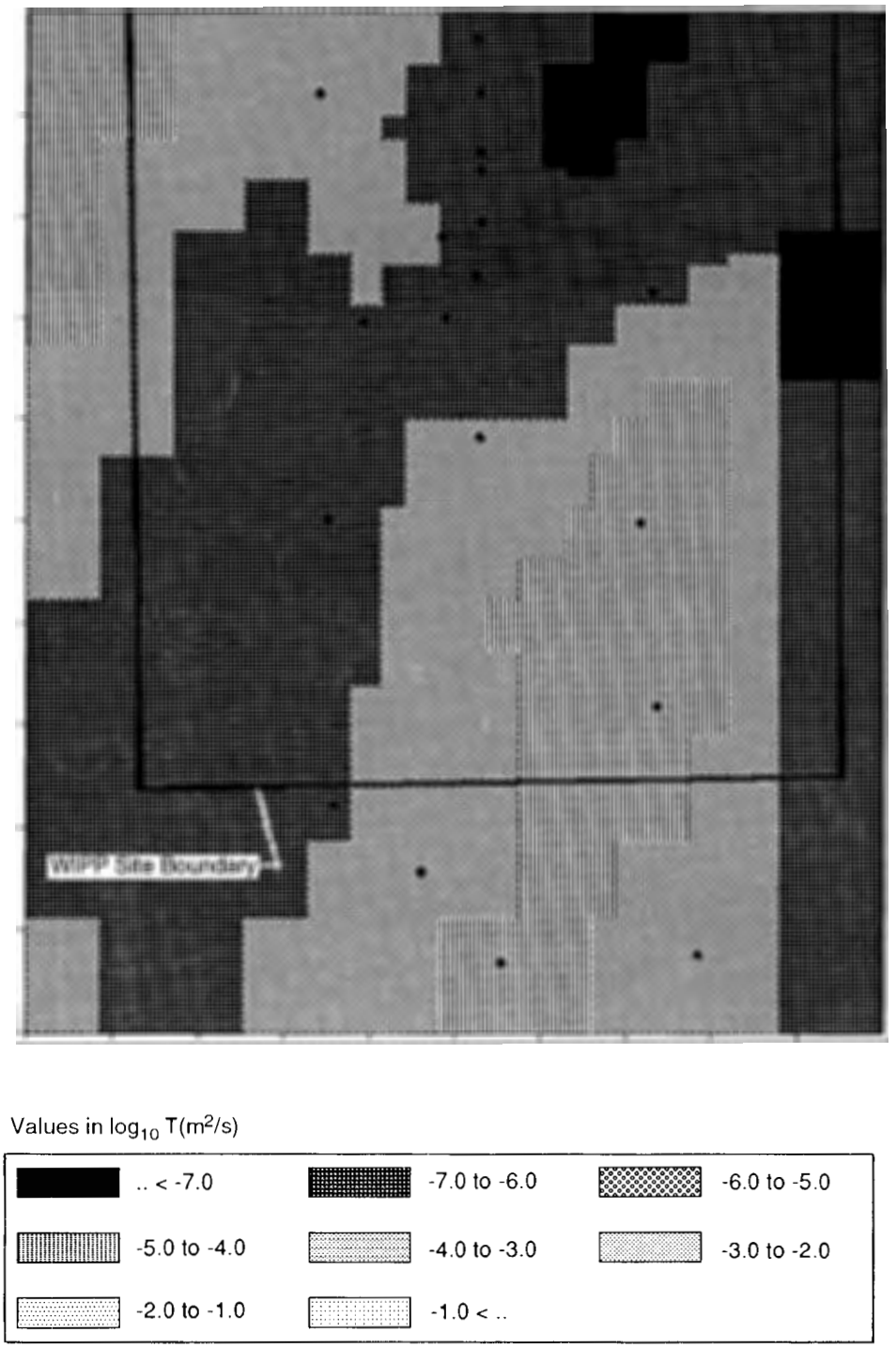

Figure 4-4. Enlargement of transmissivity field in the vicinity of the southern WIPP-site boundary. (Note: Aspect ratio of figure is not [1:1].)

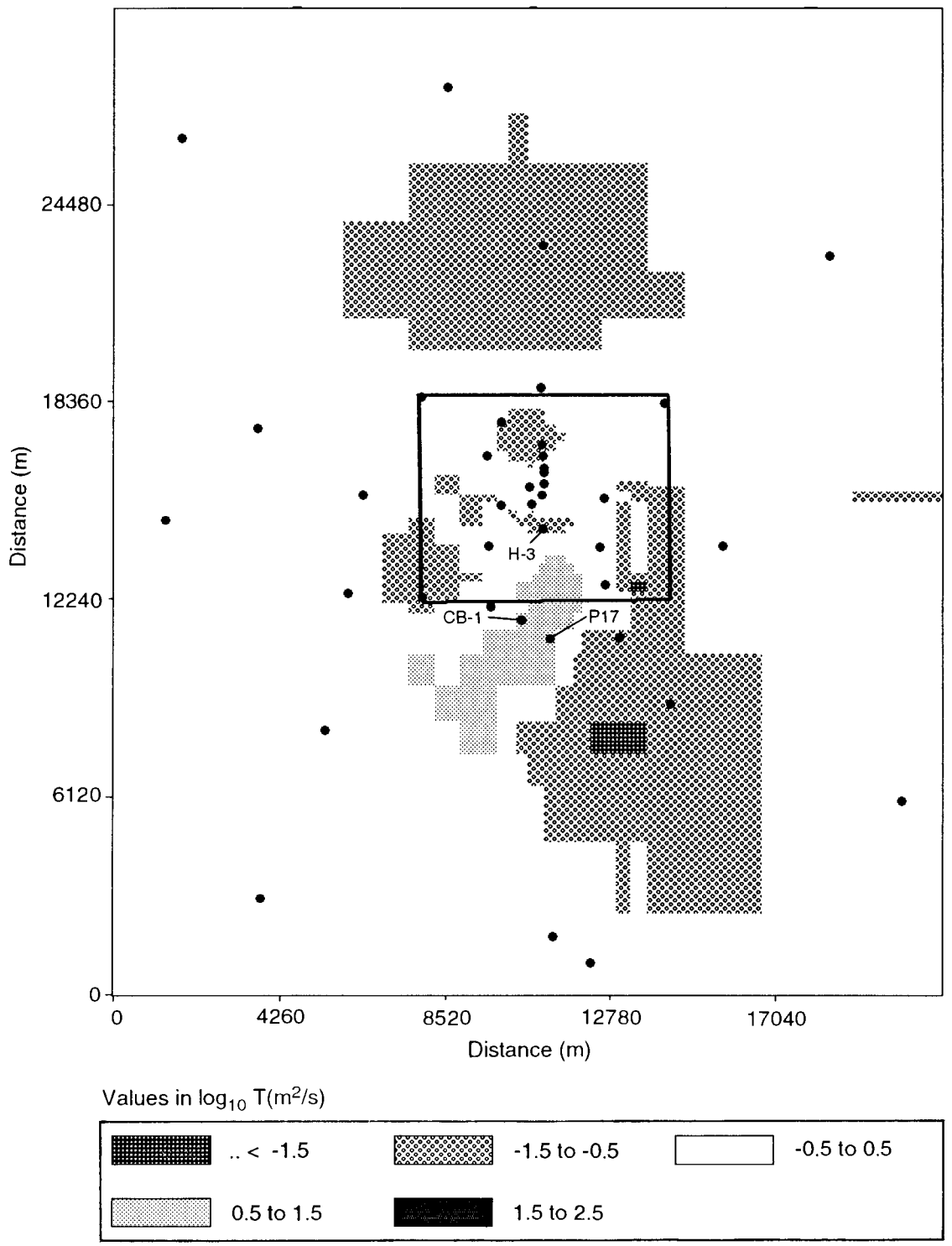

Figure 4-5. Differences between the GRASP-INV calibrated transmissivity field and the manually calibrated field of LaVenue et al., 1990. (Note: Aspect ratio of figure is not [1:1].)

adjacent to the CB-1 and P-17 boreholes. Here the GICF transmissivities are higher by about 0.5 to 1.5 $\log_{10}$ (m^2/s). The region immediately north of the H-3 borehole is -1.5 to -0.5 $\log_{10}$ (m^2/s) lower in the GICF field relative to the 1990 study.

Figure 4-6 contains the travel paths determined in the 1990 study and from the GICF. Both the travel paths and the travel times to the southern WIPP-site boundary for these two trajectories differ significantly. The travel time determined in the 1990 study was approximately 14,000 yr. The travel time associated with the GRASP-INV code is approximately 30,000 yr, a factor of 2 higher. The higher travel time may be largely attributed to the lower transmissivity region north of the H-3 borehole (i.e., in the particle drop point region). If the differences in the calculated and observed heads at the H-1 borehole were reduced (Figure 4-2), the transmissivities would be increased north of H-3, which would ultimately reduce the travel time of 30,000 yr. However, the automated calibration was restricted to adding only 44 pilot points, approximately the same as were added in the 1990 study. This was done to evaluate the robustness of the GRASP-INV code. The constraint imposed on the assignment of the pilot-point transmissivities was also more restrictive ($\pm 3\sigma$) than the manual assignment of transmissivity in the 1990 study. Therefore, the same number of pilot points does not adequately modify the transmissivity field to fully calibrate the model to the transient heads. If additional pilot points had been added to produce an equivalent "goodness-of-fit" to the 1990 study, the travel times would be closer.

4.2 Description of the 1992 Culebra Model

4.2.1 Model Grid and Boundary Conditions

The finite-difference grid used in this modeling study to generate 70 CS fields was selected to facilitate the successful reproduction of both steady-state and transient heads. The grid consists of $50 \times 57 \times 1$ (x,y,z) grid blocks and has a finer grid occurring in the central portion of the model in the vicinity of H-3, H-11, WIPP-13, and the shafts (Figure 4-7). Grid-block dimensions range from 50 m near the center of the site to approximately 2800 m at the model boundary. The vertical dimension of the grid is taken from the thickness of the Culebra Dolomite in the WIPP area. The mean thickness of 7.7 m was calculated from the available data and was assumed suitable for the vertical model dimension in this study.

The grid was rotated 38° east (Figure 4-8) relative to the 1990 model grid to facilitate the introduction of climatic variations during the 1992 PA calculations (Section 7.2.2 of WIPP PA Department, 1992, Vol. 2). The model boundaries and orientation are the same as used by Beyeler in the 1991 PA Culebra calculations. The locations of the boundaries of the model were chosen to maximize the ability to use Nash Draw as a groundwater divide and to minimize the effect that the boundaries may have on the transient modeling results for the long-term pumping tests at the H-3, WIPP-13, and H-11 locations. Table 4-3 lists the prescribed-pressure boundaries that were applied to the southeastern, southwestern, northeastern, and northwestern boundaries (Figure 4-8). One section of the northwestern boundary was considered a no-flow boundary due to the groundwater divide along Nash Draw.

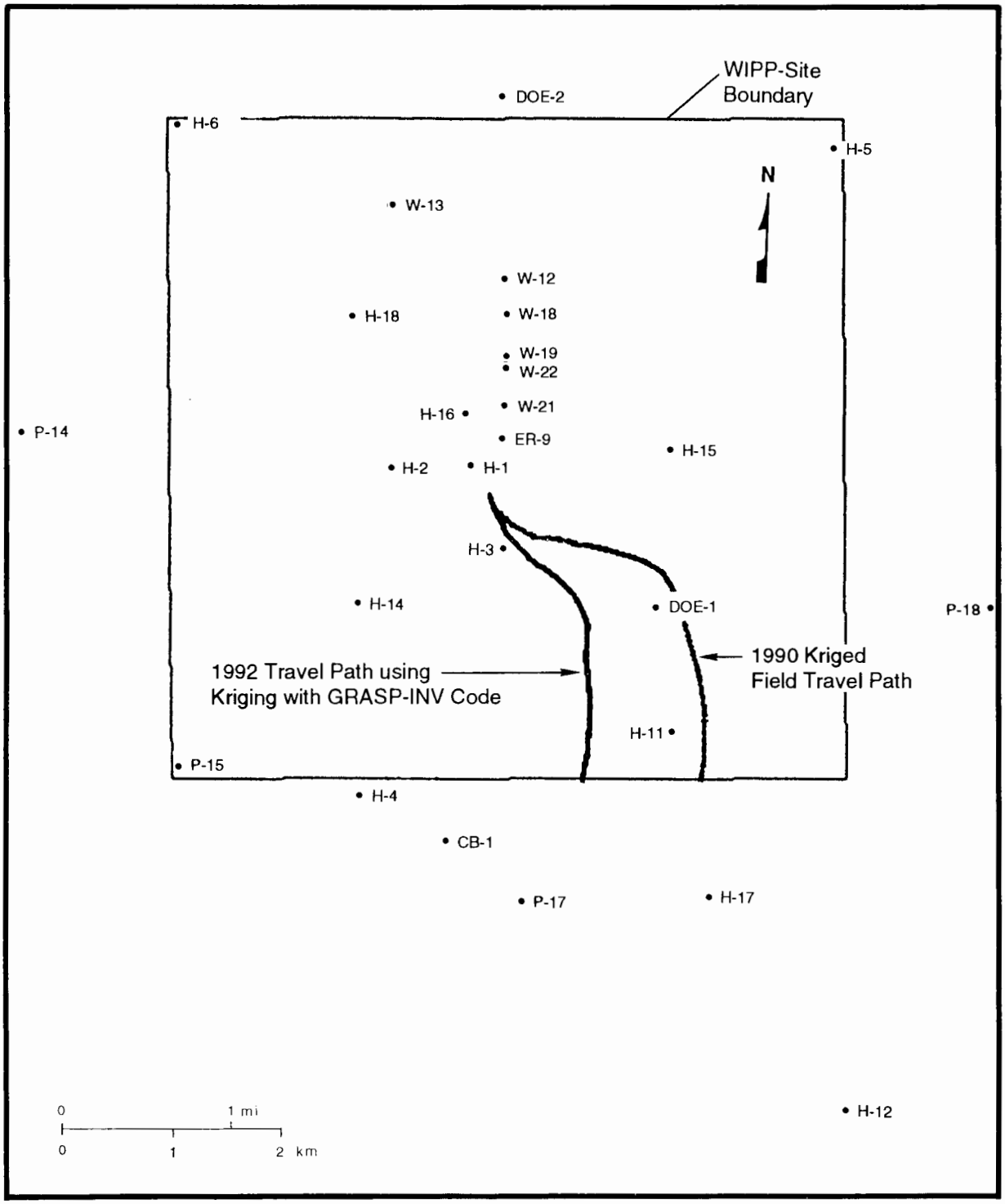

TRI-6342-3355-0

Figure 4-6. Particle travel paths from the 1990 and 1992 kriged transmissivity fields.

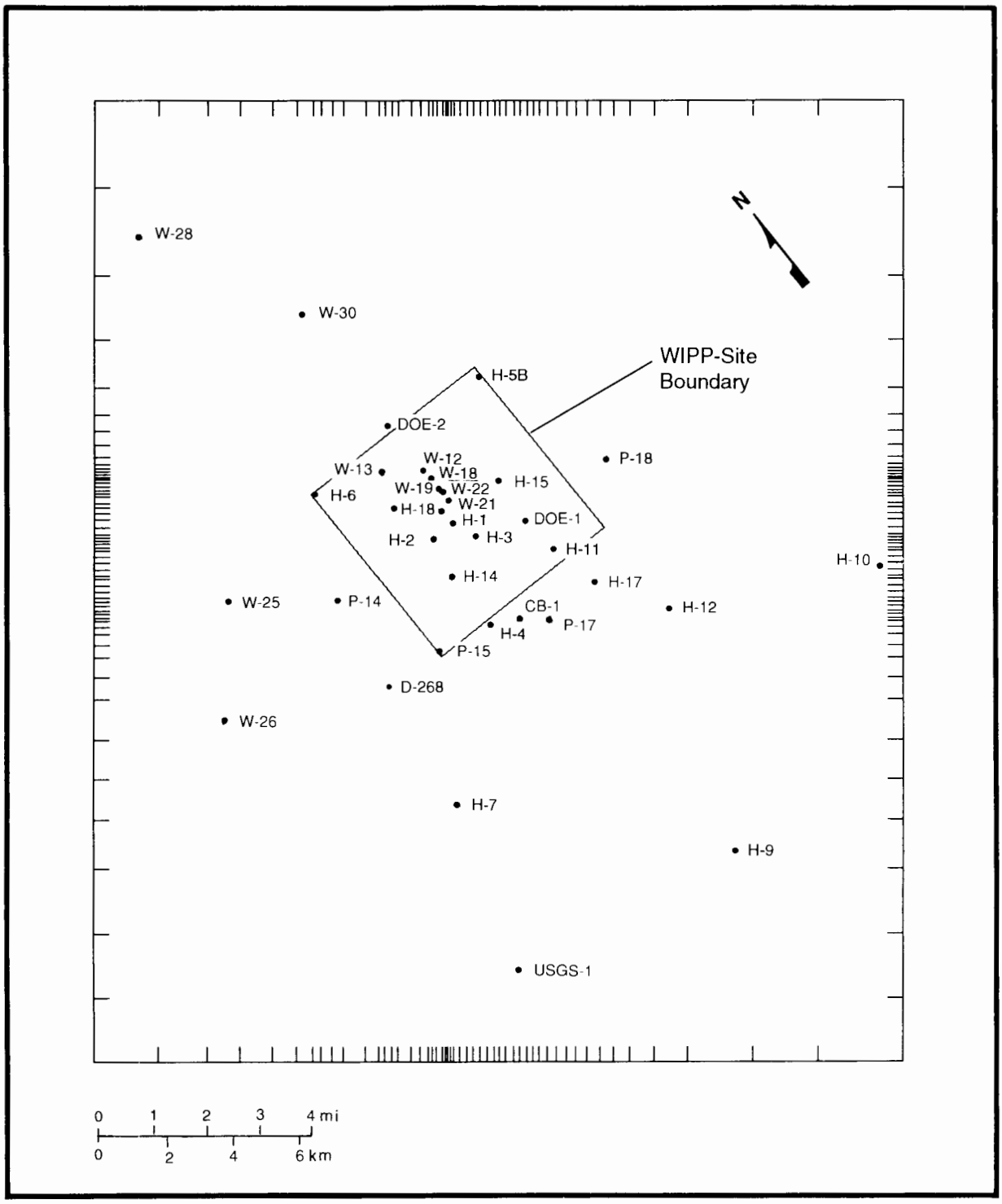

TRI-6342-3348-0

Figure 4-7. Finite-difference regional grid used in 1992 modeling study.

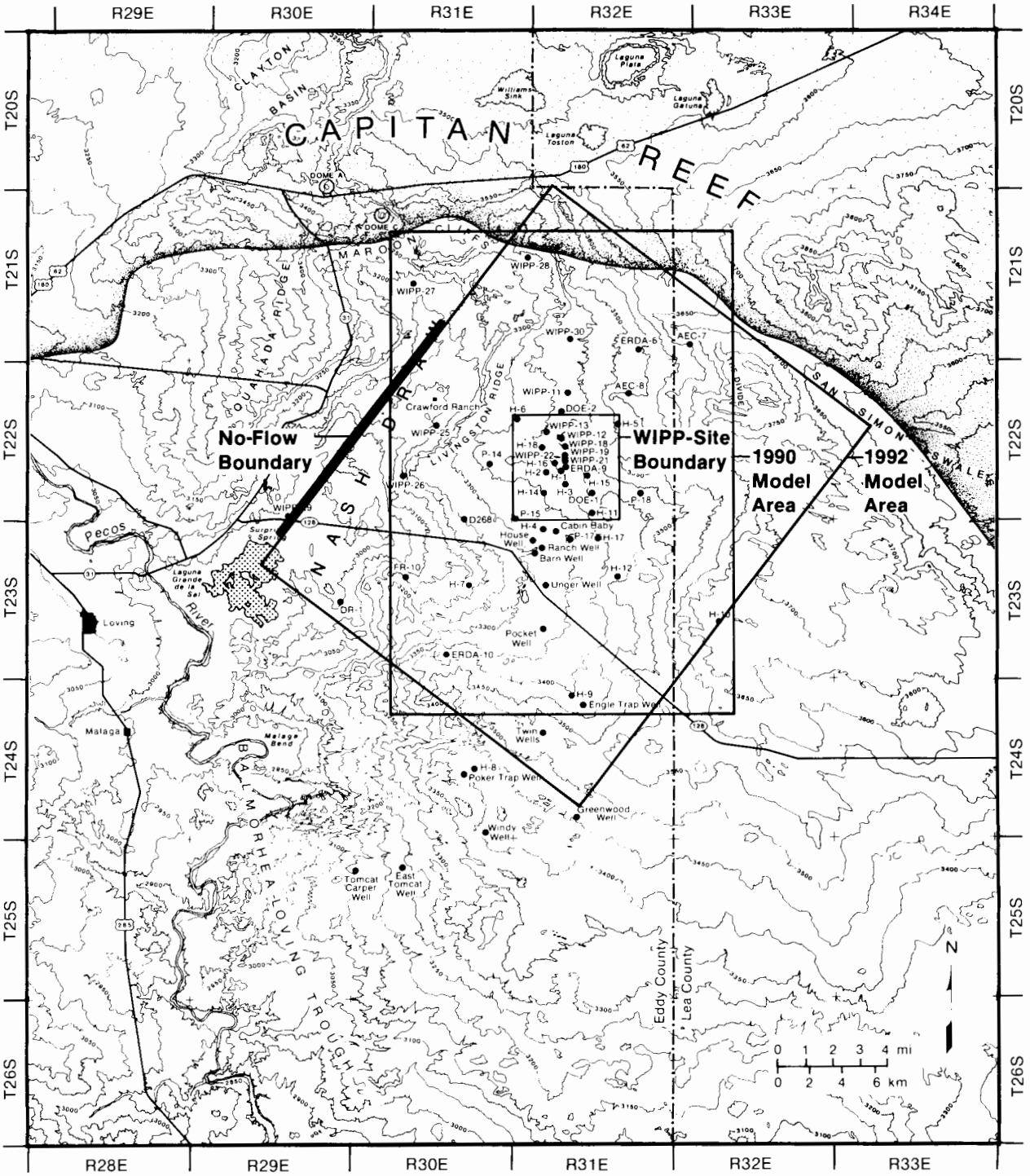

TRI-6342-612-10

Figure 4-8. Comparison of 1990 and 1992 model areas.

Table 4-3. Prescribed Pressure Boundaries.

Boundary	Model Indices (I,J)	Elevation of Head (m)
Northwestern	1,2	905.52
	1,50	937.53
	1,52	938.00
	1,54	938.47
	1,56	938.75
	1,49	937.29
	1,51	937.72
	1,53	938.26
	1,55	938.79
	1,57	941.02
Northeastern	2,57	942.01
	3,57	942.00
	4,57	941.86
	5,57	941.65
	6,57	941.47
	7,57	941.20
	8,57	940.95
	9,57	940.82
	10,57	940.59
	11,57	940.42
	12,57	940.19
	13,57	940.04
	14,57	939.83
	15,57	939.56
	16,57	939.42
	17,57	939.16
	18,57	938.95
	19,57	938.82
	20,57	938.65
	21,57	938.37
	22,57	938.20
	23,57	937.97
	24,57	937.85
	25,57	937.60
	26,57	937.42
	27,57	937.18
	28,57	937.00
	29,57	936.70
	30,57	936.51
	31,57	936.23
	32,57	936.00
	33,57	935.87
	34,57	935.83
	35,57	935.67
	36,57	935.64
	37,57	935.49
	38,57	935.34
	39,57	935.27
	40,57	935.23
	41,57	935.07
	42,57	934.94
	43,57	934.89
	44,57	934.79

Table 4-3. Prescribed Pressure Boundaries (Continued).

Boundary	Model Indices (I,J)	Elevation of Head (m)
(Northeastern)	45,57	934.57
	46,57	934.41
Southeastern	50,2	950.30
	50,3	938.01
	50,4	955.59
	50,5	980.20
	50,6	997.61
	50,7	1038.44
	50,8	1067.32
	50,9	985.20
	50,10	999.29
	50,11	1008.10
	50,12	1018.84
	50,13	1032.20
	50,14	1047.88
	50,15	1071.01
	50,16	1104.73
	50,17	982.63
	50,18	1007.38
	50,19	1016.58
	50,20	1034.33
	50,21	1032.22
	50,22	1053.31
	50,23	1082.89
	50,24	1108.83
	50,25	1001.00
	50,26	1015.55
	50,27	1025.21
	50,28	1043.19
	50,29	1057.01
	50,30	1069.37
	50,31	1080.87
	50,32	1108.27
	50,33	1013.46
	50,34	1011.01
	50,35	1017.05
	50,36	1032.92
	50,37	1046.08
	50,38	1067.07
	50,39	1074.44
	50,40	1106.30
	50,41	1037.52
	50,42	1007.12
	50,43	1011.56
	50,44	1022.06
	50,45	1034.68
	50,46	1049.14
	50,47	1053.92
	50,48	1081.50
	50,49	1044.60
	50,50	1005.70

Table 4-3. Prescribed Pressure Boundaries (Concluded).

Boundary	Model Indices (I,J)	Elevation of Head (m)
(Southeastern)	50,51	1008.32
	50,52	1010.70
	50,53	1006.69
	50,54	993.89
	50,55	970.08
	50,56	963.09
Southwestern	1,1	905.29
	2,1	904.37
	3,1	908.14
	4,1	908.83
	5,1	905.86
	6,1	902.74
	7,1	898.18
	8,1	892.09
	9,1	886.34
	10,1	879.84
	11,1	875.75
	12,1	875.45
	13,1	876.41
	14,1	878.27
	15,1	882.59
	16,1	888.41
	17,1	891.85
	18,1	893.42
	19,1	893.86
	20,1	893.99
	21,1	893.82
	22,1	893.52
	23,1	893.11
	24,1	892.44
	25,1	891.71
	26,1	890.76
	27,1	890.15
	28,1	890.32
	29,1	891.73
	30,1	893.96
	31,1	896.83
	32,1	900.19
	33,1	902.57
	34,1	904.10
	35,1	905.28
	36,1	905.14
	37,1	904.47
	38,1	904.54
	39,1	905.29
	40,1	904.86
	41,1	903.28
	42,1	902.78
	43,1	904.44
	44,1	907.84
	45,1	912.35
	46,1	917.67
	47,1	926.39
	48,1	941.73
	49,1	955.63
	50,1	965.73

The Culebra is considered confined above and below by low-permeability beds of anhydrite, halite, and siltstone. Vertical flux is not considered in the model because of the existence of these low-permeability anhydrites. The conceptual model used in this study therefore assumes a two-dimensional flow system although this assumption has not been validated. Currently, a three-dimensional modeling effort is being conducted by Sandia Department 6119 to determine the validity of assuming the Culebra is a completely confined aquifer.

4.2.2 Model Initial Kriged-Transmissivity Field and Its Uncertainty

As in the 1990 study, uncertainties were assigned to the observed transmissivity data. For example, in order to account for the difference in the uncertainty associated with transmissivities derived from DSTs and slug tests and those derived from pumping tests, standard deviations (σ) of the $\log_{10}$ transmissivity values were assumed and assigned values based on the type of test used to obtain the value. A minimum standard deviation $\sigma = 0.25$ for $\log_{10}$ T, T in m^2/s, was assumed for pumping-test results, and a standard deviation $\sigma = 0.5$ was considered to be appropriate for transmissivity values interpreted from the results of DSTs or slug tests. These assigned standard deviations are meant to represent the difference in uncertainties of the results of these tests on a scale of tens of meters.

Before a conditional simulation of the transmissivity field can be produced, the determination of a theoretical generalized covariance function (GCF) consistent with the logarithms of the Culebra transmissivity data must be performed. The GCF is the theoretical model which is used to estimate the transmissivities with kriging and to generate the unconditional transmissivity field for the conditional simulation. In the AKRIP code, the coefficients of the GCF are determined by an automatic iterative procedure in which the GCF is fitted to local neighborhoods defined by subsets of the observed transmissivity data. As in the 1990 study, the neighborhood used in this study is defined by the ten nearest observed data points surrounding a particular grid block in the model area.

LaVenue et al. (1990) determined that a zero-order GCF best fit the observed Culebra transmissivity data according to the following relation:

$$K(s) = -2.3 \times 10^{-4} |s| \ , \tag{4-1}$$

where $K(s)$ is the generalized covariance and s is the average distance between an observed data point and the center of the estimation area. More details concerning the selection of this GCF may be found in LaVenue et al. (1990).

The initial kriged grid-block $\log_{10}$-transmissivity estimates (i.e., the average over the specific area of each block as determined using a 2×2 Gauss-point grid within each grid block) and the corresponding kriging estimation errors calculated using the above GCF are shown in Figures 4-9 and 4-10, respectively. The kriged field illustrated in Figure 4-9 is the same initial kriged field used in each of the conditional simulations produced in this study. As mentioned in Chapter 3, the differences in the CS transmissivity fields are due to the difference in random seeds used in TUBA while generating the unconditional transmissivity simulation. Consistent with the 1990 study, Figure 4-9 depicts higher transmissivity values in the western part ($\log_{10}$ transmissivity from -3.0 to -3.5) of the model region and lower values ($\log_{10}$ transmissivity from -6.0 to -8.0) in the east. The lowest values of transmissivity occur in

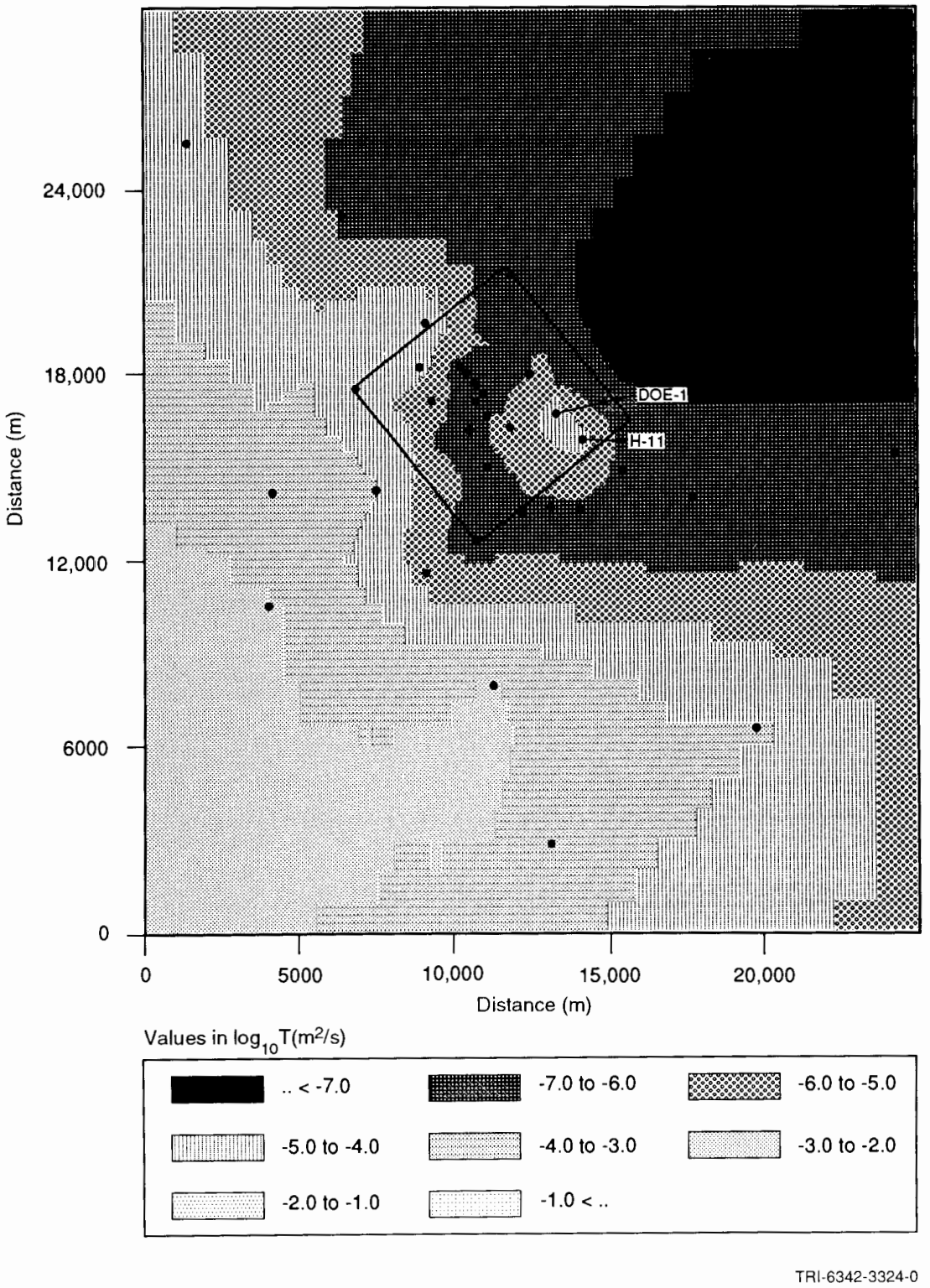

Figure 4-9. Initial kriged grid-block $\log_{10}$ transmissivity estimates (i.e., the average over the specific area of each block as determined using a 2×2 Gauss-point grid within each grid block).

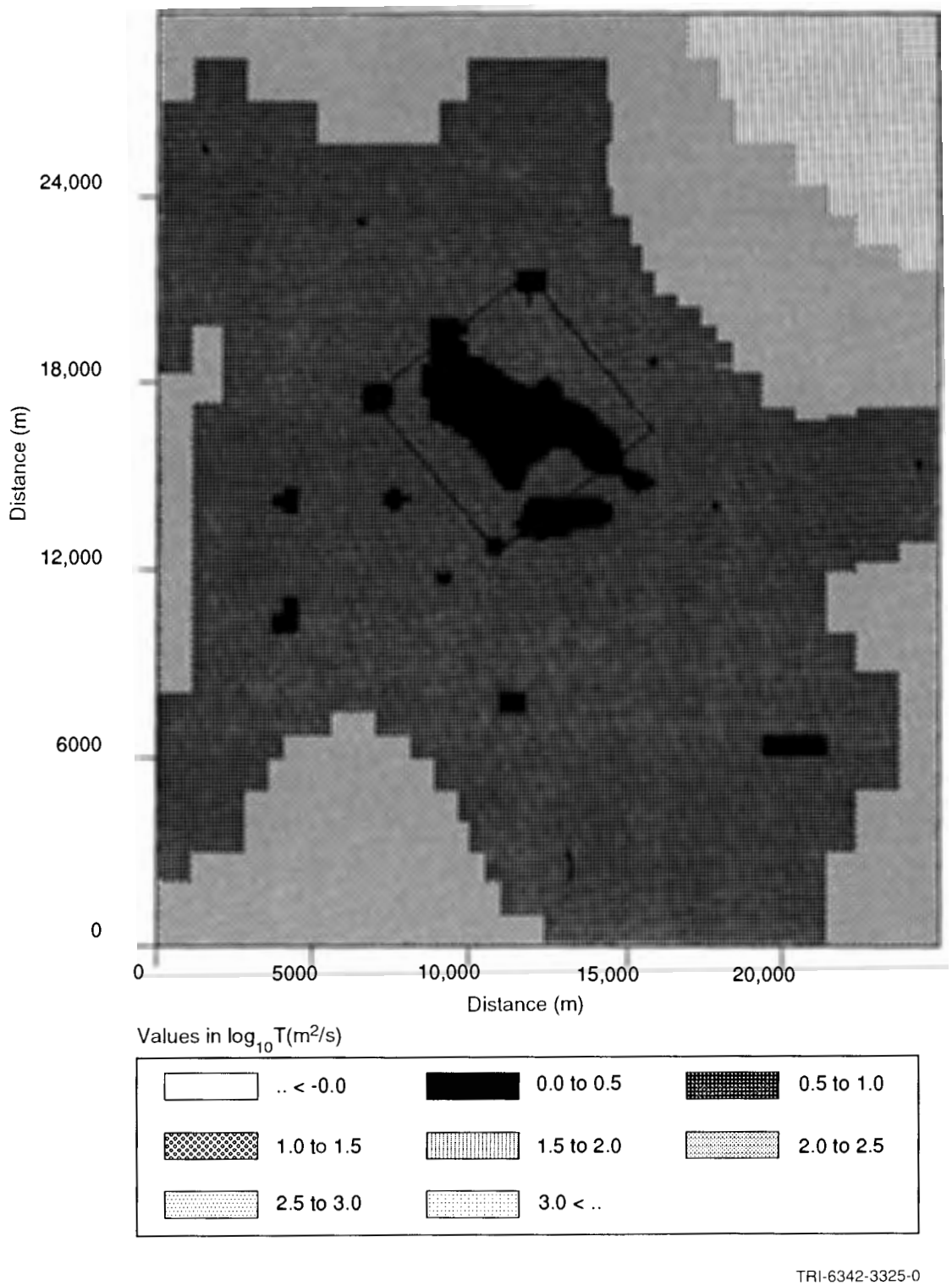

Figure 4-10. Estimation errors of the initial kriged field.

the eastern region and reflect the projection of the underlying local trends determined by AKRIP. A local transmissivity high occurs in the grid blocks within the vicinity of the H-11 and DOE-1 boreholes where fracturing is known to exist.

The estimation errors (as defined by one standard deviation) within the model region are highest in the northeast model region due to the lack of data in that area (Figure 4-10). Here the errors have values from 1.0 to 2.5 $\log_{10}$ T, T in m^2/s. Within the central portion of the model area, the errors of the estimate are between 0.5 and 0.75 for $\log_{10}$ T, T in m^2/s. As previously mentioned, during the optimization procedure in which the optimum transmissivity value is assigned to one or two pilot points, the range of transmissivity values considered plausible occurs within $\pm 3\sigma$ of the initial CS value.

4.2.3 Model Transient Time Steps

Over eight years of transient events were simulated in this study. In an attempt to reduce the computational time necessary to calibrate to the transient pressure data, only the major transient events, listed in Table 4-1, were considered in the 1992 model. The number of time steps was therefore reduced from approximately 380 in the 1990 model to 190 in the 1992 model.

4.3 Discussion of the Calibration of a Single Realization

In this section, the calibration of one of the seventy CS transmissivity fields is discussed in detail to illustrate the process used in GRASP-INV. As discussed in Chapter 3 and illustrated in Figure 3-1, the first step toward calibrating the CS fields to the steady-state and transient data involves the simulation step required to produce the initial conditional simulations. The grid used to produce the conditional simulations is finer than the finite-difference grid and, as discussed in Section 3.3.2, is referred to as the Gauss grid. The Gauss grid is generated by dividing each finite-difference grid block into four sections. Each section is considered to contain homogeneous and isotropic properties. All of the calculations required to produce a conditional simulation are conducted at the Gauss grid scale. Once the conditional simulation is generated, the four Gauss grid blocks within each finite-difference grid block are integrated using Gauss quadrature techniques to determine the single homogeneous, isotropic value assigned to each finite-difference grid block. The Gauss grid was necessary because the TUBA code used in this study did not currently have the capability of generating an IRF-k field of block-averaged values.

Prior to producing the initial conditional simulations of the $\log_{10}$ transmissivity field, a verification exercise was conducted to determine whether TUBA produced an unconditional (UC) field with a GCF as specified. The zero-order GCF previously discussed was used in this exercise, which required simulating a UC field and then sampling from the field and redetermining the GCF from the sampled data. After several fields were simulated and subsequently sampled, it was determined that while the coefficient of the GCF may vary slightly, the order and form of the GCF remained consistent with the GCF input to TUBA.

Figure 4-11 depicts the unconditional simulation (UCS) of a $\log_{10}$ transmissivity field on the Gauss grid with the GCF mentioned above. The UCS field has a high degree of spatial variability while containing the same broad

trends in transmissivity observed in the WIPP data. However, the actual locations of the higher and lower transmissivity regions do not coincide with those observed at the WIPP site. This is expected because the field has not yet been conditioned to the WIPP data. As discussed in Chapter 3, the second step in the process of producing a conditional simulation requires the UCS to be sampled (i.e., values noted) in the same locations as the observed data and used as input to the kriging processor to determine the simulated kriged (SK) field. The simulated kriged field is determined by using the UC sampled values as input and subsequently kriging to obtain estimates at the Gauss grid-block centers. Figure 4-12 illustrates the kriged field using the UC sampled data as input. While reproducing the average nature of the UC transmissivity field over the model domain, the kriged estimates do not reproduce the spatial variability or underlying reality of the UC field.

The differences between the UCS field and the SK field are shown in Figure 4-13. It is these differences that are added to the initial kriged field mentioned in Section 4.2.2 to produce the conditional simulation. The differences represent the spatial variability that is lost when kriging is employed to estimate a parameter field because of the smoothing effect of the kriging algorithm and because the sample set is relatively small. Since kriging honors values at measurement locations, the differences between the UCS and SK fields are very small at the sample locations. (Note: In the absence of measurement error at the observed locations, the differences at these locations will be zero.) Away from measurement locations, the differences increase with values of up to +/- 3.0 $\log_{10}$ T. Negative differences indicate that the UCS field has lower $\log_{10}$ T values than the SK field whereas positive differences indicate higher $\log_{10}$ T values in the UCS field than in the SK field.

After the addition of the differences illustrated in Figure 4-13 to the initial kriged field (Figure 4-9), the initial CS field is obtained (Figure 4-14). As previously mentioned, the addition is conducted at each of the Gauss grid-block centers. While the general trends are the same between the initial CS and initial kriged fields, the initial CS field has a much higher degree of spatial variability than the initial kriged field. The broad continuous features observed in the kriged transmissivity field are much narrower and discontinuous in the initial CS field. The high-transmissivity region in the vicinity of the H-11 and DOE-1 boreholes is significantly larger in the initial CS field due to the addition of the positive differences south of H-3. After integrating the Gauss grid values using Gauss quadrature techniques, the finite-difference grid block values were obtained. The integration over the Gauss grid slightly reduced the spatial variability represented in Figure 4-14 due to the larger areas each finite-difference grid block represents (Figure 4-15).

The initial steady-state groundwater flow simulation was then conducted using the boundary conditions listed in Table 4-3 and the initial CS transmissivities illustrated in Figure 4-15. Figure 4-16 contains a contour map of the differences between the calculated and observed freshwater heads. The northwest region of the WIPP site (i.e., the W-25, P-14 and H-18 boreholes) contains the highest head differences (-16 to -18 m) implying a significant need for additional groundwater flux to this area.

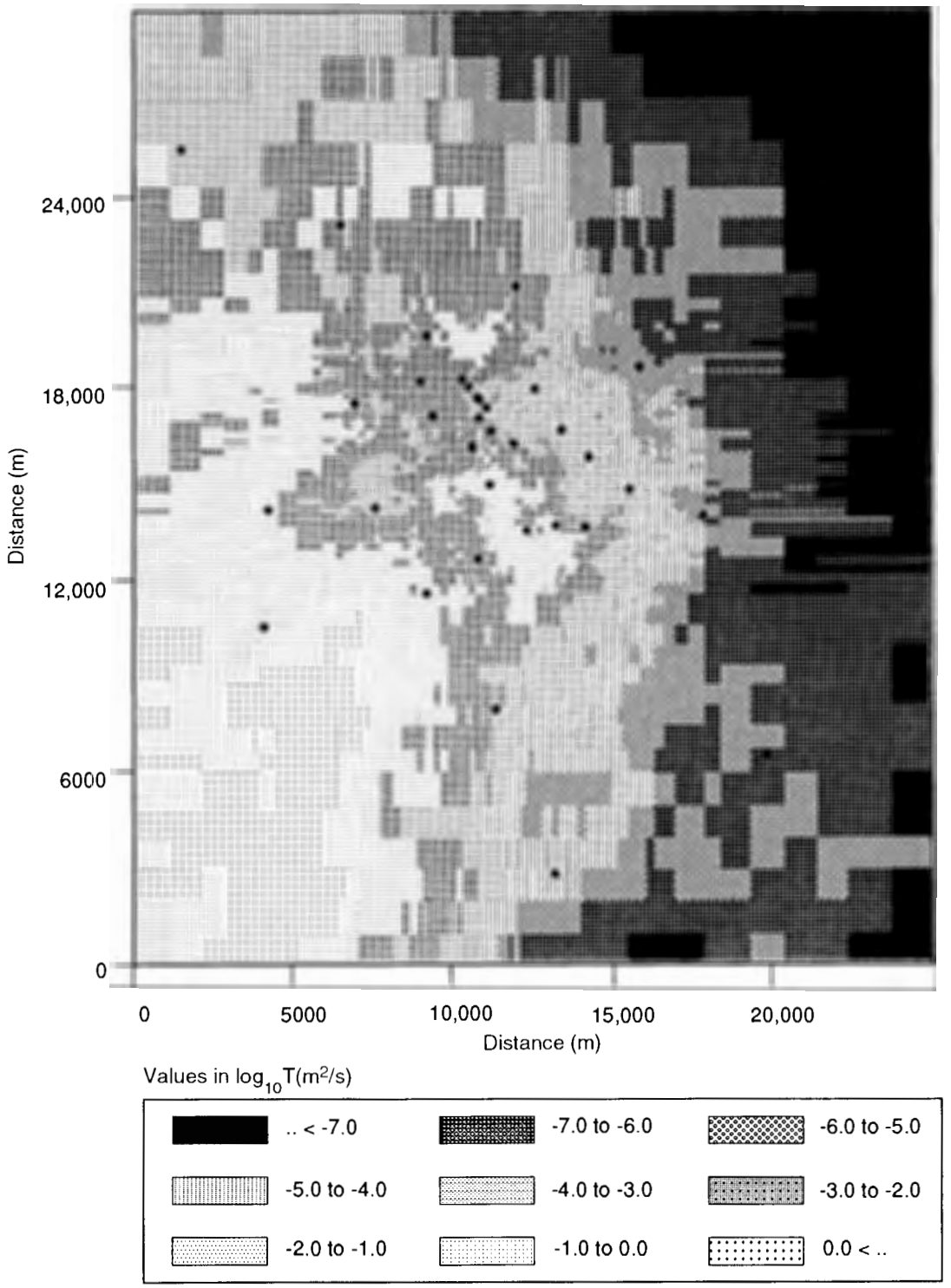

TRI-6342-3326-0

Figure 4-11. Unconditional simulation of a $\log_{10}$ transmissivity field on the Gauss grid.

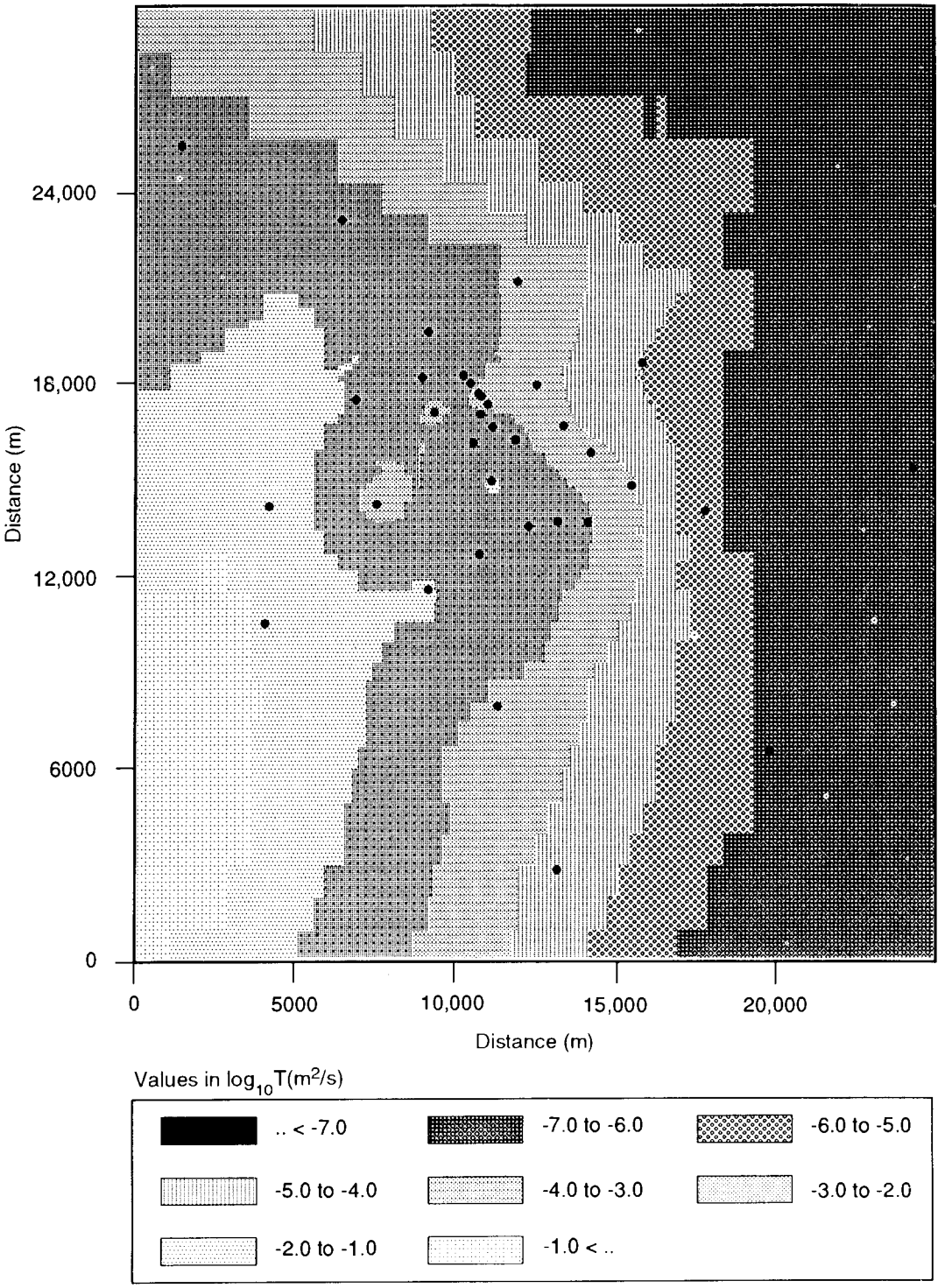

TRI-6342-3327-0

Figure 4-12. Kriged field using the unconditional sampled data as input.

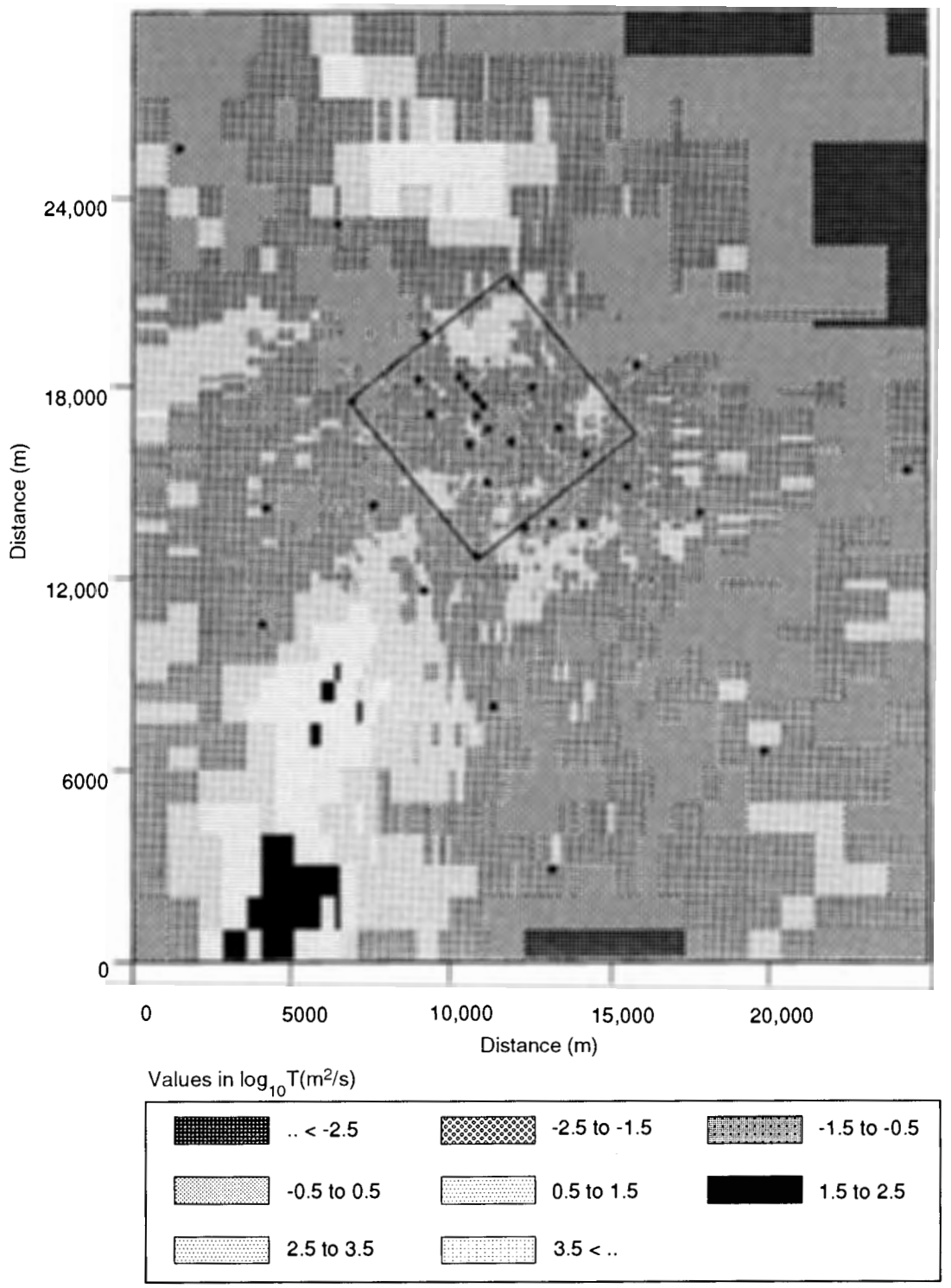

TRI-6342-3328-0

Figure 4-13. Differences between the unconditional simulation (UCS) field (Figure 4-11) and the simulated kriged (SK) field (Figure 4-12).

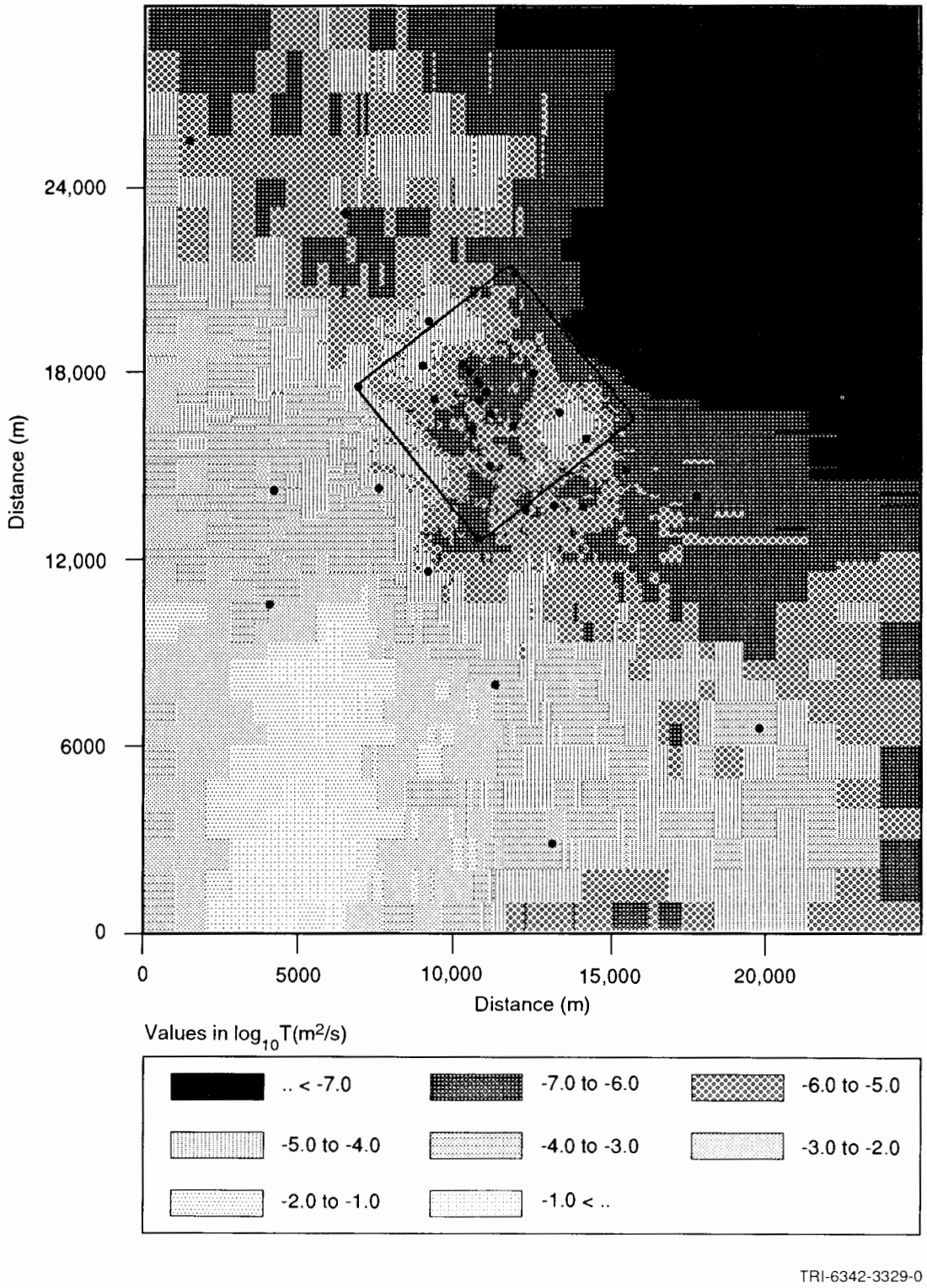

Figure 4-14. Initial conditionally simulated (CS) field of the example realization on the Gauss grid.

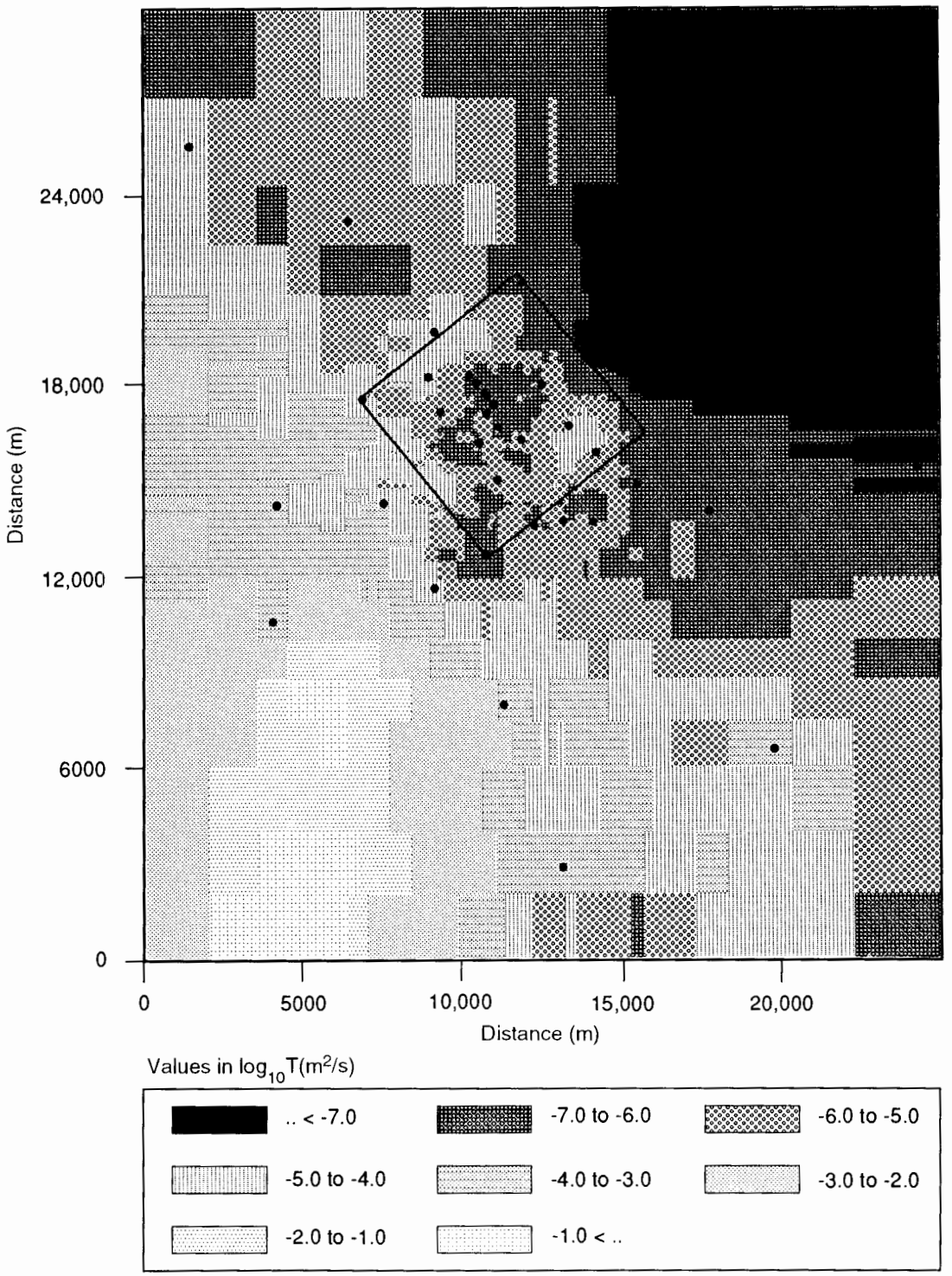

TRI-6342-3330-0

Figure 4-15. Initial conditionally simulated (CS) field of the example realization on the finite-difference grid.

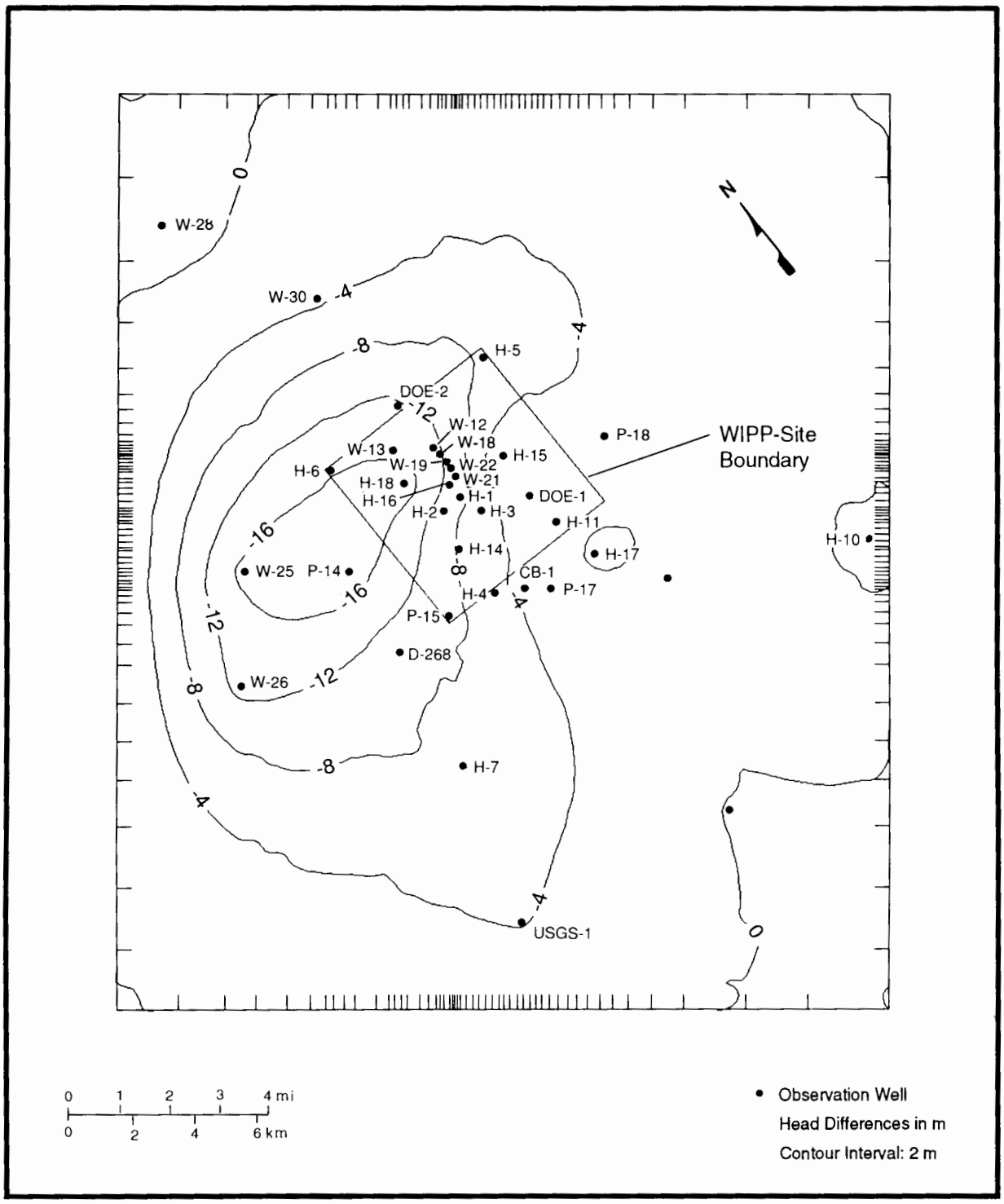

TRI-6342-3317-0

Figure 4-16. Contour map of the differences between the calculated and observed freshwater heads.

As discussed in Chapter 3, the steady-state performance measure used during calibration consisted of the sum of the squared deviations of calculated and observed heads. The normalized sensitivities of the performance measure to an increase in model transmissivities are shown in Figure 4-17. The sensitivity values are calculated at potential pilot-point locations (i.e., at the grid-block centers) and indicate the change in the performance measure for a unit increase in the transmissivity assigned to a pilot point. The highest sensitivity region has a negative sign and occurs in the northwest model area. The negative sign indicates that the performance measure and the selected system parameter are inversely proportional. Thus, an increase in the transmissivity field in the high negative sensitivity region will increase groundwater flux to the northwest model region and subsequently decrease the performance measure (i.e., reduce the head differences).

One pilot point was automatically located by GRASP-INV in the grid block with the highest sensitivity value. The value assigned to this pilot point was selected through optimization routines. The initial value at the pilot point location was -4.39 $\log_{10}$T m^2/s. The value initially assigned by the optimization routines was outside the plausibility criteria ($\pm 3\sigma$) at the pilot-point location. Therefore, GRASP-INV readjusted the assigned value to fall just within the $\pm 3\sigma$ range and assigned the $\log_{10} T$ uncertainty value to the pilot point. The pilot point was then added to the transmissivity data set used to generate a conditional simulation. Figure 4-18 depicts the CS field during the second step of the steady-state calibration. The transmissivities in the northwest region were increased (Figure 4-19), and the performance measure was subsequently reduced from the initial value of 2.64×10^{11} Pa^2 to 9.36×10^{10} Pa^2. As the flow chart shown in Figure 3-1 illustrates, the process of iteratively assigning pilot points in areas of high sensitivity and regenerating the conditional simulation continues until either the minimum steady-state performance measure is achieved or until the maximum number of pilot points is added. (In this study, 50 were added for steady-state calibration.)

Transient calibration is conducted in much the same fashion as steady-state calibration. The main difference between the two is the specification of a time window over which the transient pressure deviations between the observed and calculated data are determined. As previously mentioned, the major transient tests were simulated in chronological order. Calibration to these tests was therefore also conducted chronologically. To illustrate the transient calibration process, an example is taken from the pumping test conducted at the H-11 borehole in 1988.

Figure 4-20 illustrates the DOE-1 and H-15 transient hydrographs and their response to pumping at the H-11 borehole prior to transient calibration. The calculated pressure data illustrate the need for additional calibration in order to reproduce the observed drawdowns. A performance measure was selected consisting of the sum of the squared deviations between the calculated and observed pressures at the H-15 and DOE-1 boreholes. The time window was specified over the period of the H-11 pumping test (Figure 4-20). The sensitivity of the performance measure to the increase in model transmissivities identified a high-sensitivity region just south of the H-15 borehole. GRASP-INV assigned two pilot points in this region, which subsequently increased the transmissivities between the H-11 and H-15 boreholes. After two additional calibration steps, in which four more pilot points were added by GRASP-INV, the differences between the calculated and observed pressures at the DOE-1 and H-15 boreholes were acceptable.

Figure 4-21 shows the calibrated CS transmissivity field for the realization discussed in this section. The differences between the initial CS and the calibrated CS fields, shown in Figure 4-22, include the introduction of a

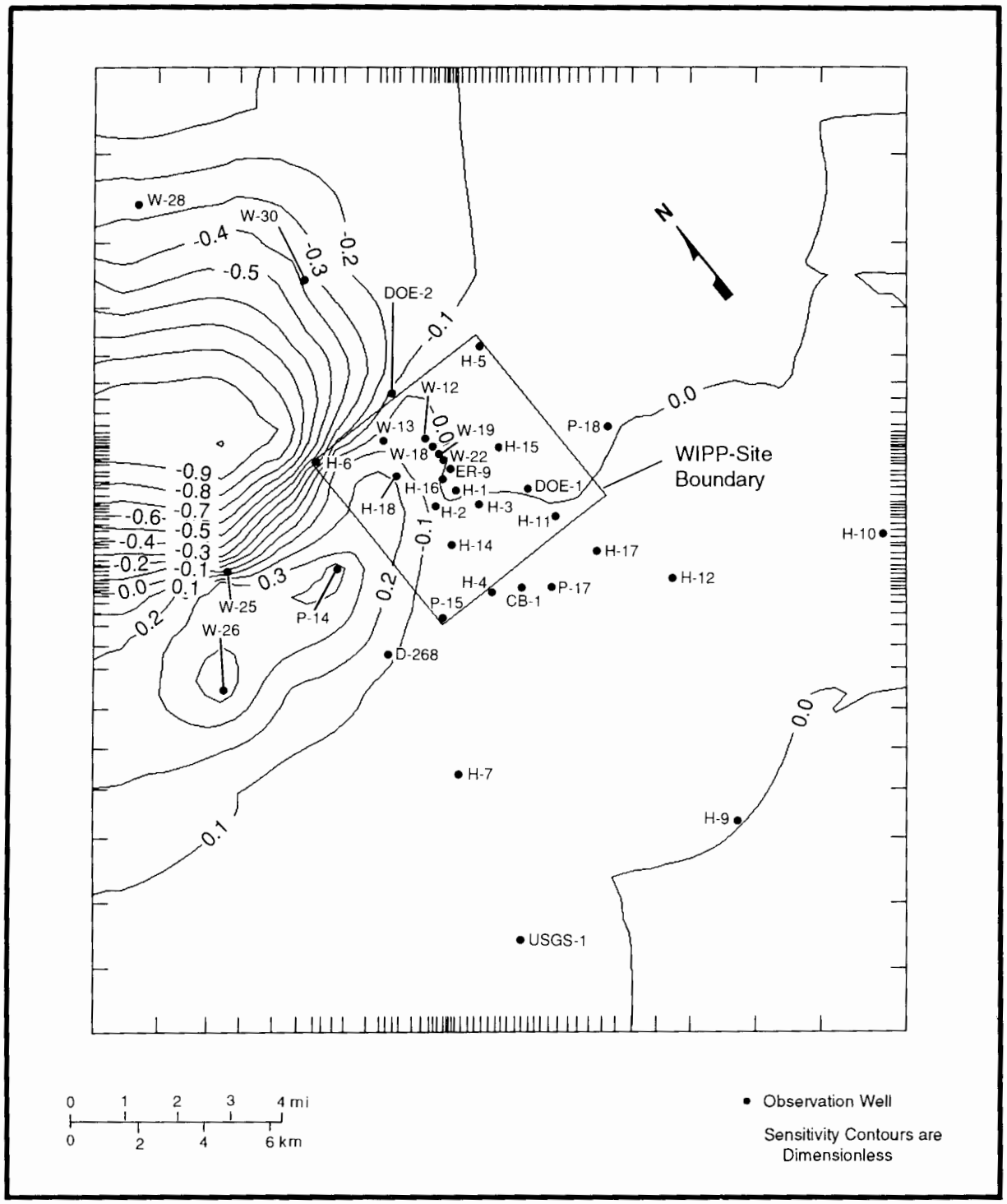

TRI-6342-3323-0

Figure 4-17. Sensitivities of the initial steady-state performance measure to an increase in model transmissivities.

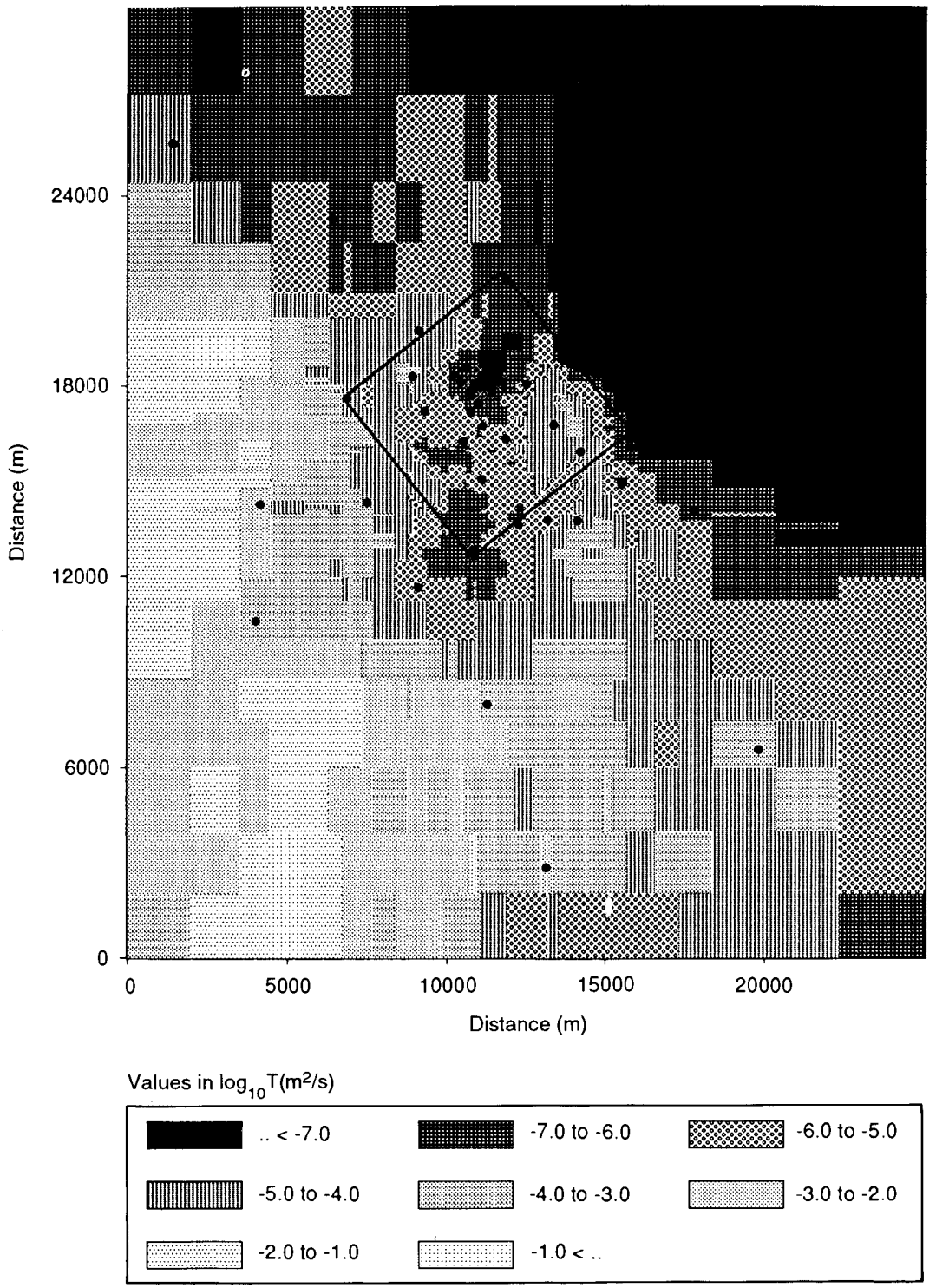

TRI-6342-3332-0

Figure 4-18. The conditionally simulated (CS) field during the second step of the steady-state calibration.

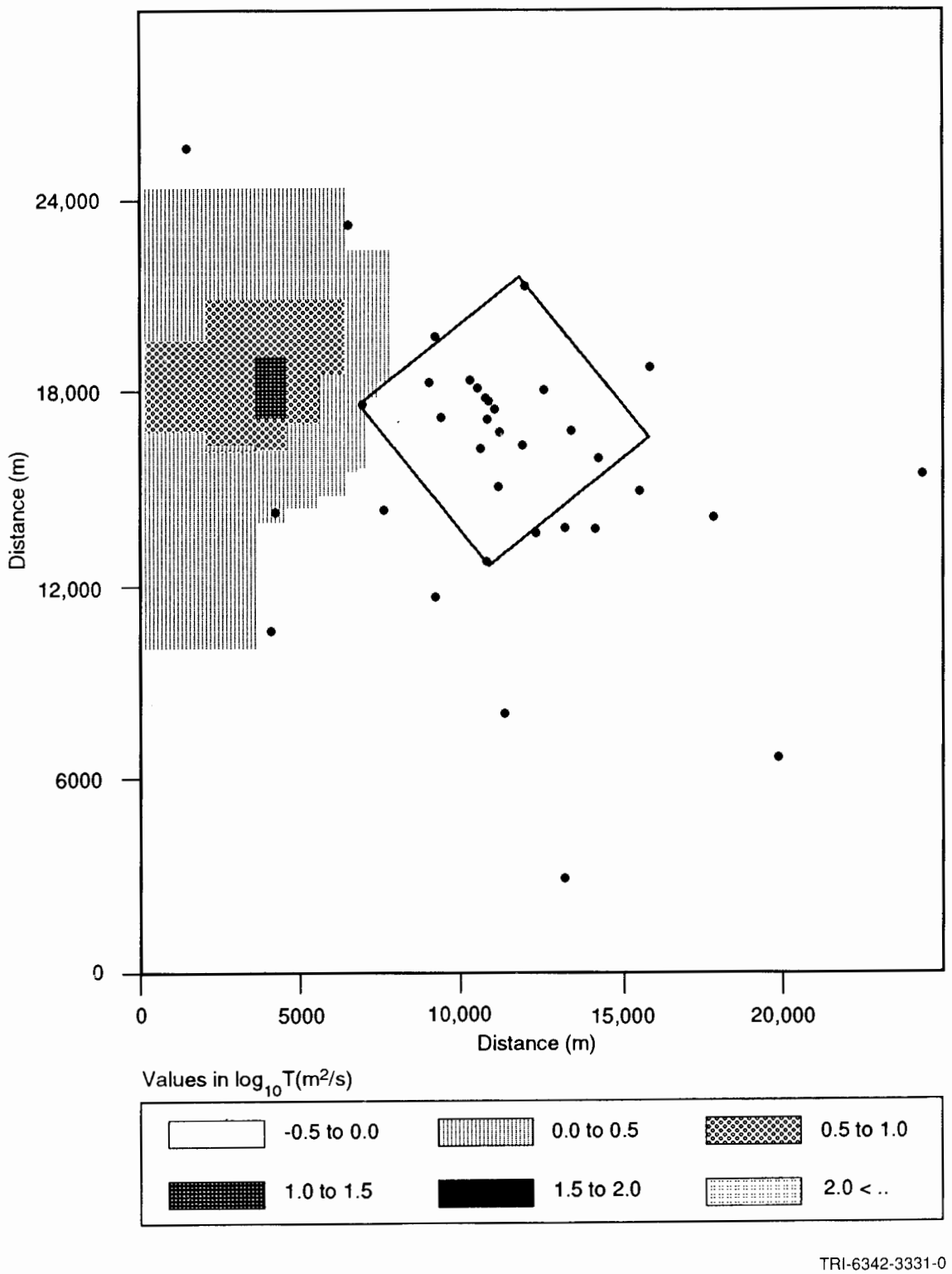

Figure 4-19. Increase in transmissivities after a pilot point was added during steady-state calibration.

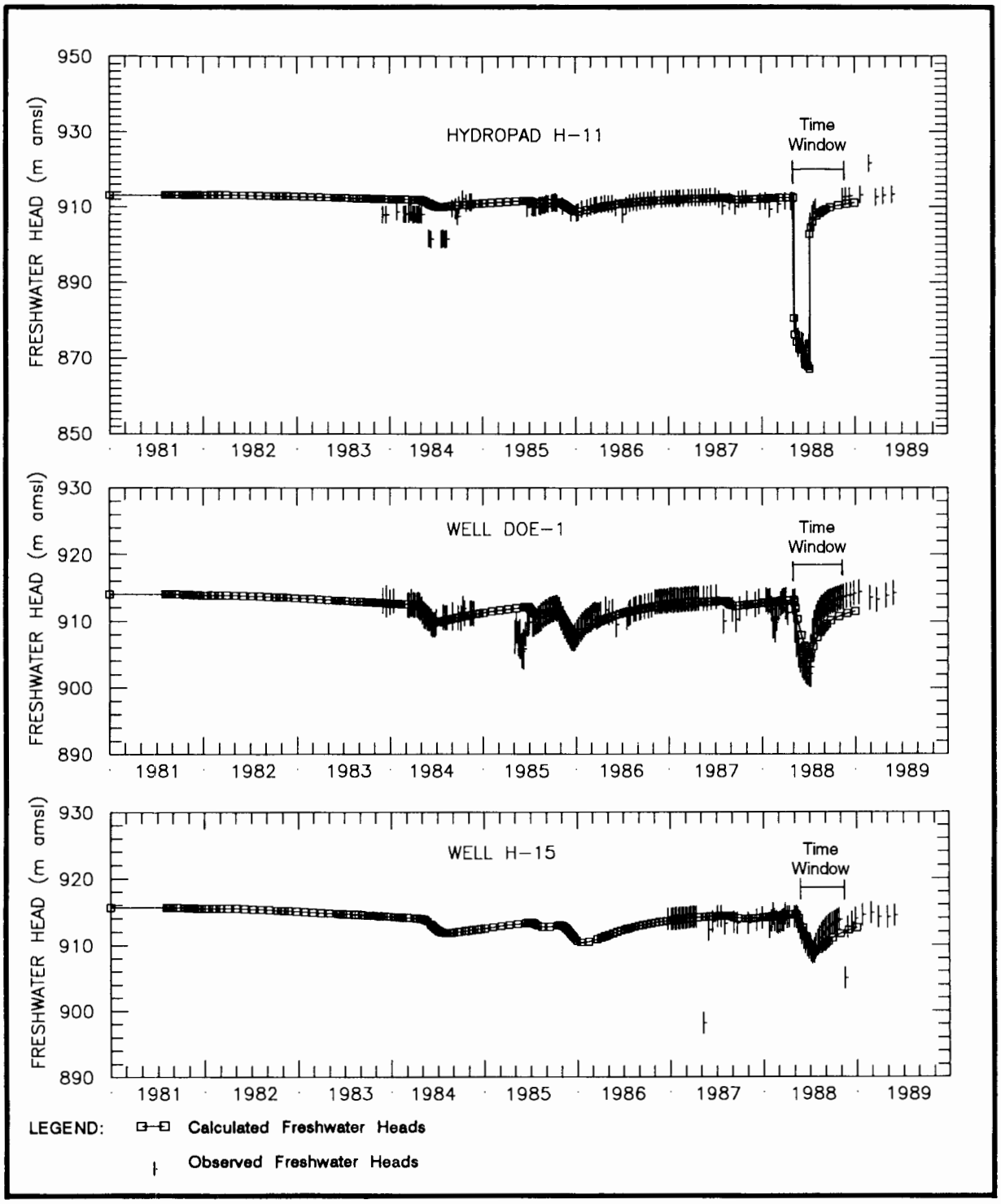

TRI-6342-3346-0

Figure 4-20. DOE-1 and H-15 transient hydrographs and their response to pumping at the H-11 borehole.

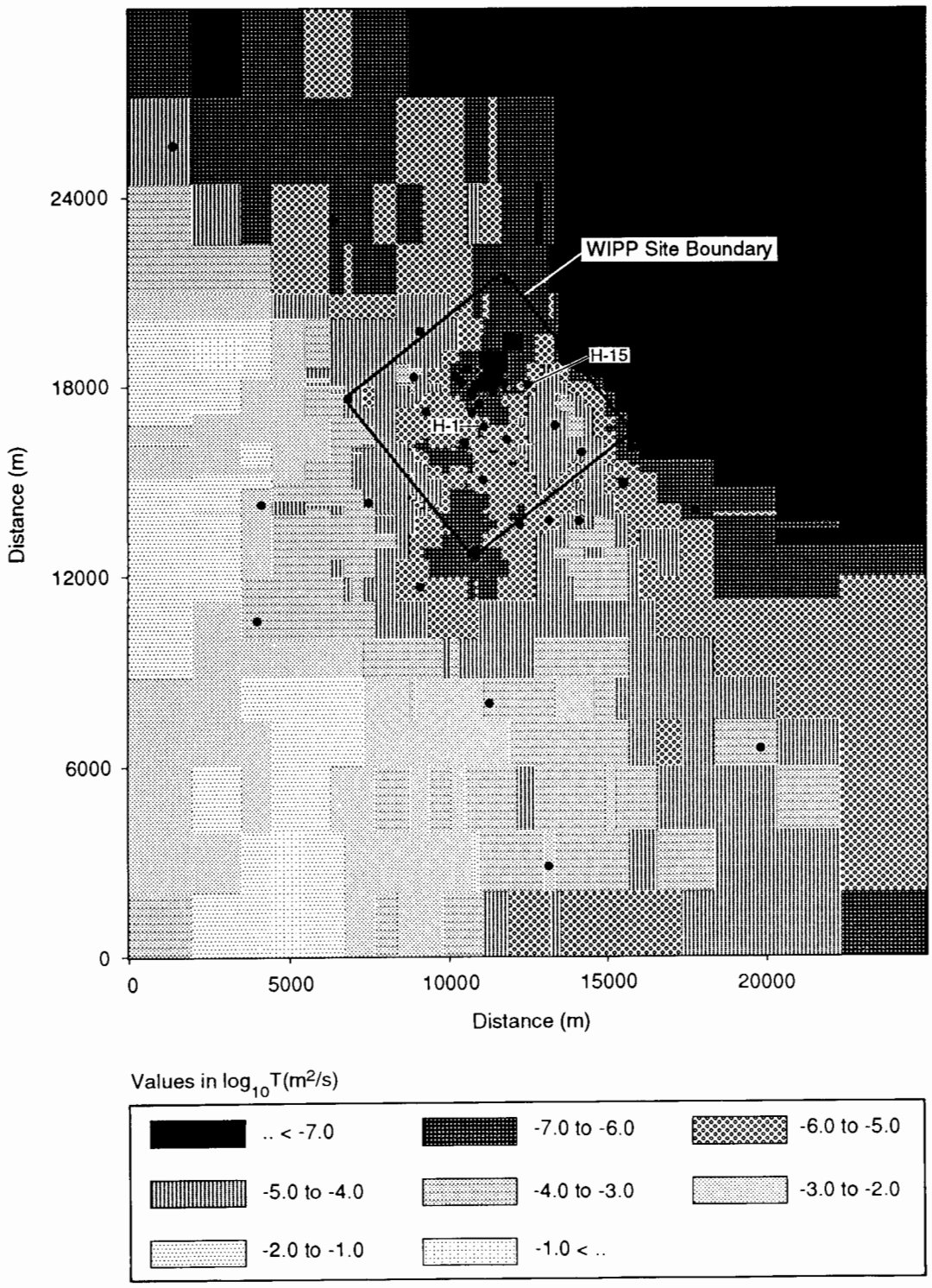

TRI-6342-3428-0

Figure 4-21. Calibrated conditionally simulated (CS) transmissivity field.

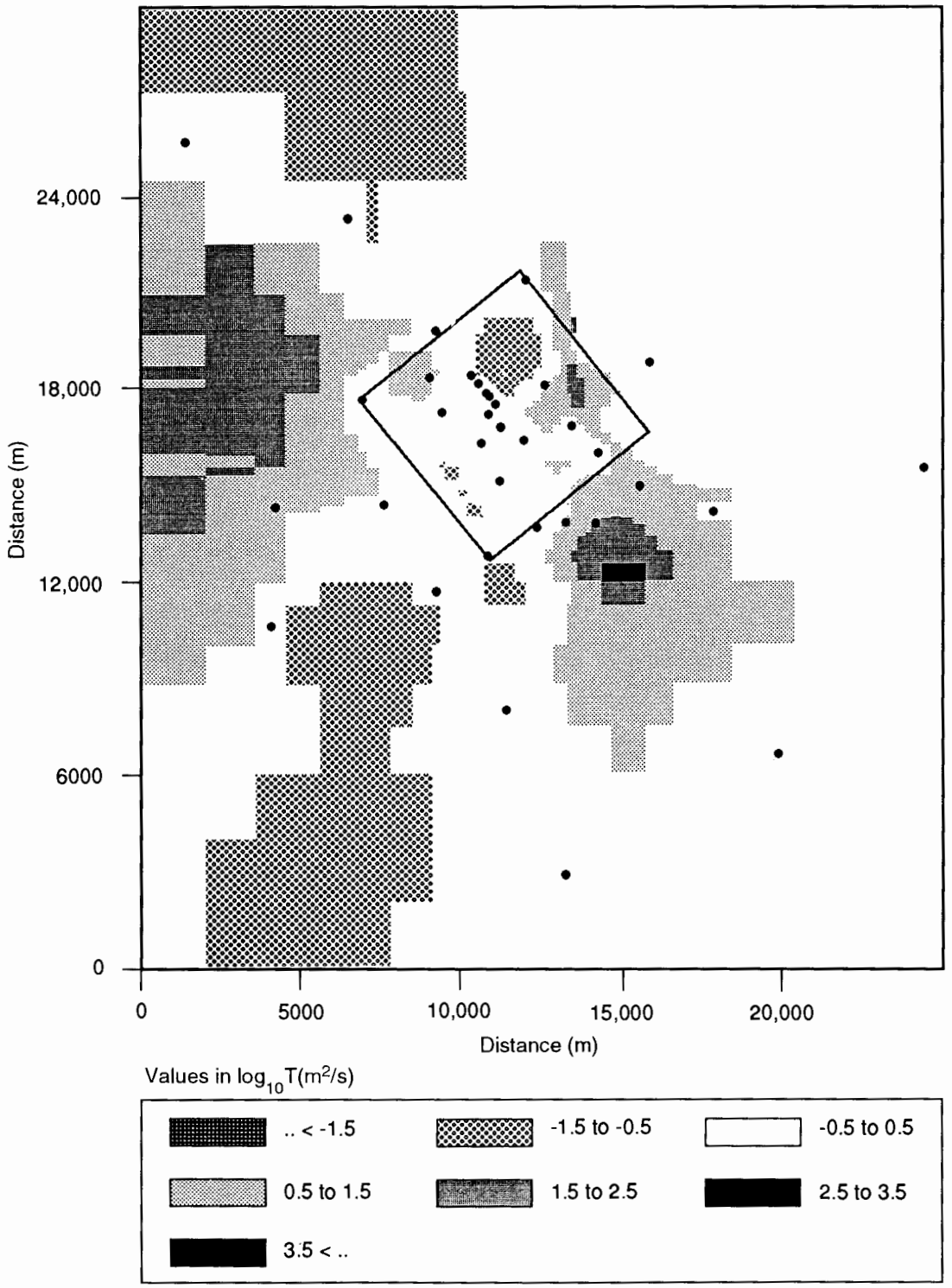

TRI-6342-3333-0

Figure 4-22. Differences between initial and calibrated conditionally simulated (CS) transmissivity fields.

narrow high-transmissivity zone south of H-15. The calibrated CS field has a much more tortuous high-transmissivity zone relative to the results determined in the 1990 study. The travel path through the CS field is illustrated in Figure 4-23. The travel time to the southern WIPP-site boundary is approximately 21,500 yr, 7000 yr longer than the 1990 travel time value. The increase is due to a longer travel distance through lower transmissivities in the vicinity of H-1 to the point at which the groundwater enters the extension of the high-transmissivity zone.

4.4 Discussion of the Ensemble of Calibrated Conditionally Simulated Transmissivity Fields

4.4.1 Ensemble Mean Transmissivities

The example described in Section 4.3 illustrates the procedure used in this study to calibrate 70 CS transmissivity fields. Each CS field was composed of an underlying kriged field to which a conditional random error field was added. The error field varied for each of the 70 realizations due to the random seeds input to the Turning Bands algothrim. Thus, each of the calibrated CS transmissivity fields has a different spatial distribution of transmissivities. In some cases, the high-transmissivity zone is a broad feature that extends from the DOE-1 borehole in the east WIPP-site area to the H-14 borehole west of H-3. In other cases, the high-transmissivity zone has a narrow, tortuous and in some instances, discontinuous nature.

In an attempt to compare the mean transmissivity field determined in this study to the transmissivity field of the 1990 study, an ensemble mean calculation was performed across the realizations to determine the average transmissivity value at each grid block. The resulting ensemble transmissivity field (Figures 4-24 and 4-25) has features which are very similar to the 1990 kriged transmissivity field (Figure 4-26). Outside of the WIPP-site area, the re-entry of high transmissivities from the Nash Draw area occurs south of the WIPP site near the H-7 borehole in both the 1990 results and in the ensemble mean field. The high-transmissivity zone within the WIPP-site boundary, as represented in the ensemble mean field (Figure 4-25), extends northward from the P-17 borehole where it narrowly lies between the P-17 and H-17 boreholes. Once crossing the southern WIPP-site boundary, the high-transmissivity zone widens significantly extending westward to the H-3 borehole and eastward beyond the H-11 and DOE-1 boreholes.

4.4.2 Ensemble Steady-State Head Differences

A root-mean squared error (RMSE) between calculated and observed steady-state heads was calculated in order to summarize the fit of each realization to the steady-state data. The RMSE values at each of the boreholes that had steady-state observed head data were summed within each simulation to obtain an average RMSE. A histogram of the average RMSE value for each of the 70 simulations (Figure 4-27) depicts a mean RMSE value within the simulations between 1.5 and 2.5 m. The simulation with the worst steady-state head fit is shown to have an average RMSE value between 6.5 and 7.5 m. This particular realization illustrates a situation in which the difference field (added to the kriged field during the CS process) significantly reduced the ability of the GRASP-INV code to calibrate the field to steady-state conditions within 50 calibration steps. This situation occurs when the initial CS field

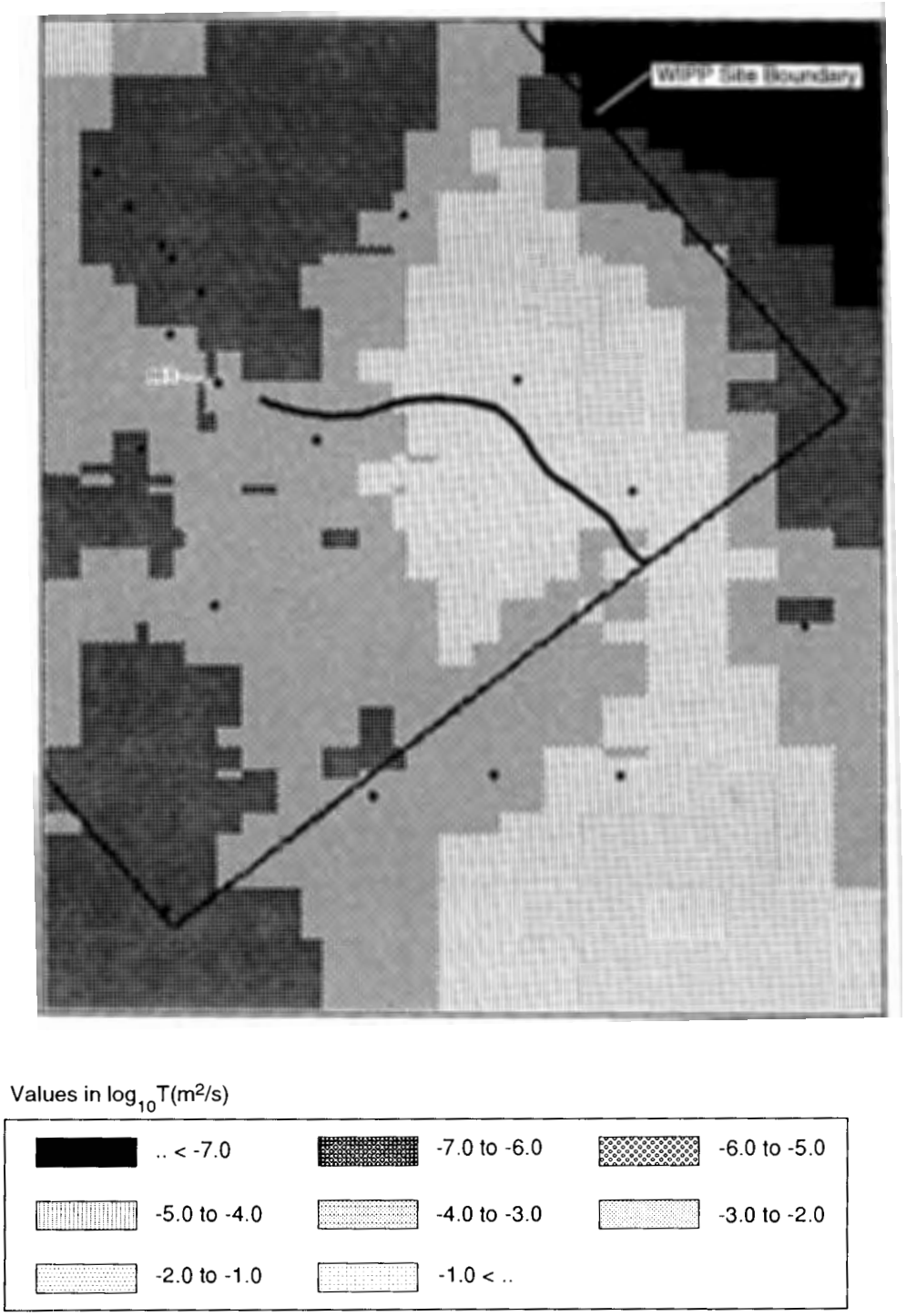

Figure 4-23. Groundwater travel path through calibrated conditionally simulated (CS) field.

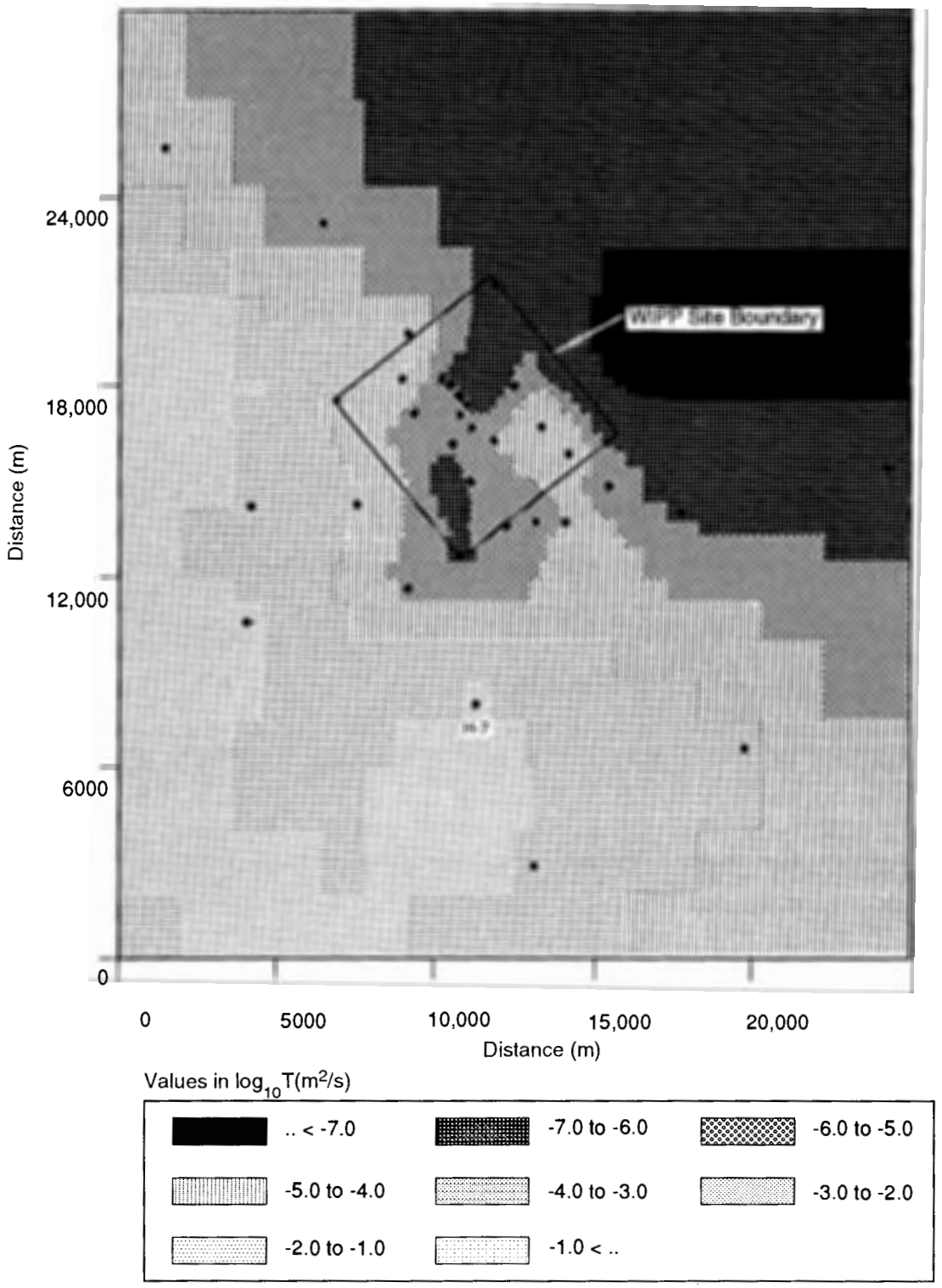

Figure 4-24. Ensemble transmissivity field resulting from a mean calculation performed across the realizations.

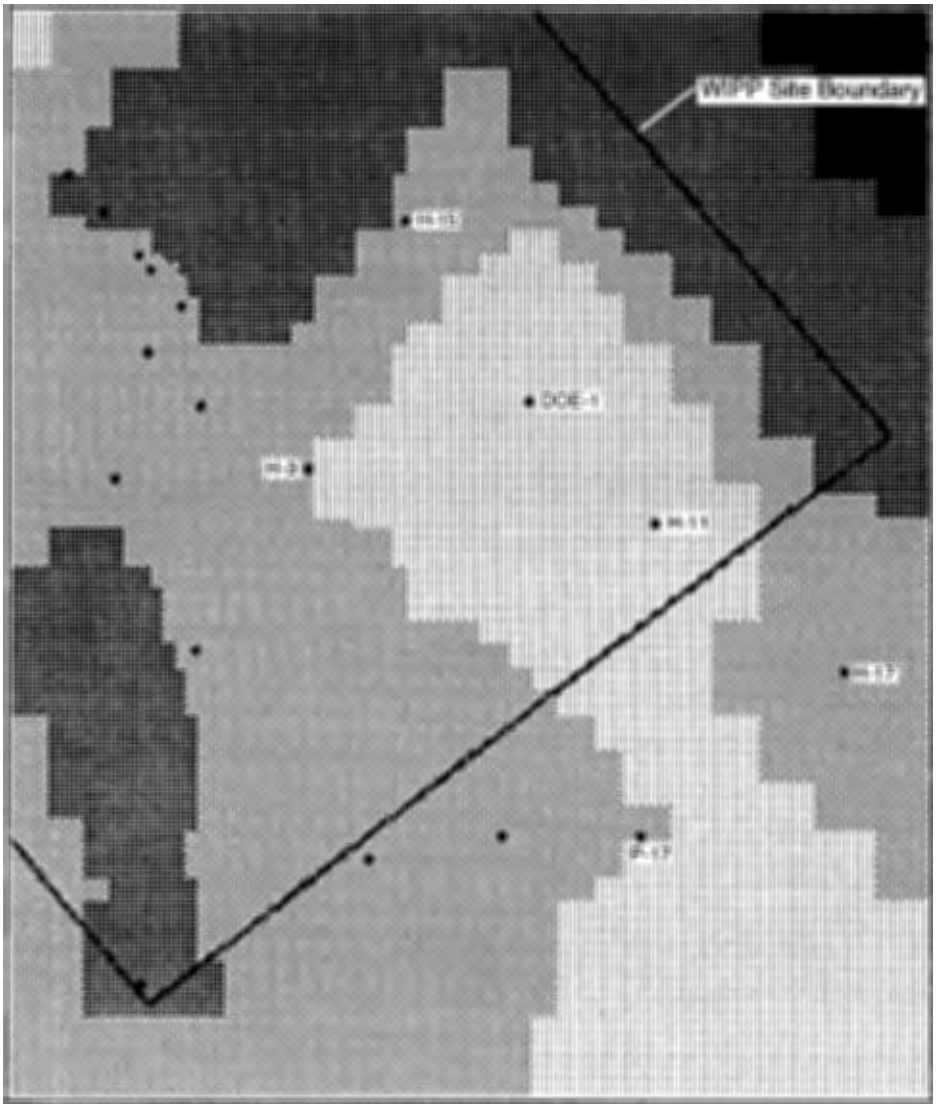

Values in $\log_{10}T(m^2/s)$

.. < -7.0	-7.0 to -6.0	-6.0 to -5.0
-5.0 to -4.0	-4.0 to -3.0	-3.0 to -2.0
-2.0 to -1.0	-1.0 < ..	

TRI-6342-3335-0

Figure 4-25. Ensemble transmissivity field in the vicinity of the southern WIPP-site boundary.

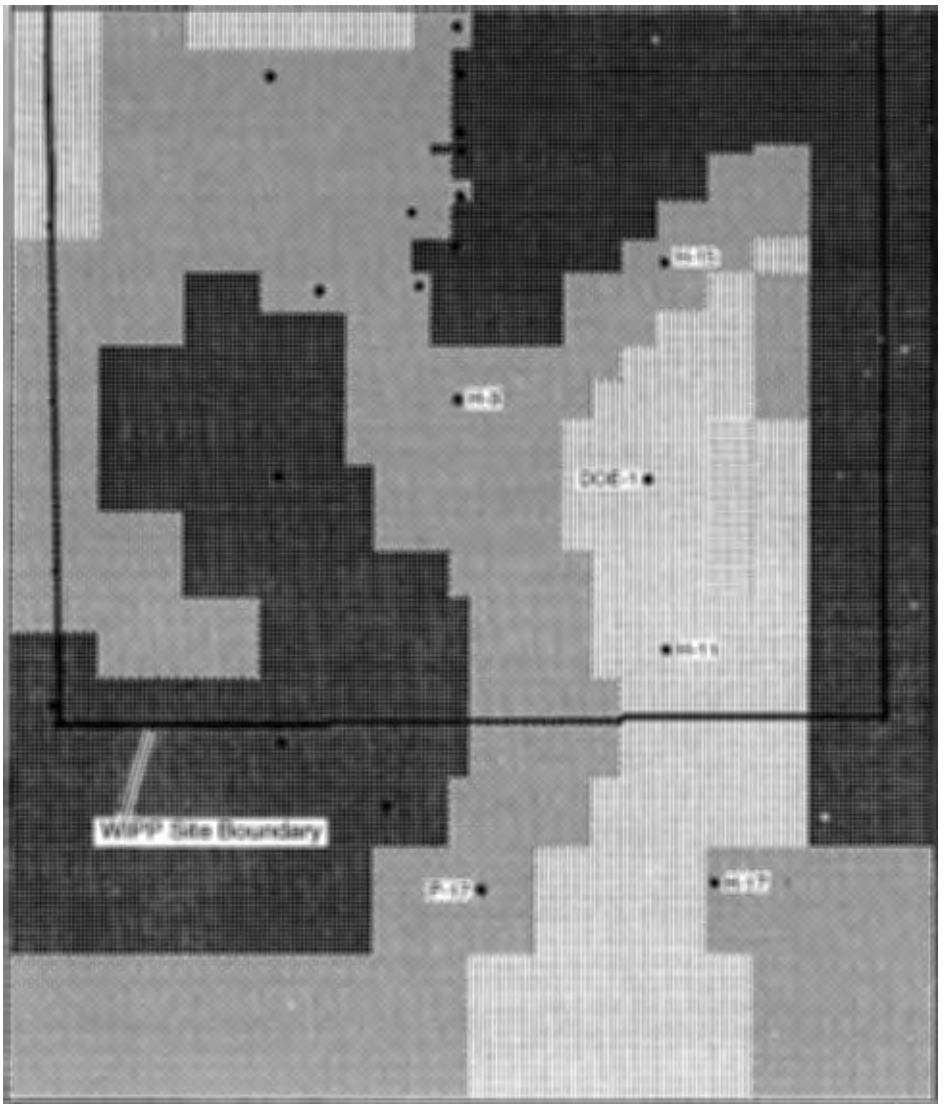

Values in $\log_{10}T(m^2/s)$

.. < -7.0	-7.0 to -6.0	-6.0 to -5.0
-5.0 to -4.0	-4.0 to -3.0	-3.0 to -2.0
-2.0 to -1.0	-1.0 < ..	

TRI-6342-3336-0

Figure 4-26. Calibrated transmissivities of the 1990 model in the vicinity of the southern WIPP-site boundary. (Note: Aspect ratio of figure is not [1:1].)

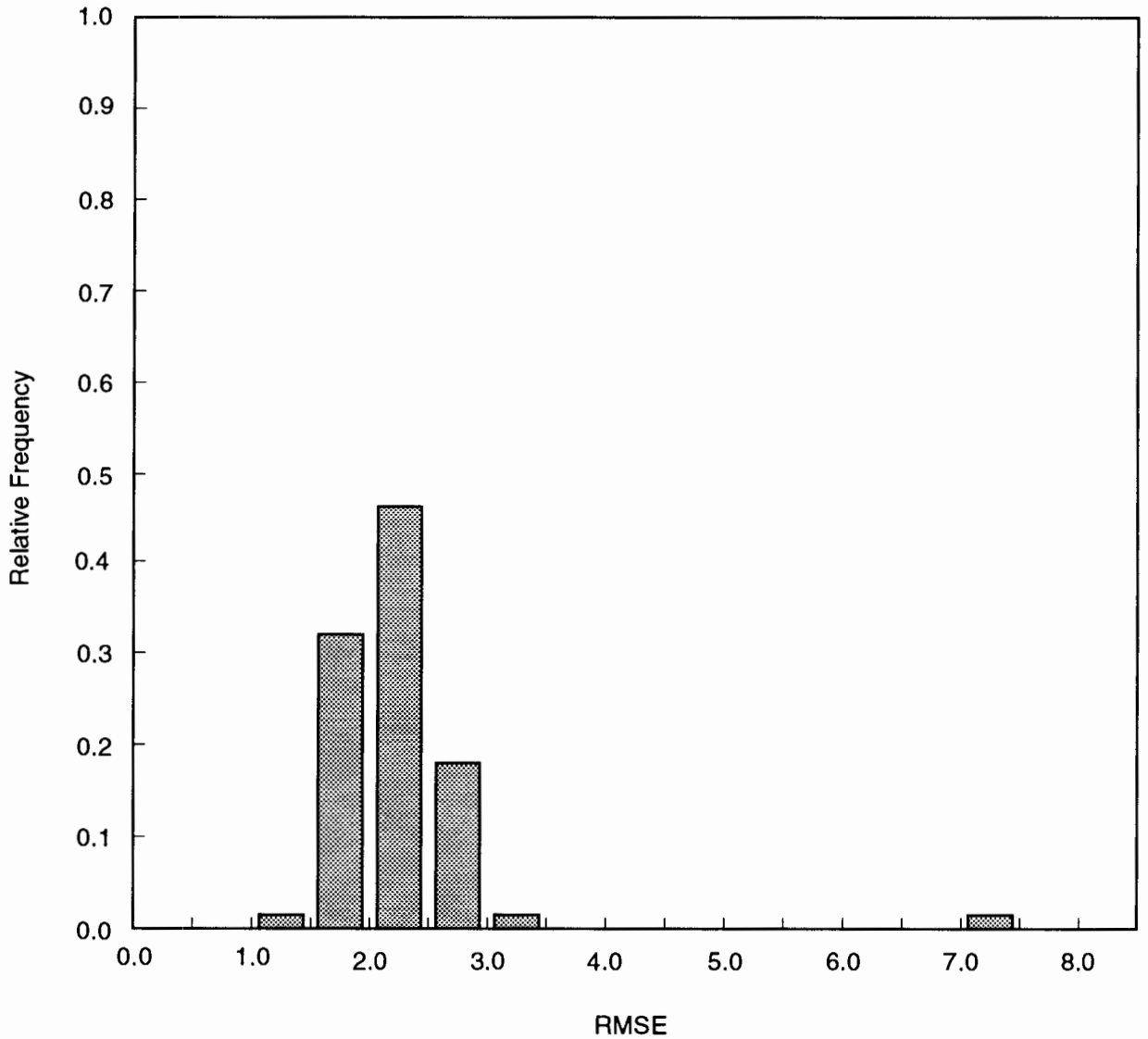

TRI-6342-3344-0

Figure 4-27. Histogram of the average, root-mean squared error (RMSE) value for each of the 70 simulations.

generated has features that produce significantly high initial-head differences. The GRASP-INV code then has to add more pilot points to modify the CS field to bring the head field into agreement with the observed data than may be necessary for an initial CS field which produces initial head differences that are low. Because a fixed number of pilot points were specified for calibrating to the steady-state data, some fields had smaller RMSE values than others.

RMSE values were also calculated to determine average head differences over the ensemble of realizations at each borehole location (Table 4-4). Figure 4-28 shows a contour surface of the RMSE values over the model domain. The maximum average difference between the calculated and observed data occurs at the H-7 borehole where the RMSE value is -4.3 m. (Note: The sign of the RMSE was assigned after evaluating the ensemble differences.) The head differences in the southern model and central WIPP-site area also have negative signs with average values ranging between -0.7 m and -2.8 m. The regions that have positive head differences occur in the area immediately east of the H-11 borehole and in the area between the P-14 and WIPP-26 boreholes. The average head differences in these regions are greater than 2.0 m. The difference at the H-17 borehole is the highest with a positive value of 3.4 m.

Table 4-4. Average Root-Mean Squared Error (RMSE) Values for the Ensemble Differences between Calculated and Observed Heads.

Well Location	Head Difference (m)
H-1	-1.90
H-2	-1.31
H-3	-1.02
H-4	-0.99
H-5	+1.11
H-6	+0.91
H-7	-4.27
H-9	+2.17
H-10	+1.34
H-11	+1.48
H-12	+1.22
H-14	-0.96
H-15	+2.22
H-17	+3.44
H-18	-2.63
P-14	+2.61
P-15	-2.00
P-17	+0.73
WIPP-12	+0.67
WIPP-13	-0.78
WIPP-18	-0.93
WIPP-25	+2.94
WIPP-26	+2.19
WIPP-28	+1.45
WIPP-30	+1.30
CB-1	-0.69
DOE-1	+1.27
DOE-2	+0.69
D-268	+1.74
USGS-1	-2.84

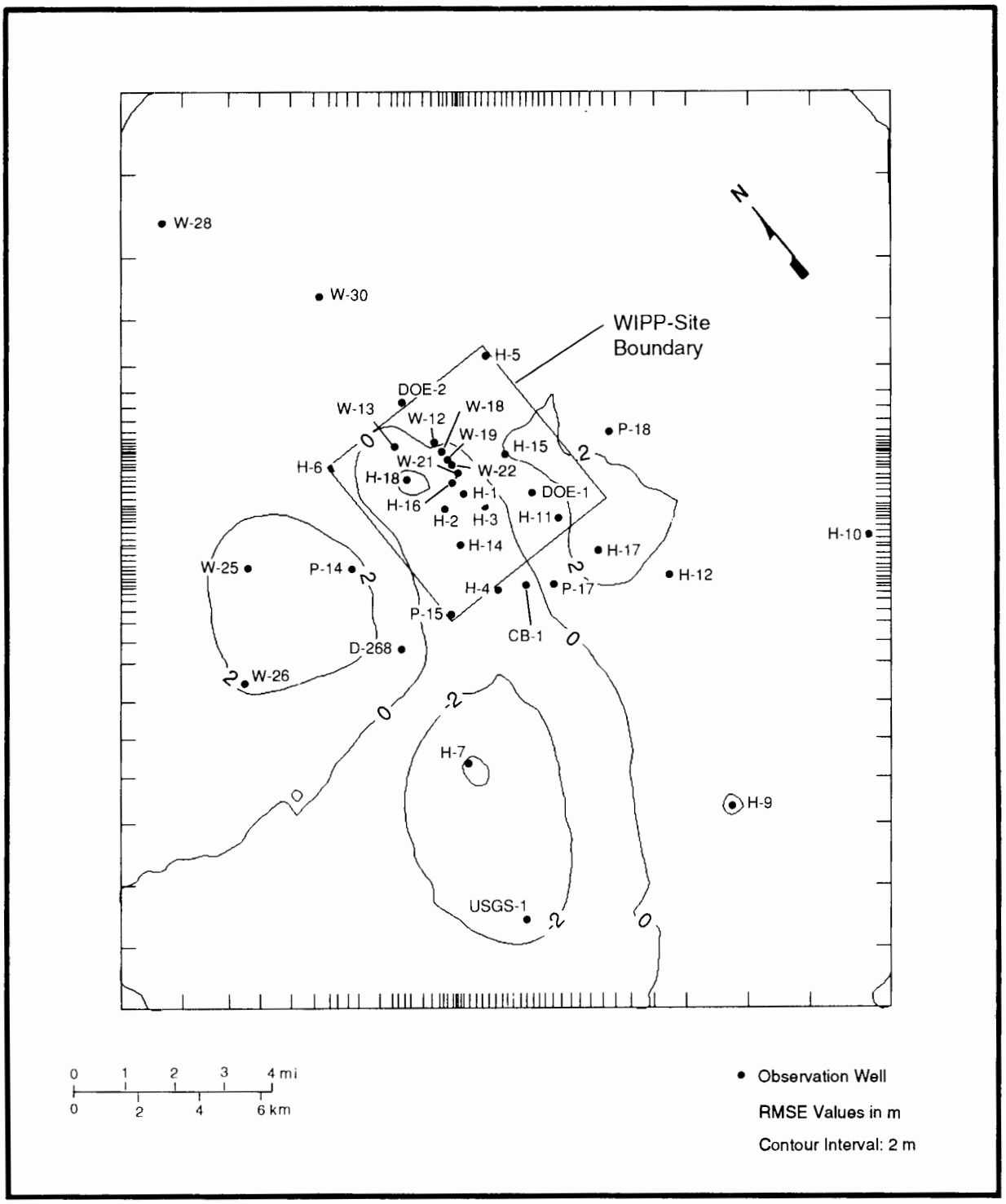

TRI-6342-3319-0

Figure 4-28. Contour surface of the root-mean squared error (RMSE) values over the model domain.

The average head differences at the H-7, WIPP-25, WIPP-26, and P-14 boreholes, illustrated in Figure 4-28, indicate that the boundary conditions specified along the southern and western boundaries are not consistent with the observed heads. Several iterations were made to the boundary conditions prior to beginning the calibration exercise. The iterations were necessary due to the difficulty in matching the H-7, USGS-1, and H-9 observed heads while properly fitting the heads in the rest of the model domain. The difficulty arises from the existence of the no-flow region along the Nash Draw axis and the extremely flat hydraulic gradients in the southern area. If the specified heads are increased along the southern boundary to fit H-7 and USGS-1, the southern boundary converts from a discharge boundary to a recharge boundary. Recently, discussions on the Culebra have led toward considering this possibility. One problem, however, stems from the fact that the Pecos River, and the Malaga Bend region in particular, has been hypothesized to behave as a discharge region for regional flux from the Rustler (Mercer, 1983). While no absolute conclusions may be made yet concerning the direction of groundwater flow in the region south of the WIPP site, the results determined in this study have indicated that there is an inconsistency between the assumption that groundwater flows southward throughout the model domain and the observed heads in this area. Thus, a compromise between the fits at the southern boreholes and the rest of the model area was necessarily implemented through the boundary conditions.

4.4.3 Ensemble Groundwater Travel Times

The groundwater travel time from a point within the Culebra coincident with the centroid of the waste panels to the southern WIPP-site boundary was calculated for each of the calibrated CS fields. A common technique of expressing travel-time distributions is through a cumulative distribution function (cdf), which represents the probability of various travel times occurring. For instance, the travel time cdf determined from the calibrated fields (Figure 4-29) indicates that 90% of the travel times were longer than 12,000 yr, 50% of the travel times were longer than 18,000 yr, and 10% of the travel times were longer than 27,000 yr. The histogram shown in Figure 4-30 also conveys the distribution of groundwater travel times.

The travel paths that correspond to the travel times contained in the cdf are illustrated in Figure 4-31. Most of the travel paths follow a southeasterly direction until reaching the DOE-1 vicinity at which point the paths travel directly south to the WIPP-site boundary. A few paths travel directly south from the starting point while several others have a east-southeasterly direction prior to moving south toward the WIPP-site boundary.

Assuming the numerical model used to simulate a system properly accounts for the physics and scale of the problem of interest, the uncertainty of model results should decrease as the data set to which the model is conditioned increases. Conditioning a transmissivity field used in a model to observed steady-state pressure data reduces uncertainty in the transmissivity estimates away from the observed locations. Conditioning to transient-pressure data further reduces uncertainty in the transmissivity estimates between pressure-measurement locations due to the increase in information regarding the transmissive properties between these two locations. The reduction in the uncertainty of the travel time due to the conditioning of the Culebra model to the transient pressure data base is illustrated in Figure 4-32 where the cdf of travel times determined from the transient-calibrated model (referred to herein as the TCDF) and the cdf determined from the steady-state calibrated model (referred to herein as the SCDF) are shown. The cdf of the steady-state model was calculated by removing all the pilot points added during transient calibration from the input data sets of each of the realizations.

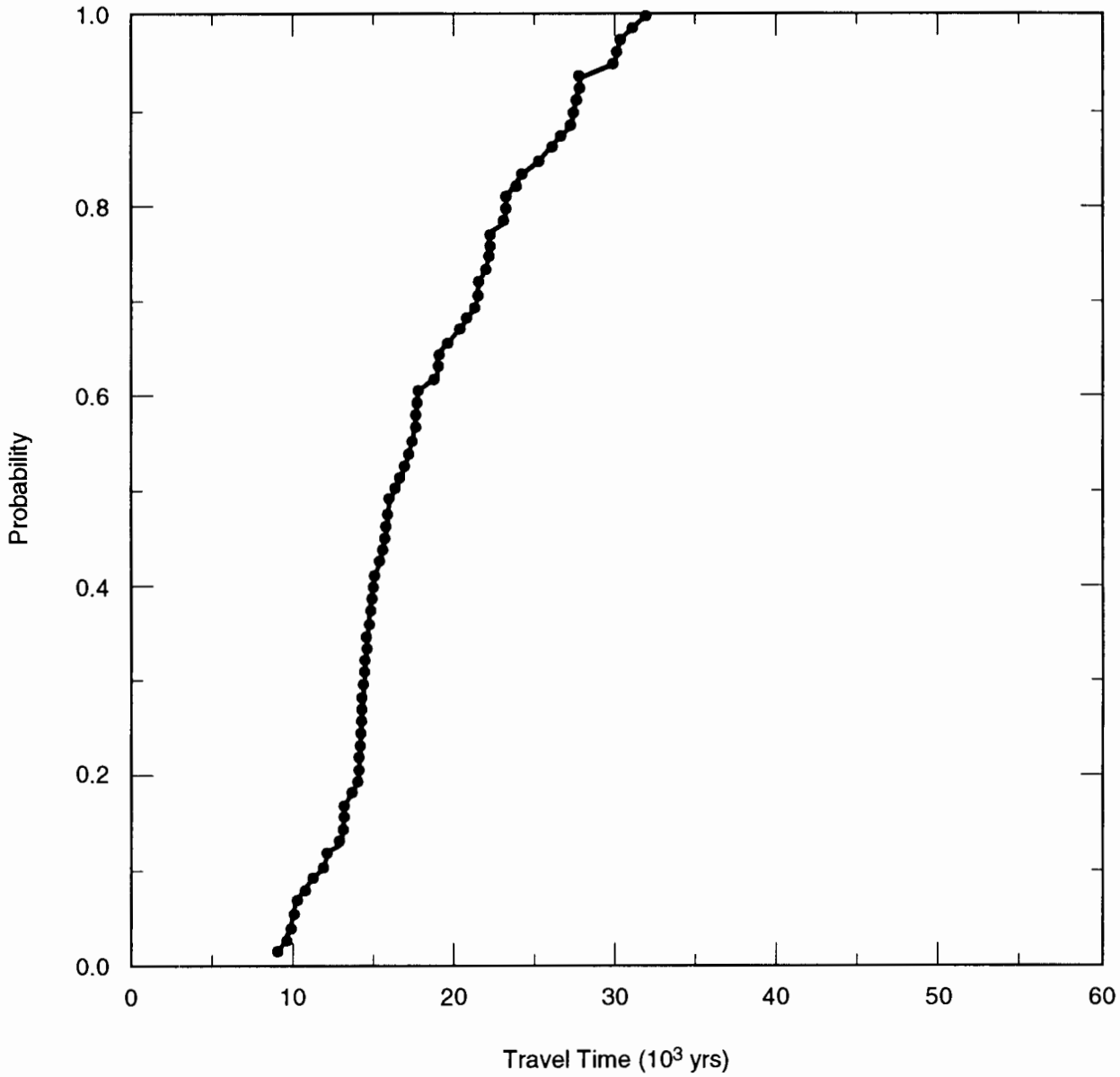

TRI-6342-3340-0

Figure 4-29. Travel time cumulative distribution function (cdf) determined from the 70 calibrated fields.

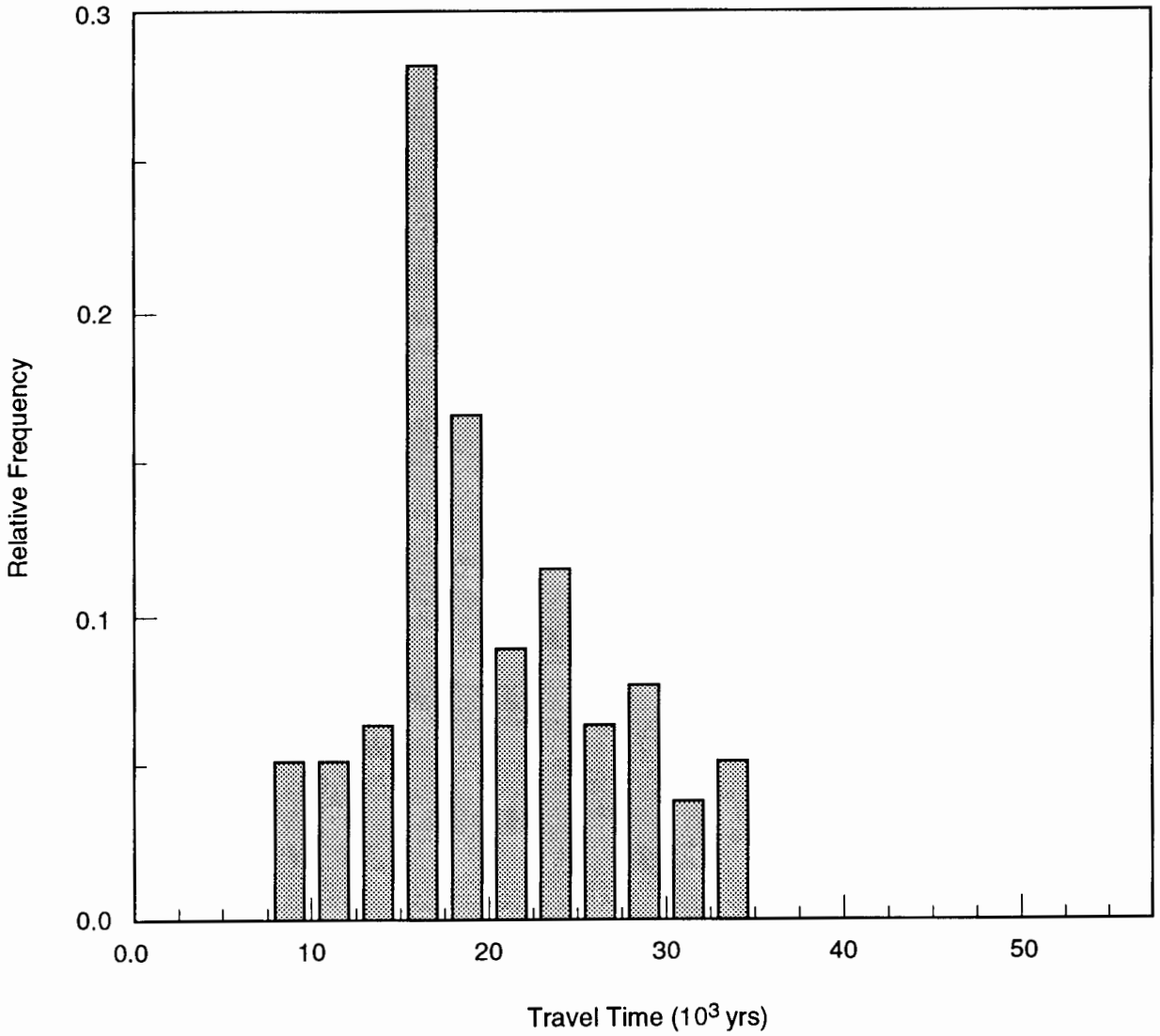

TRI-6342-3343-0

Figure 4-30. Histogram of travel times from ensemble of transient calibrated fields.

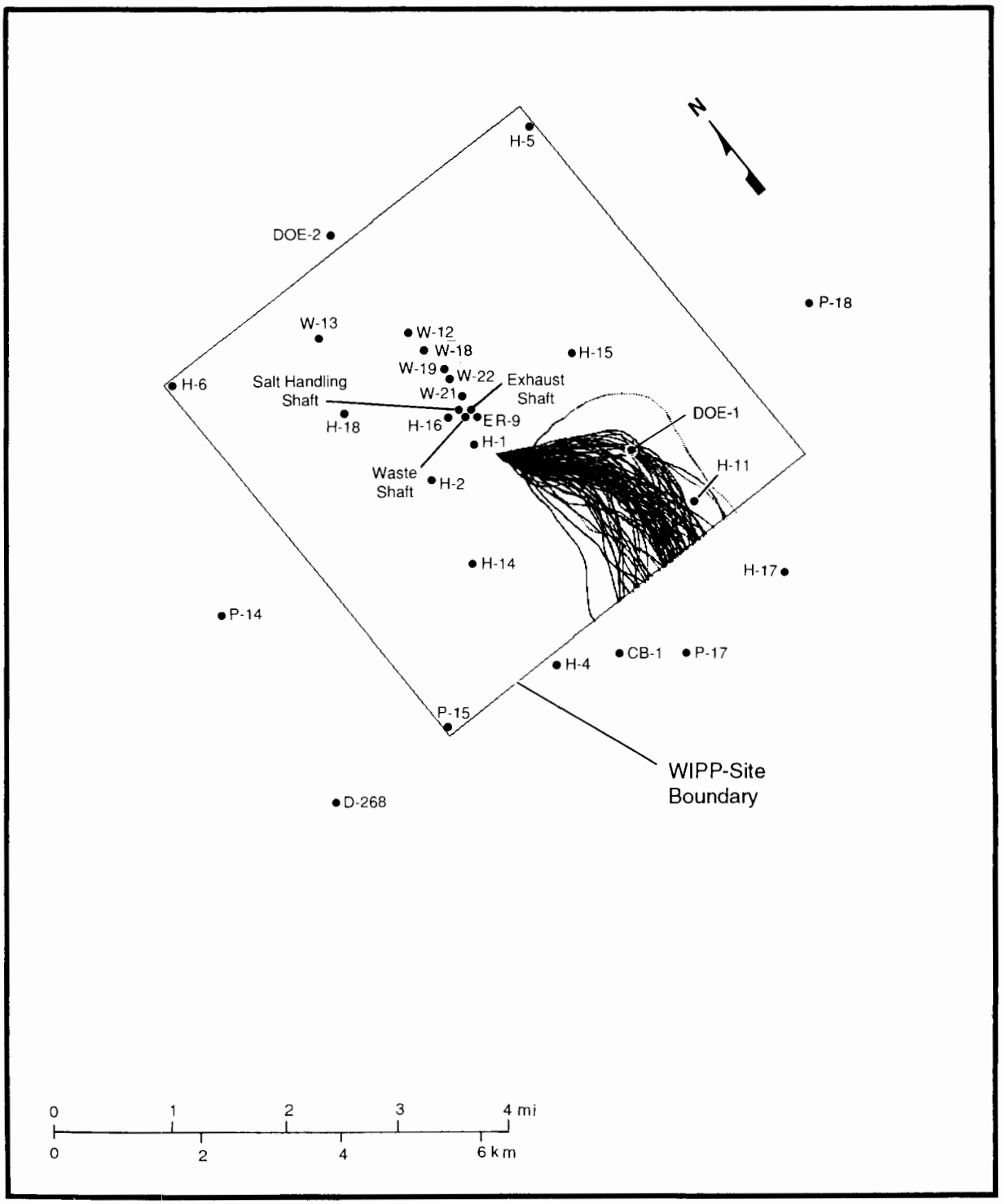

TRI-6342-3321-0

Figure 4-31. Travel paths corresponding to the travel times contained in the cumulative distribution function (cdf).

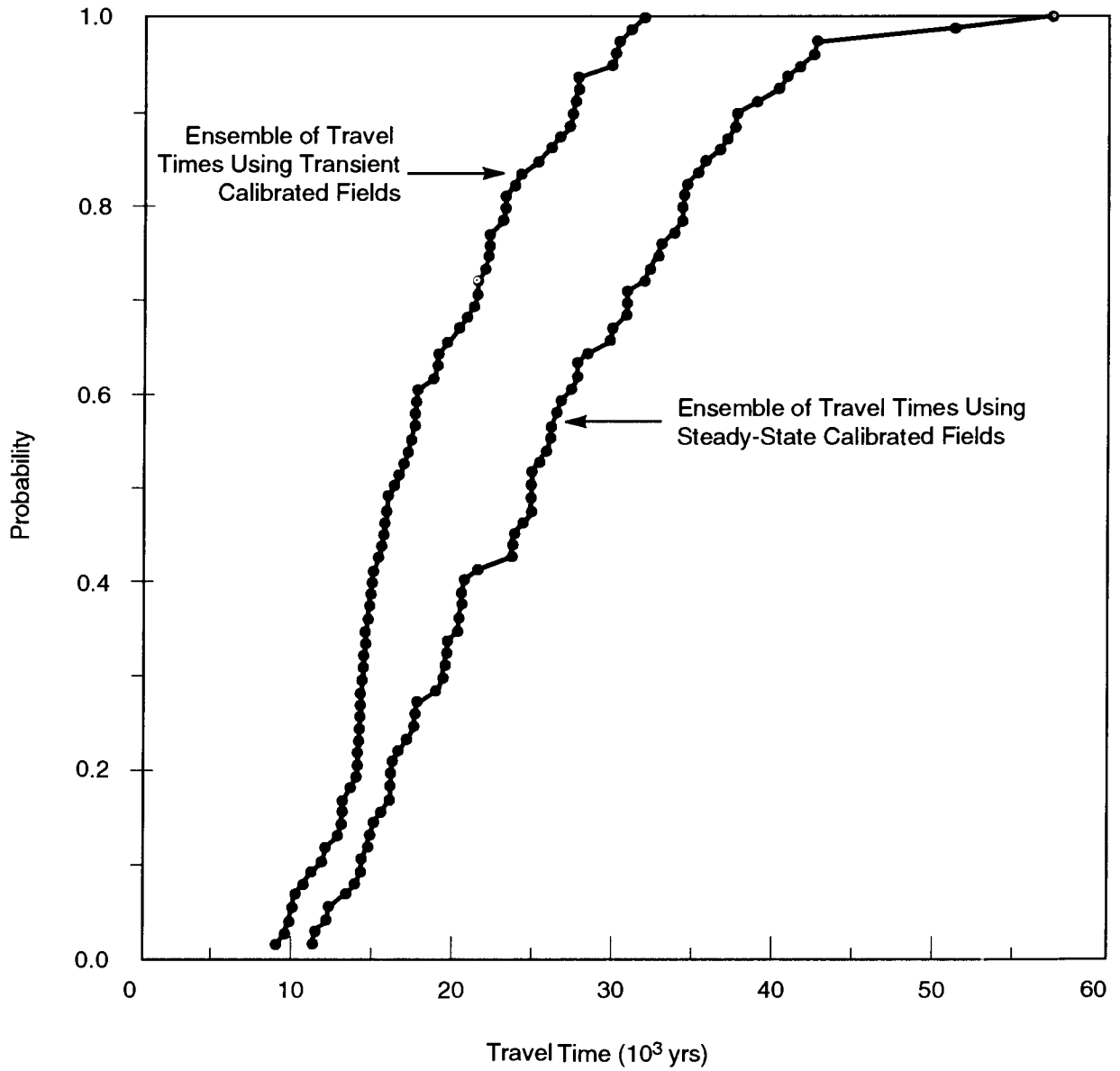

Figure 4-32. Cumulative distribution function (cdf) of travel times determined from the transient-calibrated fields (TCDF) and the cdf determined from the steady-state calibrated fields (SCDF).

As illustrated in Figure 4-32, the SCDF has a broader range of travel times than the TCDF. The minimum values between the two are approximately the same; however, the median and maximum travel times are quite different. As mentioned above, 50% of the travel times in the TCDF were greater than 18,000 yr and 10% were greater than 27,000 yr. In the SCDF, 50% of the travel times are greater than 25,000 yr and 10% are greater than 37,500 yr. The maximum travel times for the steady-state and transient-calibrated fields are 57,000 yr and 33,000 yr, respectively. The histogram of travel times using only the steady-state calculated models also illustrates this point (Figure 4-33).

Thus, the calibration to the transient-pressure data has significantly reduced the range of observed travel times. The extension of the high-transmissivity zone toward the H-15 borehole and the subsequent effect the extension has upon the reduction in travel distance from the starting point (i.e., a point coincident with the centroid of the waste panels in the Culebra) to a region of higher transmissivities has reduced the uncertainty in the travel times. The reduction in uncertainty occurs, as stated above, because of the modifications to the CS transmissivity fields in the southeastern region of the WIPP site, which are necessary to match the observed transient pressures in this region.

For comparison purposes, the travel paths that correspond to the travel times contained in the SCDF are illustrated in Figure 4-34. Like the travel paths shown in Figure 4-31, most of the travel paths follow a southeasterly direction until reaching the DOE-1 vicinity at which time the paths travel directly south to the WIPP-site boundary. A few more paths travel directly south from the starting point while several others have a east-southeasterly direction prior to moving south toward the WIPP-site boundary. In general though, the distribution of paths seems very similar to that illustrated in Figure 4-31.

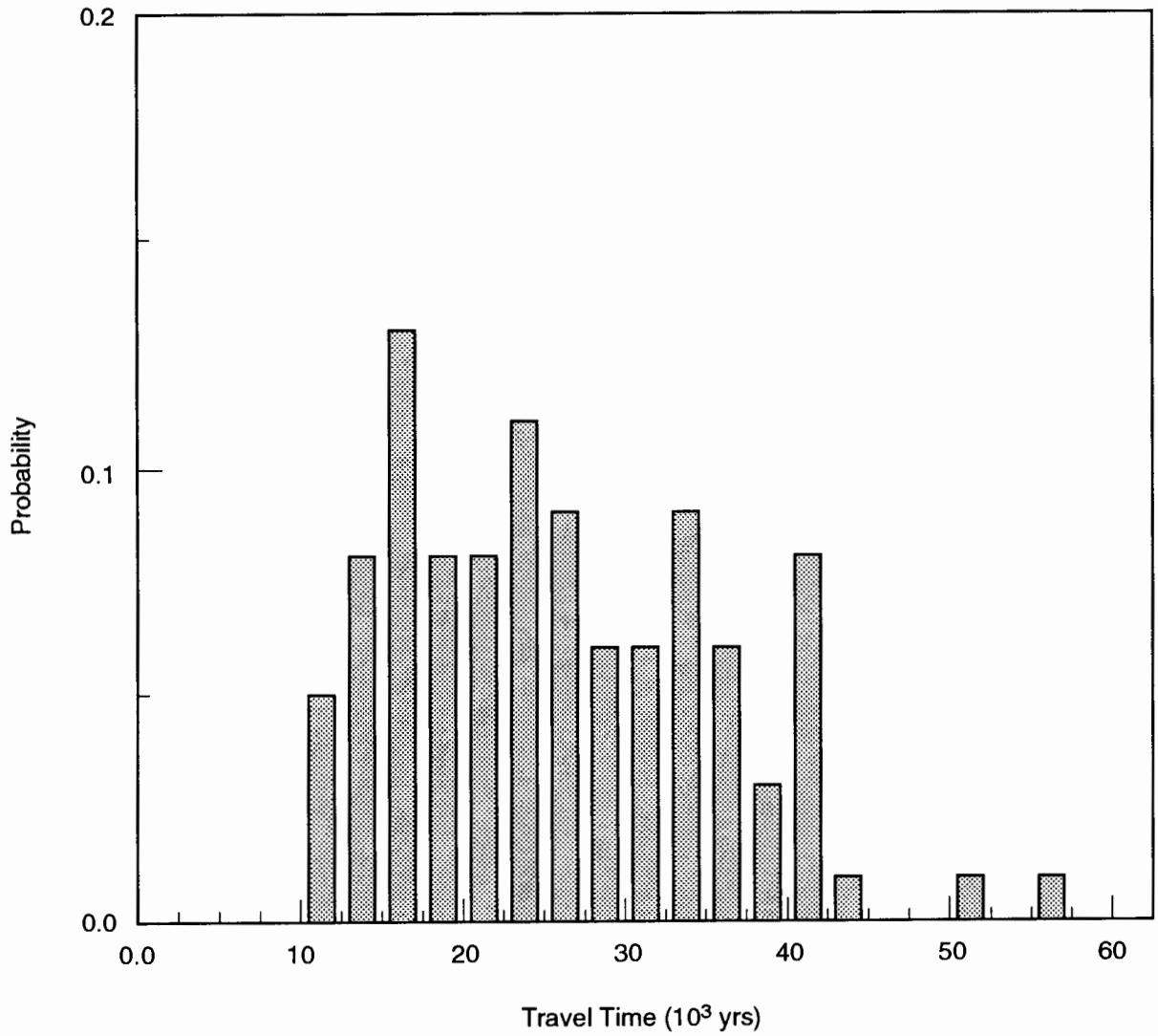

TRI-6342-3342-0

Figure 4-33. Histogram of travel times from ensemble of fields calibrated only to steady-state head data.

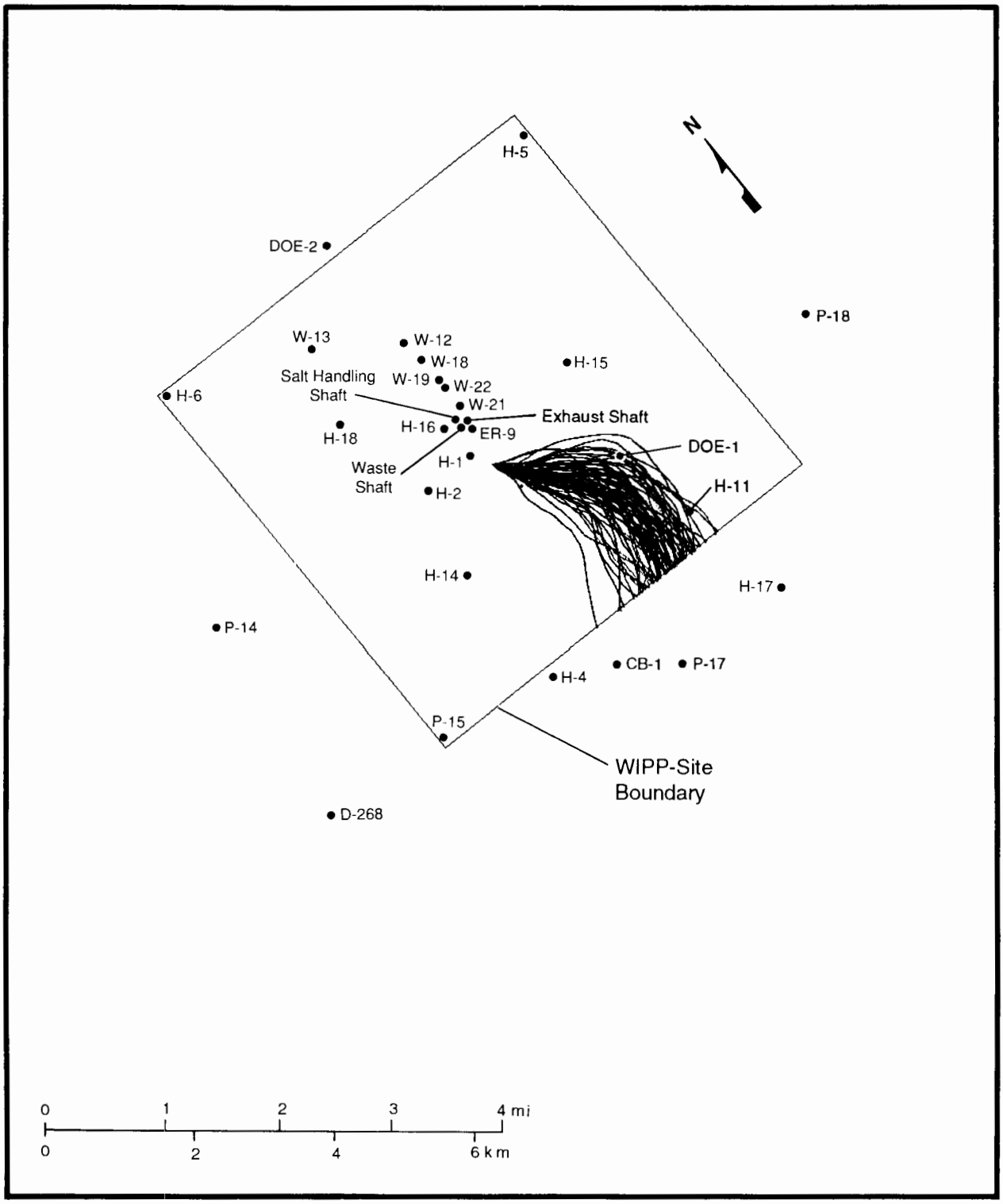

TRI-6342-3320-0

Figure 4-34. Travel paths associated with ensemble of transmissivity fields calibrated only to steady-state head data.

5. DISCUSSION

In the 1990 study, calibrating the transmissivity field to the transient pressures observed at the H-15 borehole from the H-11 pumping test reduced the travel time determined in the steady-state calibrated model by 30% and significantly altered the travel path due to the northern extension of the high-transmissivity zone toward the H-15 borehole. In this study, the fit to the H-15 response did not have as great an effect upon the travel time as noted in the 1990 study. Figure 5-1 illustrates this point. Each realization's goodness-of-fit to the H-15 drawdown (as expressed by the sum of the squared deviations of the calculated and observed pressures over the time of the H-11 pumping test) is plotted against its associated travel time. The travel times for the realizations that have low squared-deviation values (i.e., less than 1×10^{13} Pa^2) range from approximately 10,000 yr to 27,000 yr. Figure 5-1 also illustrates that although the fit to H-15's response may be poor, the travel time may be relatively short (e.g., 9500 yr).

Upon inspection, the primary factor that affects travel times is the distance that the particle must travel within a low-transmissivity region between the drop point and the southern WIPP-site boundary. In some realizations, the CS field has a low-transmissivity region ($\log_{10}$ T of -6.0 to -7.0) which extends southward from the WIPP-19, WIPP-21, and WIPP-22 boreholes to the H-1 borehole. The width and length of this low-transmissivity feature vary widely. In other realizations, this lower transmissivity feature is confined to the immediate vicinity of the WIPP wells and the transmissivities in the vicinity of the H-1 borehole lie between -5.0 and -6.0 $\log_{10}$ T. In these realizations, the travel times are smaller.

The secondary factor affecting the travel time is whether the particle intersects higher transmissivities (-4.0 to -5.0 $\log_{10}$ T) before exiting the southern WIPP-site boundary. In most of the realizations, the particles do eventually intersect a region of higher transmissivities. In some cases, the high-transmissivity region may begin adjacent to the H-3 borehole while, in others, the high-transmissivity region begins in the vicinity of the H-11 and DOE-1 boreholes.

Understanding the effect these two factors have on the value of the travel time helps to explain the lack of correlation observed in Figure 5-1. The fit to the H-15 response in and of itself is only of secondary importance. As described in Section 4.3, the transmissivities illustrated in Figure 4-23 depict an example of a realization in which the southern extension of low transmissivities (-6.0 to -7.0 $\log_{10}$ T) from the WIPP boreholes retard the groundwater from reaching the northern extension of the high-transmissivity zone. The particle must also travel through a region of transmissivities which range between -5.0 and -6.0 $\log_{10}$ T before entering higher transmissivities. A large percentage of the 21,500-yr travel time is associated with the first thousand meters traveled.

Figure 5-2 shows a transmissivity field that has an excellent fit to the steady-state and transient pressures. Although the southern extension of low transmissivities also exists, the distance between the lower transmissivities and the northern extension of the high-transmissivity zone is much smaller than in Figure 4-23. The reduced distance traveled before entering the higher transmissivities has reduced the travel time from 21,500 yr to 15,700 yr. To illustrate an extreme case, the travel time associated with the transmissivity field shown in Figure 5-3 is

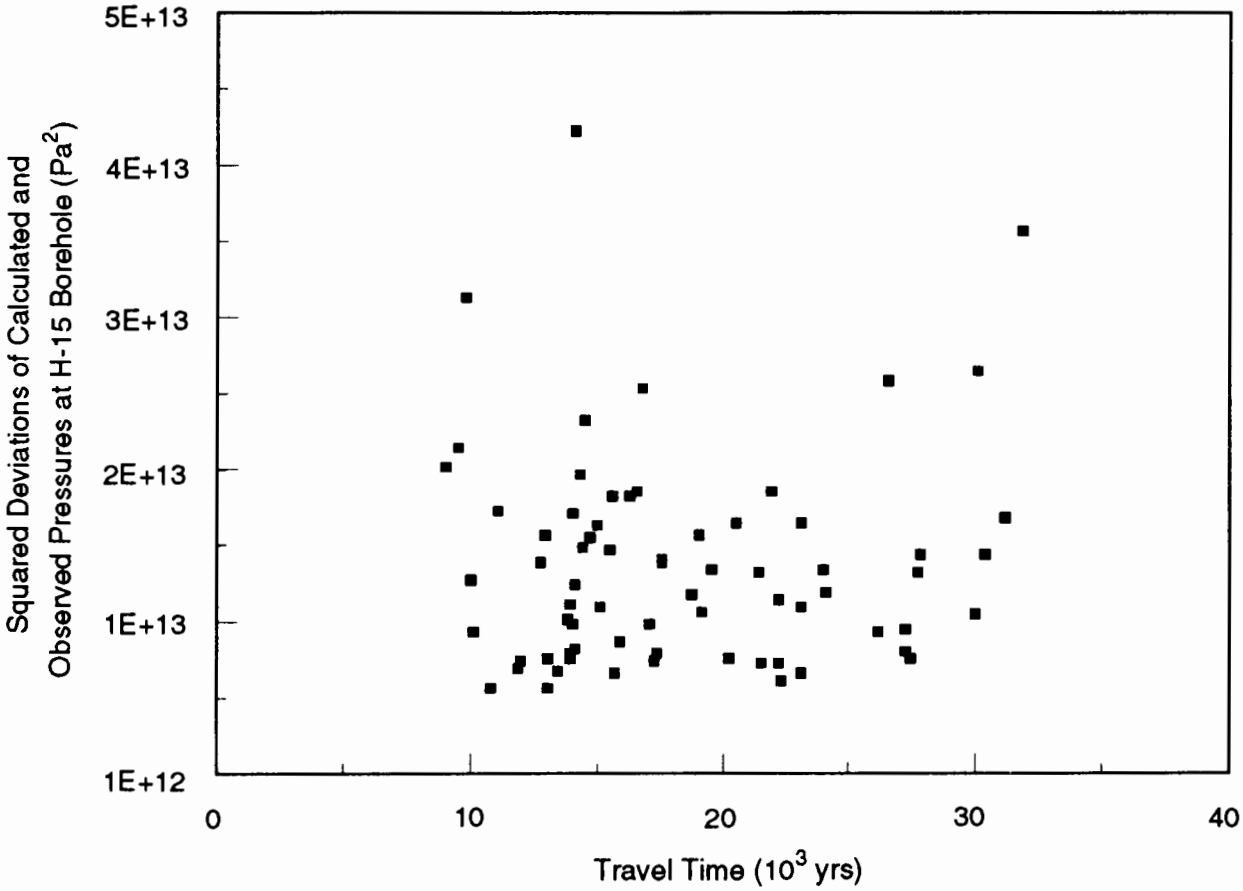

TRI-6342-3427-0

Figure 5-1. Scatterplot of goodness-of-fit of H-15 drawdown to travel times.

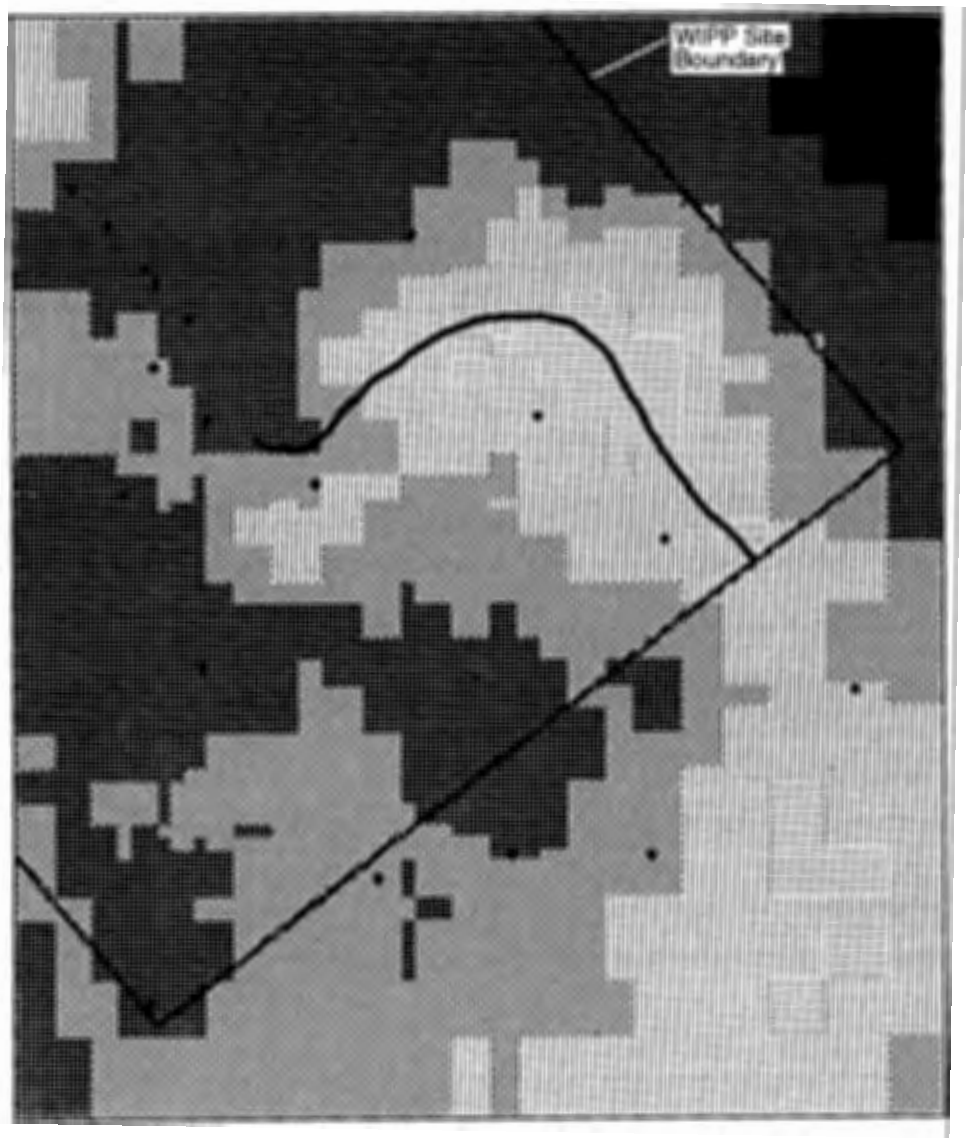

Values in $\log_{10}T(m^2/s)$

.. < -7.0	-7.0 to -6.0	-6.0 to -5.0
-5.0 to -4.0	-4.0 to -3.0	-3.0 to -2.0
-2.0 to -1.0	-1.0 < ..	

TRI-6342-3338-0

Figure 5-2. A transmissivity field that has an excellent fit to the steady-state and transient pressures and an associated groundwater travel time of 15,700 yr.

TRI-6342-3339-0

Figure 5-3. A transmissivity field that has a fair fit to the transient pressures and an associated groundwater travel time of 9900 yr.

approximately 9900 yr. While the fit to the transient data is considered fair, the fit to the H-15 drawdown is poor. However, it is worth noting the lack of a low-transmissivity (-7.0 to -6.0 $\log_{10}$ m^2/s) region in the vicinity of the drop point. The transmissivities between the drop point and the southern WIPP-site boundary range from -4.0 to -6.0 $\log_{10}$ T. If the differences between the calculated and observed drawdown at the H-15 borehole were reduced, the transmissivities would likely increase between H-1 and the southern WIPP-site boundary and the travel time would be further reduced.

An attempt to clarify the impact of the low-transmissivity region in the vicinity of the H-1 borehole on travel time is presented in Figures 5-4 and 5-5. Figure 5-4 contains a histogram of the distances traveled by each of the 70 particles to the southern WIPP-site boundary. Most of the travel distances are between 3000 and 4000 m. If the harmonic mean of a transmissivity field is calculated over the first 2000 m of the travel path and plotted against its associated travel time, a general inverse correlation between the two is observed (Figure 5-5).

Because lower transmissivities have a greater effect upon the harmonic mean value than higher transmissivities, the fields with lower transmissivities in the H-1 area should generally produce lower harmonic mean values and longer travel times. Scatterplots similar to that illustrated in Figure 5-5 were also produced for travel distances of 500 m and 1000 m. In these figures, however, a trend was less easily observed than the trend seen in Figure 5-5. The difference is due to the fact that at 2000 m, the particle has traveled far enough to exit the low-transmissivity region and potentially enter the high-transmissivity zone. As mentioned above, the low-transmissivity region has the primary effect upon travel time; the transmissivities encountered by the particle once it has exited the low-transmissivity region are of secondary importance.

From this study, the importance of understanding the location of the lower transmissivity region in the vicinity of the H-1 area is clear. The uncertainty of the transmissivities in this region has been shown to affect the overall travel time distribution significantly. In addition, if the high-transmissivity region exists in reality as a fracture zone with significantly higher transmissivities than represented in the CS field, the lower transmissivities would have the controlling effect upon the actual travel time to the southern WIPP-site boundary.

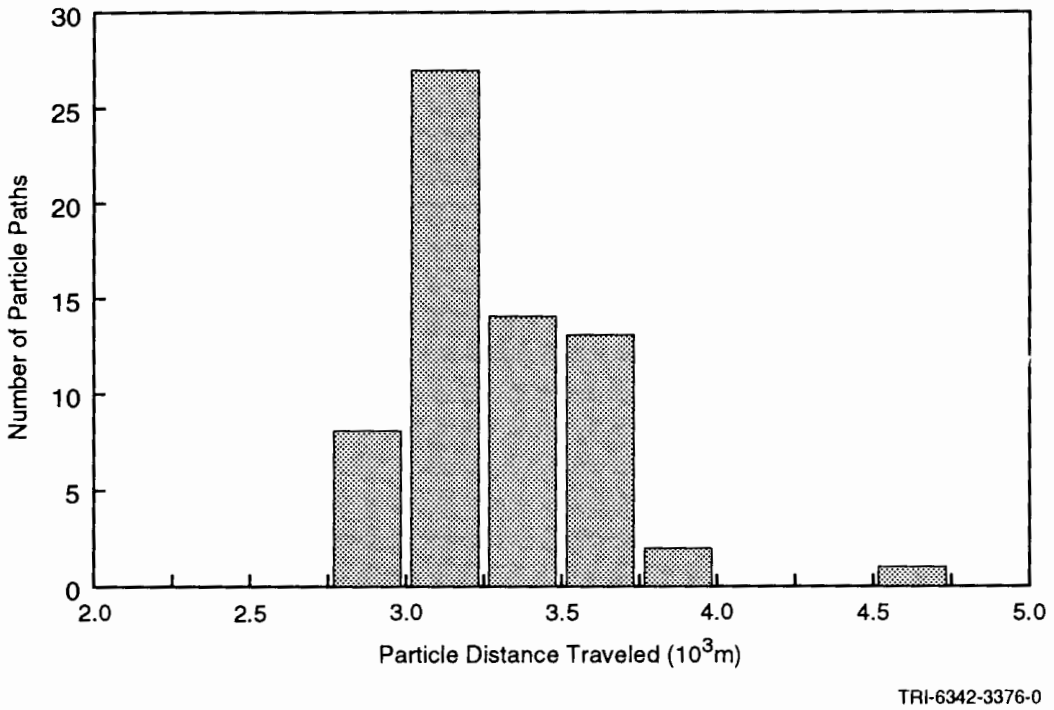

Figure 5-4. Histogram of groundwater particle distance traveled to southern WIPP-site boundary for the ensemble of calibrated fields.

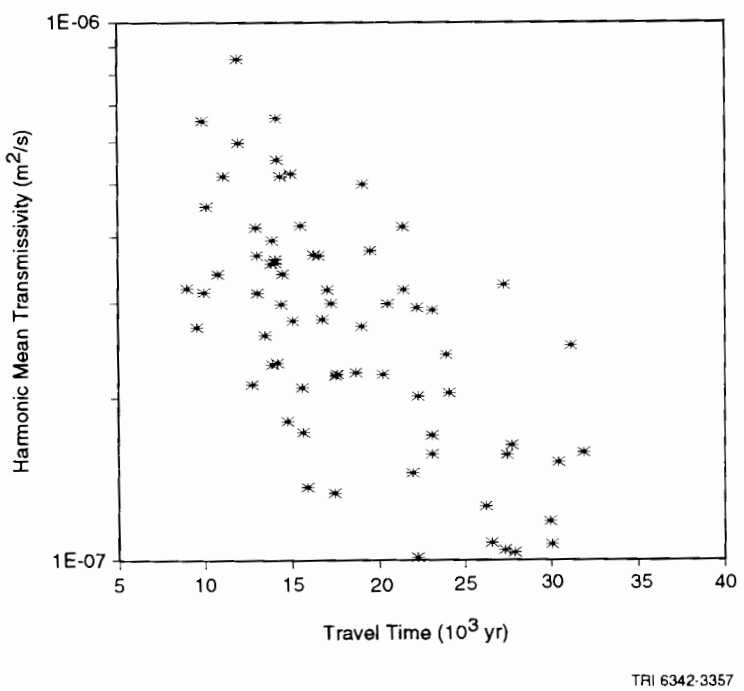

Figure 5-5. Scatterplot of harmonic-mean transmissivity over first 2000 m of flow path for ensemble of fields vs. associated groundwater travel time.

6. CONCLUSIONS

In this study, an automated approach to solving the inverse problem was utilized to calibrate 70 transmissivity fields to the exhaustive data base of measured heads taken within the Culebra Dolomite Member. The GRASP-INV code, employed during this study, produced conditionally simulated (CS) transmissivity fields and subsequently calibrated them using the pilot-point technique. Pilot points are calibration points within the model domain that are assigned synthetic transmissivity values. The pilot-point location and value are determined through adjoint sensitivity and optimization techniques, respectively.

In an earlier study (LaVenue et al., 1990), a wide high-transmissivity zone was assigned to match the observed pressures at H-15 during the H-11 pumping test. This high-transmissivity feature, which was not unique in orientation, width, or transmissivity magnitude, extended northward from P-17 to H-15. Given the uncertainty in the high-transmissivity feature, a large number of different representations of the high-transmissivity zone could be possible, and thus, the actual transmissivity zone could be significantly different from the representation in the 1990 model domain.

An attempt was made in this study to assess the plausible variations in the high-transmissivity zone. The uncertainty associated with the Culebra transmissivity field, as expressed through the kriging estimate's (μ) standard error (σ), provided one way to assess the possible spatial variability in this region through the analysis of numerous realizations. The distribution of possible values at a given point within which a CS value should lie is expressed by $\mu \pm 3\sigma$. This distribution was narrower near measured transmissivity locations and wider away from transmissivity observations. By generating and subsequently calibrating numerous transmissivity fields with values within the $\mu \pm 3\sigma$ distribution, the range of plausible fields and the spatial variability associated with these fields was determined.

Once the calibrated fields were produced, groundwater travel times from a point within the Culebra, coincident with the center of the waste panels, to the southern WIPP-site boundary were calculated. From this distribution of travel times, the most important spatial features controlling groundwater flow were determined to be

1. The southern and eastern extension of lower transmissivities from the vicinity of the H-1 and WIPP-21 boreholes toward the H-3 borehole.

2. The northern and western extension of the high-transmissivity zone from the vicinity of the H-11 and DOE-1 boreholes toward the H-15 and H-3 boreholes.

These results indicate that additional data in the region east and north of the H-3 borehole could benefit future modeling studies by reducing some of the questions concerning the spatial variability within this region.

REFERENCES

Barr, G.E., W.B. Miller, and D.D. Gonzalez. 1983. *Interim Report on the Modeling of the Regional Hydraulics of the Rustler Formation.* SAND83-0391. Albuquerque, NM: Sandia National Laboratories.

Beauheim, R.L. 1986. *Hydraulic-Test Interpretations for Well DOE-2 at the Waste Isolation Pilot Plant (WIPP) Site.* SAND86-1364. Albuquerque, NM: Sandia National Laboratories.

Beauheim, R.L. 1987a. *Analysis of Pumping Tests of the Culebra Dolomite Conducted at the H-3 Hydropad at the Waste Isolation Pilot Plant (WIPP) Site.* SAND86-2311. Albuquerque, NM: Sandia National Laboratories.

Beauheim, R.L. 1987b. *Interpretation of the WIPP-13 Multipad Pumping Test of the Culebra Dolomite at the Waste Isolation Pilot Plant (WIPP) Site.* SAND87-2456. Albuquerque, NM: Sandia National Laboratories.

Beauheim, R.L. 1987c. *Interpretations of Single-Well Hydraulic Tests Conducted At and Near the Waste Isolation Pilot Plant (WIPP) Site, 1983-1987.* SAND87-0039. Albuquerque, NM: Sandia National Laboratories.

Beauheim, R.L. 1988. "Scale Effects in Well Testing in Fractured Media," *Proceedings Fourth Canadian/American Conference on Hydrogeology: Fluid Flow, Heat Transfer and Mass Transport in Fractured Rocks, Banff, Alberta, Canada, June 21-24, 1988.* Eds. B. Hitchon and S. Bachu. SAND87-1955. Dublin, OH: National Water Well Association. Vol. 4, 152-159.

Beauheim, R.L. 1989. *Interpretation of H-11b4 Hydraulic Tests and the H-11 Multipad Pumping Test of the Culebra Dolomite at the Waste Isolation Pilot Plant (WIPP) Site.* SAND89-0536. Albuquerque, NM: Sandia National Laboratories.

Bellman, R.E. 1957. *Dynamic Programming.* Princeton, NJ: Princeton University Press.

Bertram-Howery, S.G., M.G. Marietta, R.P. Rechard, P.N. Swift, D.R. Anderson, B.L. Baker, J.E. Bean, Jr., W. Beyeler, K.F. Brinster, R.V. Guzowski, J.C. Helton, R.D. McCurley, D.K. Rudeen, J.D. Schreiber, and P. Vaughn. 1990. *Preliminary Comparison with 40 CFR Part 191, Subpart B for the Waste Isolation Pilot Plant, December 1990.* SAND90-2347. Albuquerque, NM: Sandia National Laboratories.

Carrera, J., and S.P. Neuman. 1986. "Estimation of Aquifer Parameters Under Transient and Steady State Conditions: 2. Uniqueness, Stability, and Solution Algorithms," *Water Resources Research.* Vol. 22, no. 2, 211-227.

Cauffman, T.L., A.M. LaVenue, and J.P. McCord. 1990. *Ground-Water Flow Modeling of the Culebra Dolomite. Volume II: Data Base.* SAND89-7068/2. Albuquerque, NM: Sandia National Laboratories.

Cole, C.R., and F.W. Bond. 1980. *Assessment of Effectiveness of Geologic Isolation Systems: Comparison of INTERA and WISAP Consequence Model Application.* PNL-3070. Richland, VA: Pacific Northwest Laboratory.

D'Appolonia Consulting Engineers, Inc. 1981. *Modeling Verification Studies: Long-Term Waste Isolation Assessment, Waste Isolation Pilot Plant (WIPP Project), Southeastern New Mexico.* Report prepared for Westinghouse Electric Corporation under contract to U.S. Department of Energy.

Davies, P.B. 1989. *Variable-Density Ground-Water Flow and Paleohydrology in the Waste Isolation Pilot Plant (WIPP) Region, Southeastern New Mexico.* Open File Report 88-490. Albuquerque, NM: U.S. Geological Survey, Dept. of the Interior.

Delfiner, P. 1976. "Linear Estimation of Non Stationary Spatial Phenomena," *Advanced Geostatistics in the Mining Industry, Proceedings of the NATO Advanced Study Institute, University of Rome, October 13-25, 1975.* Eds. M. Guarascio, M. David, and C. Huijbregts. Hingham, MA: D. Reidel Pub. Co. 49-68.

Delhomme, J.P. 1979. "Spatial Variability and Uncertainty in Groundwater Flow Parameters: A Geostatistical Approach," *Water Resources Research.* Vol. 15, no. 2, 269-280.

EPA (Environmental Protection Agency). 1985. "40 CFR Part 191: Environmental Standards for the Management and Disposal of Spent Nuclear Fuel, High-Level and Transuranic Radioactive Wastes," *Federal Register.* Vol. 50, no. 182, 38066-38089.

Gill, P.E., W. Murray, and M.H. Wright. 1981. *Practical Optimization.* New York, NY: Academic Press, Inc.

Haug, A., V.A. Kelley, A.M. LaVenue, and J.F. Pickens. 1987. *Modeling of Ground-Water Flow in the Culebra Dolomite at the Waste Isolation Pilot Plant (WIPP) Site: Interim Report.* Contractor Report SAND86-7167. Albuquerque, NM: Sandia National Laboratories.

INTERA, Inc. 1989. *Users Manual for STLINE.* [Austin, TX:] INTERA, Inc. (Copy on file at the Waste Management and Transportation Library, Sandia National Laboratories, Albuquerque, NM.)

Journel, A.G., and Ch.J. Huijbregts. 1978. *Mining Geostatistics.* New York, NY: Academic Press.

Kafritsas, J., and R.L. Bras. 1981. *The Practice of Kriging.* Technical Report 263. Cambridge, MA: Massachusetts Institute of Technology, Ralph M. Parsons Laboratory.

Lappin, A.R. 1988. *Summary of Site-Characterization Studies Conducted From 1983 Through 1987 at the Waste Isolation Pilot Plant (WIPP) Site, Southeastern New Mexico.* SAND88-0157. Albuquerque, NM: Sandia National Laboratories.

Lappin, A.R., R.L. Hunter, D.P. Garber, and P.B. Davies, eds. 1989. *Systems Analysis, Long-Term Radionuclide Transport, and Dose Assessments, Waste Isolation Pilot Plant (WIPP), Southeastern New Mexico; March 1989.* SAND89-0462. Albuquerque, NM: Sandia National Laboratories.

LaVenue, A.M., A. Haug, and V.A. Kelley. 1988. *Numerical Simulation of Ground-Water Flow in the Culebra Dolomite at the Waste Isolation Pilot Plant (WIPP) Site: Second Interim Report.* SAND88-7002. Albuquerque, NM: Sandia National Laboratories.

LaVenue, A.M., T.L. Cauffman, and J.F. Pickens. 1990. *Ground-Water Flow Modeling of the Culebra Dolomite. Volume I: Model Calibration.* SAND89-7068/1. Albuquerque, NM: Sandia National Laboratories.

Luenberger, D.G. 1973. *Introduction to Linear and Nonlinear Programming.* Reading, MA: Addison-Wesley Publishing Co.

Mantoglou, A., and J.L. Wilson. 1981. *Simulation of Random Fields with the Turning Bands Method.* Report 264. Cambridge, MA: Ralph M. Parsons Laboratory, Department of Civil Engineering, Massachusetts Institute of Technology.

Mantoglou, A., and J.L. Wilson. 1982. "The Turning Bands Method for Simulation of Random Fields Using Line Generation by a Spectral Method," *Water Resources Research*. Vol. 18, no. 5, 1379-1394.

Marsily, G. de. 1986. *Quantitative Hydrogeology: Groundwater Hydrology for Engineers.* Orlando, FL: Academic Press, Inc.

Marsily, G. de, G. Lavedan, M. Boucher, and G. Fasanino. 1984. "Interpretation of Interference Tests in a Well Field Using Geostatistical Techniques To Fit the Permeability Distribution in a Reservoir Model," *Second NATO Advanced Study Institute, GEOSTAT 1983 - Tahoe, CA, Proceedings of the Geostatistics for Natural Resources Characterization, September 6-17, 1983.* Eds. G. Verly, M. David, A.G. Journel, and A. Marechai. Hingham, MA: D. Reidel Pub. Co. 831-849.

Matheron, G. 1971. *The Theory of Regionalized Variables and its Applications.* Paris, France: École National Supérieure des Mines.

Matheron, G. 1973. "The Intrinsic Random Functions and Their Applications," *Advances in Applied Probability.* Vol. 5, no. 3, 439-468.

Mejia, J. M., and I. Rodríguez-Iturbe. 1974. "On the Synthesis of Random Field Sampling from the Spectrum: An Application to the Generation of Hydrologic Spatial Processes," *Water Resources Research*. Vol. 10, no. 4, 705-711.

Mercer, J.W. 1983. *Geohydrology of the Proposed Waste Isolation Pilot Plant Site, Los Medaños Area, Southeastern New Mexico.* U.S. Geological Survey Water-Resources Investigations 83-4016. Albuquerque, NM: U.S. Geological Survey.

Niou, S., and J. Pietz. 1987. *A Statistical Inverse Analysis of the H-3 Multipad Pumping Test.* Report prepared by IT Corporation, Inc. for Westinghouse Electric Corporation.

Powers, D.W., S.J. Lambert, S-E. Shaffer, L.R. Hill, and W.D. Weart, eds. 1978. *Geological Characterization Report, Waste Isolation Pilot Plant (WIPP) Site, Southeastern New Mexico.* SAND78-1596. Albuquerque, NM: Sandia National Laboratories. Vols. 1 - 2.

RamaRao, B.S., and M. Reeves. 1990. *Theory and Verification for the GRASP II Code for Adjoint-Sensitivity Analysis of Steady-State and Transient Ground-Water Flow.* SAND89-7143. Albuquerque, NM: Sandia National Laboratories.

Reeves, M., D.S. Ward, N.D. Johns, and R.M. Cranwell. 1986a. *Theory and Implementation for SWIFT II, The Sandia Waste-Isolation Flow and Transport Model for Fractured Media, Release 4.84.* SAND83-1159; NUREG/CR-3328. Albuquerque, NM: Sandia National Laboratories.

Reeves, M., D.S. Ward, N.D. Johns, and R.M. Cranwell. 1986b. *Data Input Guide for SWIFT II, The Sandia Waste-Isolation Flow and Transport Model for Fractured Media, Release 4.84.* SAND83-0242; NUREG/CR-3162. Albuquerque, NM: Sandia National Laboratories.

Reeves, M., D.S. Ward, P.A. Davis, and E.J. Bonano. 1986c. *Swift II Self-Teaching Curriculum: Illustrative Problems for the Sandia Waste-Isolation Flow and Transport Model for Fractured Media.* SAND84-1586; NUREG/CR-3925. Albuquerque, NM: Sandia National Laboratories.

Sandia WIPP Project. 1992. *Preliminary Performance Assessment for the Waste Isolation Pilot Plant, December 1992, Vol. 3.* SAND92-0700/3. Albuquerque, NM: Sandia National Laboratories.

Saulnier, G.J., Jr. 1987. *Analysis of Pumping Tests of the Culebra Dolomite Conducted at the H-11 Hydropad at the Waste Isolation Pilot Plant (WIPP) Site.* SAND87-7124. Albuquerque, NM: Sandia National Laboratories.

Shinozuka, M., and C.-M. Jan. 1972. "Digital Simulation of Random Processes and Its Applications," *Journal of Sound and Vibration.* Vol. 25, no. 1, 111-128.

Smith, L., and R.A. Freeze. 1979. "Stochastic Analysis of Steady State Groundwater Flow in a Bounded Domain: 2. Two-Dimensional Simulations," *Water Resources Research.* Vol, 15, no. 6, 1543-1559.

Smith, L., and F.W. Schwartz. 1981. "Mass Transport. 2. Analysis of Uncertainty in Prediction," *Water Resources Research.* Vol. 17, no. 2, 351-369.

U.S. Department of Energy. 1980a. *Final Environmental Impact Statement, Waste Isolation Pilot Plant.* DOE/EIS-0026. Washington, D.C.: U.S. Department of Energy. Vol. 2.

U.S. Department of Energy. 1980b. *Waste Isolation Pilot Plant, Safety Analysis Report.* [Washington, D.C.: U.S. Department of Energy.] Vols. 1-5.

Wilson, J.L. 1979. "The Synthetic Generation of Areal Averages of a Random Field," *Socorro Workshop on Stochastic Methods in Subsurface Hydrology, Socorro, NM, April 26-27, 1979.* (Copy on file at the Waste Management and Transportation Library, Sandia National Laboratories, Albuquerque, NM.)

Wilson, J.L., B.S. RamaRao, and J.A. McNeish. 1986. *GRASP: A Computer Code to Perform Post-SWENT Adjoint Sensitivity Analysis of Steady-State Ground-Water Flow.* BMI/ONWI-625. Columbus, OH: Prepared for Office of Nuclear Waste Isolation, Battelle Memorial Institute.

WIPP PA (Performance Assessment) Division. 1991. *Preliminary Comparison with 40 CFR Part 191, Subpart B for the Waste Isolation Pilot Plant, December 1991. Volume 3: Reference Data.* SAND91-0893/3. Albuquerque, NM: Sandia National Laboratories.

WIPP PA (Performance Assessment) Department. 1992. *Preliminary Performance Assessment for the Waste Isolation Pilot Plant, December 1992, Vols. 1-2.* SAND92-0700. Albuquerque, NM: Sandia National Laboratories.

Zimmerman, D.A., and J.L. Wilson. 1990. *Description of and User's Manual for TUBA: A Computer Code for Generating Two-Dimensional Random Fields via the Turning Bands Method.* Albuquerque, NM: SeaSoft Scientific and Engineering Analysis Software. (Copy on file at the Waste Management and Transportation Library, Sandia National Laboratories, Albuquerque, NM.)

NOMENCLATURE

b	=	thickness of the grid block
$\underline{\underline{B}}$	=	transformation matrix
$\underline{\underline{C}}$	=	conductance matrix
$\underline{d}$	=	direction vector
$\underline{e}_p$	=	$\{\underline{p}(k) - p_{ob}(K)\}$
$\underline{e}_u$	=	$\{\underline{u} - \underline{u}_{est}\}$
$\underline{f}$	=	vector of source terms
g	=	acceleration due to gravity
$\underline{g}$	=	gradient vector
J	=	weighted least squares (WLS) error criterion function
k	=	time step number
K	=	permeability
K^*	=	estimated permeability
$k_1(r)$	=	generalized covariance function for a line (IRF-0) process
$k_2(r)$	=	generalized covariance function for a two dimensional (IRF-0) process
L	=	maximum time level of the simulation
L	=	number of lines used in Turning Bands Method
L	=	total number of time steps
m	=	suffix denoting grid block
M	=	number of grid blocks
n	=	time level (1,2,3...L)
N	=	number of pilot points
$\underline{\underline{P}}$	=	posterior covariance matrix of errors in parameters
$P_{ob(k)}$	=	pressures observed
$p(k)$	=	pressures computed
$\underline{\underline{R}}$	=	Cov. matrix of errors in $\underline{P}_{ob}$
$\underline{\underline{S}}$	=	storativity matrix
$\underline{\underline{S}}$	=	Jacobian Matrix (of sensitivities)
t	=	time
T	=	transmissivity
T^*	=	estimated transmissivity
T_p	=	pilot-point transmissivity
$\underline{u}$	=	vector of parameters ($Y_p = \mathrm{Log}_{10}\, T_p$)

$\underline{\underline{U}}$	=	Cov. matrix of errors in $\underline{u}$
W	=	Weiner-Levy Process
Y_p	=	$\mathrm{Log}_{10}\, T_p$
Z	=	a true (but unknown) field
Z_{ok}	=	kriged field using the 'measured' data
Z_{uc}	=	unconditional simulated field
Z_{uk}	=	kriged field using simulated data at the measurement
η	=	relative weight of the plausibility criterion to model fit criterion
ρ	=	density of fluid
μ	=	viscosity of fluid
$\underline{\lambda}$	=	adjoint state-vector
β	=	step length
γ	=	kriging weight
σ	=	standard deviation
ξ	=	spatial coordinate along a turning band line
Δt	=	$t^n - t^{n-1}$

PERFORMANCE ASSESSMENT DISTRIBUTION LIST

(Send Distribution list changes to M.M. Gruebel, Dept. 6342, Sandia National Laboratories, PO Box 5800, Albuquerque, NM 87185-5800)

Federal Agencies

US Department of Energy (2)
Office of Environmental Restoration
and Waste Management
Attn: L.P. Duffy, EM-1
C. Frank, EM-50
Washington, DC 20585

US Department of Energy (3)
Office of Environmental Restoration
and Waste Management
Attn: M. Frei, EM-34 (Trevion II)
Director, Waste Management Projects
Washington, DC 20585-0002

US Department of Energy
Office of Environmental Restoration
and Waste Management
Attn: J. Lytle, EM-30 (Trevion II)
Washington, DC 20585-0002

US Department of Energy
Office of Environmental Restoration
and Waste Management
Attn: S. Schneider, EM-342
(Trevion II)
Washington, DC 20585-0002

US Department of Energy (3)
WIPP Task Force
Attn: G.H. Daly
S. Fucigna
B. Bower
12800 Middlebrook Rd.
Suite 400
Germantown, MD 20874

US Department of Energy (4)
Office of Environment, Safety and
Health
Attn: R.P. Berube, EH-20
C. Borgstrum, EH-25
R. Pelletier, EH-231
K. Taimi, EH-232
Washington, DC 20585

US Department of Energy (5)
WIPP Project Integration Office
Attn: W.J. Arthur III
R. Becker
P. Dickman
L.W. Gage
P.J. Higgins
D.A. Olona
PO Box 5400
Albuquerque, NM 87115-5400

US Department of Energy (10)
WIPP Project Site Office (Carlsbad)
Attn: A. Hunt (4)
V. Daub (4)
J. Lippis
K. Hunter
PO Box 3090
Carlsbad, NM 88221-3090

US Department of Energy, (5)
Office of Civilian Radioactive Waste
Management
Attn: Deputy Director, RW-2
Associate Director, RW-10
Office of Program
Administration and
Resources Management
Associate Director, RW-20
Office of Facilities
Siting and Development
Associate Director, RW-30
Office of Systems
Integration and
Regulations
Associate Director, RW-40
Office of External
Relations and Policy
Office of Geologic Repositories
Forrestal Building
Washington, DC 20585

US Department of Energy
Attn: National Atomic Museum Library
Albuquerque Operations Office
PO Box 5400
Albuquerque, NM 87185

US Department of Energy
Research & Waste Management Division
Attn: Director
PO Box E
Oak Ridge, TN 37831

US Department of Energy (2)
Idaho Operations Office
Fuel Processing and Waste
Management Division
785 DOE Place
Idaho Falls, ID 83402

US Department of Energy
Savannah River Operations Office
Defense Waste Processing
Facility Project Office
Attn: W.D. Pearson
PO Box A
Aiken, SC 29802

US Department of Energy (2)
Richland Operations Office
Nuclear Fuel Cycle & Production
Division
Attn: R.E. Gerton
825 Jadwin Ave.
PO Box 500
Richland, WA 99352

US Department of Energy (3)
Nevada Operations Office
Attn: J.R. Boland
D. Livingston
P.K. Fitzsimmons
2753 S. Highland Drive
Las Vegas, NV 89183-8518

US Department of Energy (2)
Technical Information Center
PO Box 62
Oak Ridge, TN 37831

US Department of Energy (2)
Chicago Operations Office
Attn: J.C. Haugen
9800 South Cass Avenue
Argonne, IL 60439

US Department of Energy
Los Alamos Area Office
528 35th Street
Los Alamos, NM 87544

US Department of Energy (3)
Rocky Flats Area Office
Attn: W.C. Rask
G. Huffman
T. Lukow
PO Box 928
Golden, CO 80402-0928

US Department of Energy
Dayton Area Office
Attn: R. Grandfield
PO Box 66
Miamisburg, OH 45343-0066

US Department of Energy
Attn: E. Young
Room E-178
GAO/RCED/GTN
Washington, DC 20545

US Bureau of Land Management
101 E. Mermod
Carlsbad, NM 88220

US Bureau of Land Management
New Mexico State Office
PO Box 1449
Santa Fe, NM 87507

US Environmental Protection
Agency (2)
Office of Radiation Protection
Programs (ANR-460)
Washington, DC 20460

US Nuclear Regulatory Commission
Division of Waste Management
Attn: H. Marson
Mail Stop 4-H-3
Washington, DC 20555

US Nuclear Regulatory Commission (4)
Advisory Committee on Nuclear Waste
Attn: D. Moeller
M.J. Steindler
P.W. Pomeroy
W.J. Hinze
7920 Norfolk Avenue
Bethesda, MD 20814

Defense Nuclear Facilities Safety
Board
Attn: D. Winters
625 Indiana Avenue, NW
Suite 700
Washington, DC 20004

Nuclear Waste Technical Review Board
(2)
Attn: Library
Suite 910
1100 Wilson Blvd.
Arlington, VA 22209-2297

Energy and Science Division
Office of Management and Budget
Attn: K. Yuracko
725 17th Street NW
Washington, DC 20503

US Geological Survey (2)
Water Resources Division
Attn: C. Peters
Suite 200
4501 Indian School, NE
Albuquerque, NM 87110

State Agencies

New Mexico Bureau of Mines
and Mineral Resources
Socorro, NM 87801

New Mexico Energy, Minerals and
Natural Resources Department
Attn: Librarian
2040 South Pacheco
Santa Fe, NM 87505

New Mexico Energy, Minerals and
Natural Resources Department
New Mexico Radioactive Task Force (2)
(Governor's WIPP Task Force)
Attn: A. Lockwood, Chairman
C. Wentz, Coordinator/Policy
Analyst
2040 South Pacheco
Santa Fe, NM 87505

Bob Forrest
Mayor, City of Carlsbad
PO Box 1569
Carlsbad, NM 88221

Executive Director
Carlsbad Department of Development
Attn: C. Bernard
PO Box 1090
Carlsbad, NM 88221

New Mexico Environment Department
Secretary of the Environment (3)
Attn: J. Espinosa
PO Box 968
1190 St. Francis Drive
Santa Fe, NM 87503-0968

New Mexico Environment Department
Attn: P. McCasland
WIPP Project Site Office
PO Box 3090
Carlsbad, NM 88221-3090

New Mexico State Engineer's Office
Attn: M. Chudnoff
PO Box 25102
Santa Fe, NM 87504-5102

Environmental Evaluation Group (5)
Attn: R. Neill
Suite F-2
7007 Wyoming Blvd., NE
Albuquerque, NM 87109

Advisory Committee on Nuclear Facility Safety

John F. Ahearne
Executive Director, Sigma Xi
99 Alexander Drive
Research Triangle Park, NC 27709

James E. Martin
109 Observatory Road
Ann Arbor, MI 48109

WIPP Panel of National Research Council's Board on Radioactive Waste Management

Charles Fairhurst, Chairman
Department of Civil and
Mineral Engineering
University of Minnesota
500 Pillsbury Dr., SE
Minneapolis, MN 55455-0220

John O. Blomeke
3833 Sandy Shore Drive
Lenoir City, TN 37771-9803

John D. Bredehoeft
Western Region Hydrologist
Water Resources Division
US Geological Survey (M/S 439)
345 Middlefield Road
Menlo Park, CA 94025

Fred M. Ernsberger
1325 NW 10th Avenue
Gainsville, FL 32601

Rodney C. Ewing
Department of Geology
University of New Mexico
200 Yale, NE
Albuquerque, NM 87131

B. John Garrick
PLG, Inc.
Suite 400
4590 MacArthur Blvd.
Newport Beach, CA 92660-2027

Leonard F. Konikow
US Geological Survey
431 National Center
Reston, VA 22092

Jeremiah O'Driscoll
505 Valley Hill Drive
Atlanta, GA 30350

Christopher Whipple
Clement International Corp.
160 Spear St.
Suite 1380
San Francisco, CA 94105-1535

National Research Council (3)
Board on Radioactive
Waste Management
RM HA456
Attn: P.B. Myers,
Staff Director (2)
G.J. Grube
2101 Constitution Avenue
Washington, DC 20418

Performance Assessment Peer Review Panel

G. Ross Heath
College of Ocean and
Fishery Sciences HN-15
583 Henderson Hall
University of Washington
Seattle, WA 98195

Thomas H. Pigford
Department of Nuclear Engineering
4159 Etcheverry Hall
University of California
Berkeley, CA 94720

Thomas A. Cotton
JK Research Associates, Inc.
4429 Butterworth Place, NW
Washington, DC 20016

Robert J. Budnitz
President, Future Resources
Associates, Inc.
2000 Center Street
Suite 418
Berkeley, CA 94704

C. John Mann
Department of Geology
245 Natural History Bldg.
1301 West Green Street
University of Illinois
Urbana, IL 61801

Frank W. Schwartz
Department of Geology and Mineralogy
The Ohio State University
Scott Hall
1090 Carmack Rd.
Columbus, OH 43210

National Laboratories

Argonne National Laboratory (2)
Attn: A. Smith
D. Tomasko
9700 South Cass, Bldg. 201
Argonne, IL 60439

Battelle Pacific Northwest Laboratory (3)
Attn: R.E. Westerman
S. Bates
H.C. Burkholder
Battelle Boulevard
Richland, WA 99352

Idaho National Engineering Laboratory (2)
Attn: H. Loo
J. Pruitt
Mail Stop 5219
Idaho Falls, ID 83403-4000

Chin-Fu Tsang
Lawrence Berkeley Laboratory
Earth Sciences Division
1 Cyclotron Rd.
Berkeley, CA 94720

Los Alamos National Laboratory
Attn: B. Erdal, CNC-11
PO Box 1663
Los Alamos, NM 87545

Los Alamos National Laboratory
Attn: A. Meijer
Mail Stop J514
PO Box 1663
Los Alamos, NM 87545

Los Alamos National Laboratory (3)
HSE-8
Attn: M. Enoris
L. Soholt
J. Wenzel
PO Box 1663
Los Alamos, NM 87545

Los Alamos National Laboratory
EM-7
Attn: S. Kosiewicz
Mail Stop J595
PO Box 1663
Los Alamos, NM 87545

Oak Ridge National Laboratory
Transuranic Waste Manager
Attn: D.W. Turner
PO Box 2008, Bldg. 3047
Oak Ridge, TN 37831-6060

Savannah River Laboratory (3)
Attn: N. Bibler
M.J. Plodinec
G.G. Wicks
Aiken, SC 29801

Savannah River Plant (2)
Attn: R.G. Baxter
Building 704-S
K.W. Wierzbicki
Building 703-H
Aiken, SC 29808-0001

Corporations/Members of the Public

Benchmark Environmental Corp. (2)
Attn: C. Frederickson
K. Lickliter
4501 Indian School, NE
Suite 105
Albuquerque, NM 87110

City of Albuquerque
Public Works Department
Utility Planning Division
Attn: W.K. Summers
PO Box 1293
Albuquerque, NM 87103

Deuel and Associates, Inc.
Attn: R.W. Prindle
7208 Jefferson, NE
Albuquerque, NM 87109

Disposal Safety, Inc.
Attn: B. Ross
Suite 314
1660 L Street, NW
Washington, DC 20036

Ecodynamics (3)
Attn: P. Roache
R. Blaine
K. Economy
PO Box 9229
Albuquerque, NM 87119-9229

EG & G Idaho (3)
1955 Fremont Street
Attn: C. Atwood
C. Hertzler
T.I. Clements
Idaho Falls, ID 83415

Geomatrix
Attn: K. Coppersmith
100 Pine Street #1000
San Francisco, CA 94111

Golder Associates, Inc. (3)
Attn: M. Cunnane
R. Kossik
I. Miller
4104 148th Avenue, NE
Redmond, WA 98052

INTERA, Inc. (6)
Attn: L. Snyder
C. Ardito
1650 University Blvd. NE
Suite 300
Albuquerque, NM 87102

INTERA, Inc.
Attn: A.M. LaVenue (25)
B.S. RamaRao (25)
6850 Austin Center Blvd.
Suite 300
Austin, TX 78731

INTERA, Inc. (9)
Attn: J.F. Pickens
G. Freeze
A. Haug
J. Beach
G. Grisak
S. Pahwa
R. Andrews
J. Duguid
S. Mishra
Suite #300
6850 Austin Center Blvd.
Austin, TX 78731

INTERA, Inc.
Attn: W. Stensrud
PO Box 2123
Carlsbad, NM 88221

INTERA, Inc.
Attn: W. Nelson
101 Convention Center Drive
Suite 540
Las Vegas, NV 89109

IT Corporation (2)
Attn: R.F. McKinney
J. Myers
Regional Office - Suite 700
5301 Central Avenue, NE
Albuquerque, NM 87108

MACTEC (2)
Attn: J.A. Thies
D.K. Duncan
8418 Zuni Road, SE
Suite 200
Albuquerque, NM 87108

Pacific Northwest Laboratory
Attn: B. Kennedy
Battelle Blvd.
PO Box 999
Richland, WA 99352

RE/SPEC, Inc. (2)
Attn: W. Coons
Suite 300
4775 Indian School, NE
Albuquerque, NM 87110

RE/SPEC, Inc.
Attn: J.L. Ratigan
PO Box 725
Rapid City, SD 57709

Reynolds Elect/Engr. Co., Inc.
Building 790, Warehouse Row
Attn: E.W. Kendall
PO Box 98521
Las Vegas, NV 89193-8521

Roy F. Weston, Inc.
CRWM Tech. Supp. Team
Attn: C.J. Noronha
955 L'Enfant Plaza, SW
North Building, Eighth Floor
Washington, DC 20024

Science Applications International
Corporation (SAIC)
Attn: H.R. Pratt
10260 Campus Point Drive
San Diego, CA 92121

Science Applications International
Corporation (2)
Attn: D.C.Royer
C.G. Pflum
101 Convention Center Dr.
Las Vegas, NV 89109

Science Applications International
Corporation (2)
Attn: M. Davis
J. Tollison
2109 Air Park Road, SE
Albuquerque, NM 87106

Science Applications International
Corporation (2)
Attn: J. Young
D. Lester
18706 North Creek Parkway
Suite 110
Bothell, WA 98011

Southwest Research Institute
Center for Nuclear Waste Regulatory
Analysis (2)
Attn: P.K. Nair
6220 Culebra Road
San Antonio, TX 78228-0510

Systems, Science, and Software (2)
Attn: E. Peterson
P. Lagus
Box 1620
La Jolla, CA 92038

TASC
Attn: S.G. Oston
55 Walkers Brook Drive
Reading, MA 01867

Tech Reps, Inc. (6)
Attn: J. Chapman
C. Crawford
D. Marchand
J. Stikar
P. Oliver
D. Scott
5000 Marble NE
Suite 222
Albuquerque, NM 87110

Tolan, Beeson, & Associates
Attn: T.L. Tolan
2320 W. 15th Avenue
Kennewick, WA 99337

TRW Environmental Safety Systems
Attn: I. Sacks
2650 Park Tower Drive
Suite 800
Vienna, VA 22180

Westinghouse Electric Corporation (5)
Attn: Library
L. Trego
C. Cox
L. Fitch
R.F. Kehrman
PO Box 2078
Carlsbad, NM 88221

Westinghouse Hanford Company
MSIN HO-32
Attn: D. Wood
PO Box 1970
Richland, WA 99352

Western Water Consultants
Attn: D. Fritz
1949 Sugarland Drive #134
Sheridan, WY 82801-5720

Western Water Consultants
Attn: P.A. Rechard
PO Box 4128
Laramie, WY 82071

P. Drez
8816 Cherry Hills Road, NE
Albuquerque, NM 87111

D.W. Powers
Star Route Box 87
Anthony, TX 79821

Shirley Thieda
PO Box 2109, RR1
Bernalillo, NM 87004

Jack Urich
c/o CARD
144 Harvard, SE
Albuquerque, NM 87106

Universities

Texas A&M University
Department of Geology
Attn: P.A. Domenico
College Station, TX 77840

Texas A&M University (4)
Department of Geophysics
Attn: R. Carlson
T. Spencer
B. Johnson
E. Hoskins
College Station, TX 77840

University of California
Mechanical, Aerospace, and
Nuclear Engineering Department (2)
Attn: W. Kastenberg
D. Browne
5532 Boelter Hall
Los Angeles, CA 90024

University of California
Mine Engineering Dept.
Attn: Neville Cook
Rock Mechanics Engineering
Berkeley, CA 94720

University of Hawaii at Hilo
Attn: S. Hora
Business Administration
Hilo, HI 96720-4091

University of New Mexico
Geology Department
Attn: Library
Albuquerque, NM 87131

University of New Mexico
Research Administration
Attn: H. Schreyer
102 Scholes Hall
Albuquerque, NM 87131

University of Wyoming
Department of Civil Engineering
Attn: V.R. Hasfurther
Laramie, WY 82071

University of Wyoming
Department of Geology
Attn: J.I. Drever
Laramie, WY 82071

University of Wyoming
Department of Mathematics
Attn: R.E. Ewing
Laramie, WY 82071

Libraries

Thomas Brannigan Library
Attn: D. Dresp
106 W. Hadley St.
Las Cruces, NM 88001

Hobbs Public Library
Attn: M. Lewis
509 N. Ship Street
Hobbs, NM 88248

New Mexico State Library
Attn: N. McCallan
325 Don Gaspar
Santa Fe, NM 87503

New Mexico Tech
Martin Speere Memorial Library
Campus Street
Socorro, NM 87810

New Mexico Junior College
Pannell Library
Attn: R. Hill
Lovington Highway
Hobbs, NM 88240

Carlsbad Municipal Library
WIPP Public Reading Room
Attn: L. Hubbard
101 S. Halagueno St.
Carlsbad, NM 88220

University of New Mexico
General Library
Government Publications Department
Albuquerque, NM 87131

NEA/Performance Assessment Advisory Group (PAAG)

P. Duerden
ANSTO
Lucas Heights Research Laboratories
Private Mail Bag No. 1
Menai, NSW 2234, AUSTRALIA

Gordon S. Linsley
Division of Nuclear Fuel Cycle and Waste Management
International Atomic Energy Agency
PO Box 100
A-1400 Vienna, AUSTRIA

Nicolo Cadelli
Commission of the European Communities
200, Rue de la Loi
B-1049 Brussels, BELGIUM

R. Heremans
Organisme Nationale des Déchets Radioactifs et des Matiéres Fissiles
ONDRAF
Place Madou 1, Boitec 24/25
B-1030 Brussels, BELGIUM

J. Marivoet
Centre d'Etudes de l'Energie Nucléaire
CEN/SCK
Boeretang 200
B-2400 Mol, BELGIUM

P. Conlon
Waste Management Division
Atomic Energy Control Board (AECB)
PO Box 1046
Ottawa, Canada KIP 559, CANADA

A.G. Wikjord
Manager, Environmental and Safety Assessment Branch
Atomic Energy of Canada Limited
Whiteshell Nuclear Research Establishment
Pinewa, Manitoba ROE 1LO, CANADA

Jukka-Pekka Salo
Teollisuuden Voima Oy (TVO)
Fredrikinkatu 51-53 B
SF-00100 Helsinki, FINLAND

Timo Vieno
Technical Research Centre of Finland (VTT)
Nuclear Energy Laboratory
PO Box 208
SF-02151 Espoo, FINLAND

Timo Äikäs
Teollisuuden Voima Oy (TVO)
Fredrikinkatu 51-53 B
SF-00100 Helsinki, FINLAND

M. Claude Ringeard
Division de la Sécurité et de la Protection de l'Environment (DSPE)
Commissariat á l'Energie Atomique
Agence Nationale pour la Gestion des Déchets Radioactifs (ANDRA)
Route du Panorama Robert Schuman
B. P. No. 38
F-92266 Fontenay-aux-Roses Cedex
FRANCE

Gérald Ouzounian
Agence Nationale pour la Gestion des Déchets Radioactifs (ANDRA)
Route du Panorama Robert Schuman
B. P. No. 38
F-92266 Fontenay-aux-Roses Cedex
FRANCE

Claudio Pescatore
Division of Radiation Protection and Waste Management
OECD Nuclear Energy Agency
38, Boulevard Suchet
F-75016 Paris, FRANCE

M. Dominique Greneche
Commissariat á l'Energie Atomique
IPSN/DAS/SASICC/SAED
B. P. No. 6
F-92265 Fontenay-aux-Roses Cedex,
FRANCE

Robert Fabriol
Bureau de Recherches Géologiques et Miniéres (BRGM)
B. P. 6009
45060 Orléans Cedex 2, FRANCE

P. Bogorinski
Gesellschaft für Reaktorsicherheit (GRS) mbH
Schwertnergasse 1
D-5000 Köln 1, GERMANY

R. Storck
GSF - Institut für Tieflagerung
Theodor-Heuss-Strabe 4
D-3300 Braunschweig, GERMANY

Ferrucio Gera
ISMES S.p.A
Via del Crociferi 44
I-00187 Rome, ITALY

Hiroyuki Umeki
Isolation System Research Program
Radioactive Waste Management Project
Power Reactor and Nuclear Fuel Development Corporation (PNC)
1-9-13, Akasaka
Minato-ku
Tokyo 107, JAPAN

P. Carboneras Martinez
ENRESA
Calle Emilio Vargas 7
R-28043 Madrid, SPAIN

Tönis Papp
Swedish Nuclear Fuel and Waste Management Co.
Box 5864
S 102 48 Stockholm, SWEDEN

Conny Hägg
Swedish Radiation Protection Institute (SSI)
Box 60204
S-104 01 Stockholm, SWEDEN

J. Hadermann
Paul Scherrer Institute
Waste Management Programme
CH-5232 Villigen PSI, SWITZERLAND

J. Vigfusson
USK- Swiss Nuclear Safety Inspectorate
Federal Office of Energy
CH-5303 Würenlingen, SWITZERLAND

D.E. Billington
Departmental Manager - Assessment Studies
Radwaste Disposal R&D Division
AEA Decommissioning & Radwaste
Harwell Laboratory, B60
Didcot Oxfordshire OX11 ORA
UNITED KINGDOM

P. Grimwood
Waste Management Unit
BNFL
Sellafield
Seascale, Cumbria CA20 1PG
UNITED KINGDOM

Alan J. Hooper
UK Nirex Ltd
Curie Avenue
Harwell, Didcot
Oxfordshire, OX11 ORH
UNITED KINGDOM

Jerry M. Boak
Yucca Mountain Project Office
US Department of Energy
PO Box 98608
Las Vegas, NV 89193

Seth M. Coplan (Chairman)
US Nuclear Regulatory Commission
Division of High-Level Waste Management
Mail Stop 4-H-3
Washington, DC 20555

A.E. Van Luik
INTERA/M&O
The Valley Bank Center
101 Convention Center Dr.
Las Vegas, NV 89109

NEA/PSAG User's Group

Shaheed Hossain
Division of Nuclear Fuel Cycle and Waste Management
International Atomic Energy Agency
Wagramerstrasse 5
PO Box 100
A-1400 Vienna, AUSTRIA

Alexander Nies (PSAC Chairman)
Gesellschaft für Strahlen- und
Institut für Tieflagerung
Abteilung für Endlagersicherheit
Theodor-Heuss-Strasse 4
D-3300 Braunschweig, GERMANY

Eduard Hofer
Gesellschaft für Reaktorsicherheit
(GRS) MBH
Forschungsgelände
D-8046 Garching, GERMANY

Andrea Saltelli
Commission of the European Communities
Joint Resarch Centre of Ispra
I-21020 Ispra (Varese), ITALY

Alejandro Alonso
Cátedra de Tecnología Nuclear
E.T.S. de Ingenieros Industriales
José Gutiérrez Abascal, 2
E-28006 Madrid, SPAIN

Pedro Prado
CIEMAT
Instituto de Tecnología Nuclear
Avenida Complutense, 22
E-28040 Madrid, SPAIN

Miguel Angel Cuñado
ENRESA
Emilio Vargas, 7
E-28043 Madrid, SPAIN

Francisco Javier Elorza
ENRESA
Emilio Vargas, 7
E-28043 Madrid, SPAIN

Nils A. Kjellbert
Swedish Nuclear Fuel and Waste
Management Company (SKB)
Box 5864
S-102 48 Stockholm, SWEDEN

Björn Cronhjort
Swedish National Board for Spent
Nuclear Fuel (SKN)
Sehlsedtsgatan 9
S-115 28 Stockholm, SWEDEN

Richard A. Klos
Paul-Scherrer Institute (PSI)
CH-5232 Villingen PSI
SWITZERLAND

NAGRA (3)
Attn: C. McCombie
F. Van Dorp
S. Vomvoris
Parkstrasse 23
CH-5401 Baden, SWITZERLAND

N. A. Chapman
Intera Information Technologies
Park View House, 14B Burton Street
Melton Mowbray
Leicestershire, LE13 1AE
UNITED KINGDOM

Daniel A. Galson
Galson Sciences Ltd.
35, Market Place
Oakham
Leicestershire LE15 6DT
UNITED KINGDOM

David P. Hodgkinson
Intera Information Technologies
Chiltern House
45 Station Road
Henley-on-Thames
Oxfordshire RG9 1AT, UNITED KINGDOM

Brian G.J. Thompson
Department of the Environment: Her
Majesty's Inspectorate of Pollution
Room A5.33, Romney House
43 Marsham Street
London SW1P 2PY, UNITED KINGDOM

Intera Information Technologies
Attn: M.J.Apted
3609 South Wadsworth Blvd.
Denver, CO 80235

US Nuclear Regulatory Commission (2)
Attn: R. Codell
N. Eisenberg
Mail Stop 4-H-3
Washington, DC 20555

Battelle Pacific Northwest
Laboratories
Attn: P.W. Eslinger
PO Box 999, MS K2-32
Richland, WA 99352

Center for Nuclear Waste Regulatory Analysis (CNWRA)
Southwest Research Institute
Attn: B. Sagar
PO Drawer 28510
6220 Culebra Road
San Antonio, TX 78284

Geostatistics Expert Working Group (GXG)

Rafael L. Bras
R.L. Bras Consulting Engineers
44 Percy Road
Lexington, MA 02173

Jesus Carrera
Universidad Politécnica de Cataluña
E.T.S.I. Caminos
Jordi, Girona 31
E-08034 Barcelona, SPAIN

Gedeon Dagan
Department of Fluid Mechanics and Heat Transfer
Tel Aviv University
PO Box 39040
Ramat Aviv, Tel Aviv 69978, ISRAEL

Ghislain de Marsily (GXG Chairman)
University Pierre et Marie Curie
Laboratorie de Geologie Applique
4, Place Jussieu - T.26 - 5e etage
75252 Paris Cedex 05, FRANCE

Alain Galli
Centre de Geostatistique
Ecole des Mines de Paris
35 Rue St. Honore
77035 Fontainebleau, FRANCE

Steve Gorelick
Department of Applied Earth Sciences
Stanford University
Stanford, CA 94305-2225

Peter Grindrod
INTERA Information Technologies Ltd.
Chiltern House, 45 Station Road
Henley-on-Thames
Oxfordshire, RG9 1AT
UNITED KINGDOM

Alan Gutjahr
Department of Mathematics
New Mexico Institute of Mining and Technology
Socorro, NM 87801

C. Peter Jackson
Harwell Laboratory
Theoretical Studies Department
Radwaste Disposal Division
Bldg. 424.4
Oxfordshire Didcot Oxon OX11 ORA
UNITED KINDGOM

Peter Kitanidis
60 Peter Coutts Circle
Stanford, CA 94305

Rae Mackay
Department of Civil Engineering
University of Newcastle Upon Tyne
Newcastle Upon Tyne NE1 7RU
UNITED KINGDOM

Dennis McLaughlin
Parsons Laboratory
Room 48-209
Department of Civil Engineering
Massachusetts Institute of Technology
Cambridge, MA 02139

Shlomo P. Neuman
College of Engineering and Mines
Department of Hydrology and Water Resources
University of Arizona
Tucson, AZ 85721

Christian Ravenne
Geology and Geochemistry Division
Institut Francais du Pétrole
1 & 4, av. de Bois-Préau BP311
92506 Rueil Malmaison Cedex, FRANCE

Yoram Rubin
Department of Civil Engineering
University of California
Berkeley, CA 94720

Foreign Addresses

Studiecentrum Voor Kernenergie
Centre D'Energie Nucleaire
Attn: A. Bonne
SCK/CEN
Boeretang 200
B-2400 Mol, BELGIUM

Atomic Energy of Canada, Ltd. (3)
Whiteshell Research Estab.
Attn: M.E. Stevens
B.W. Goodwin
D. Wushke
Pinewa, Manitoba
ROE 1L0, CANADA

Esko Peltonen
Industrial Power Company Ltd.
TVO
Fredrikinkatu 51-53
SF-00100 Helsinki 10, FINLAND

Jean-Pierre Olivier
OECD Nuclear Energy Agency (2)
38, Boulevard Suchet
F-75016 Paris, FRANCE

D. Alexandre, Deputy Director
ANDRA
31 Rue de la Federation
75015 Paris, FRANCE

Claude Sombret
Centre D'Etudes Nucleaires
De La Vallee Rhone
CEN/VALRHO
S.D.H.A. BP 171
30205 Bagnols-Sur-Ceze, FRANCE

Bundesministerium fur Forschung und
Technologie
Postfach 200 706
5300 Bonn 2, GERMANY

Bundesanstalt fur Geowissenschaften
und Rohstoffe
Attn: M. Langer
Postfach 510 153
3000 Hanover 51, GERMANY

Gesellschaft fur Reaktorsicherheit
(GRS) (2)
Attn: B. Baltes
W. Muller
Schwertnergasse 1
D-5000 Cologne, GERMANY

Hahn-Mietner-Institut fur
Kernforschung
Attn: W. Lutze
Glienicker Strasse 100
100 Berlin 39, GERMANY

Institut fur Tieflagerung (2)
Attn: K. Kuhn
Theodor-Heuss-Strasse 4
D-3300 Braunschweig, GERMANY

Physikalisch-Technische Bundesanstalt
Attn: P. Brenneke
Postfach 33 45
D-3300 Braunschweig, GERMANY

Shingo Tashiro
Japan Atomic Energy Research
Institute
Tokai-Mura, Ibaraki-Ken
319-11, JAPAN

Netherlands Energy Research
Foundation (ECN)
Attn: L.H. Vons
3 Westerduinweg
PO Box 1
1755 ZG Petten, THE NETHERLANDS

Anders Windberg
Conterra AB
Krokslätts Fabriker 30
S-431 37 Mölndal, SWEDEN

Johan Andersson
Swedish Nuclear Power Inspectorate
Statens Kärnkraftinspektion (SKI)
Box 27106
S-102 52 Stockholm, SWEDEN

Fred Karlsson
Svensk Karnbransleforsorjning AB
SKB
Box 5864
S-102 48 Stockholm, SWEDEN

D.R. Knowles
British Nuclear Fuels, plc
Risley, Warrington, Cheshire WA3 6AS
1002607, UNITED KINGDOM

Nationale Genossenschaft fur die
Lagerung Radioaktiver Abfalle
(NAGRA) (2)
Attn: S. Vomvoris
P. Zuidema
Hardstrasse 73
CH-5430 Wettingen, SWITZERLAND

AEA Technology
Attn: J.H. Rees
D5W/29 Culham Laboratory
Abington
Oxfordshire OX14 3DB, UNITED KINGDOM

AEA Technology
Attn: W.R. Rodwell
O44/A31 Winfrith Technical Centre
Dorchester
Dorset DT2 8DH, UNITED KINGDOM

AEA Technology
Attn: J.E. Tinson
B4244 Harwell Laboratory
Didcot, Oxfordshire OX11 ORA
UNITED KINGDOM

Internal

1	A. Narath
20	O.E. Jones
1502	J.C. Cummings
1511	D.K. Gartling
6000	D.L. Hartley
6115	P.B. Davies
6119	E.D. Gorham
6119	Staff (14)
6121	J.R. Tillerson
6121	Staff (7)
6233	J.C. Eichelberger
6300	D.E. Miller
6302	L.E. Shephard
6303	W.D. Weart
6303	S.Y. Pickering
6304	J.T. Holmes
6305	S.A. Goldstein
6312	F.W. Bingham
6313	L.S. Costin
6331	P.A. Davis
6331	S.H. Conrad
6341	A.L. Stevens
6341	Staff (6)
6341	Sandia WIPP Central Files (100)
6342	D.R. Anderson
6342	Staff (30)
6343	T.M. Schultheis
6343	Staff (3)
6345	R.C. Lincoln
6345	Staff (9)
6347	D.R. Schafer
6400	D.J. McCloskey
6400	N.R. Ortiz
6613	R.M. Cranwell
6613	R.L. Iman
6613	C. Leigh
6613	J.E. Campbell
6622	M.S.Y. Chu
6622	J.T. McCord
6641	R.E. Luna, Acting
7723	R.G. Knowlton
7141	Technical Library (5)
7151	Technical Publications
7613-2	Document Processing for DOE/OSTI (10)
8523-2	Central Technical Files
9300	J.E. Powell
9310	J.D. Plimpton
9330	J.D. Kennedy

U.S. GOVERNMENT PRINTING OFFICE: 1993—837-923 02